Title
Study on Disordered and Dissipative Quantum Spin Systems

Permalink
https://escholarship.org/uc/item/7g9020pm

Author
Wang, Jian

Publication Date
2019

Peer reviewed|Thesis/dissertation

UNIVERSITY OF CALIFORNIA

Los Angeles

Study on Disordered and Dissipative Quantum Spin Systems

A dissertation submitted in partial satisfaction

of the requirements for the degree

Doctor of Philosophy in Physics

by

Jian Wang

2019

ABSTRACT OF THE DISSERTATION

Study on Disordered and Dissipative Quantum Spin Systems

by

Jian Wang

Doctor of Philosophy in Physics

University of California, Los Angeles, 2019

Professor Sudip Chakravarty, Chair

Disorders and dissipations play the key role in the understanding of quantum coherent system. In this thesis, I'm using numeric method plus theoretical analysis to answer the questions: What are the low energy modes in disordered quantum spin system? How will environment dissipation damp the spin system's quasi-particle excitation quantitatively? There are three parts in my thesis. Part 1 is the study of disordered quantum Ising chain. Part 2 is a numerical method for analytic continuation. Part 3 is the study of dissipative quantum Ising chain.

Part 1: Dynamical structure factor $S(k, \omega)$ is calculated for the one-dimensional (1D) transverse field Ising model and its recent extension to include a three spin term with quenched binary disorder. We study the low energy modes for lattices as large as 256 sites. We show that the intense zero energy modes appear whenever the binary disorder straddles two different topological winding numbers. We argue that these are Majorana modes, which reside on the boundaries of the rare regions. The size distribution of Majorana pairs has a fractal behavior at the critical points. With the longer ranged interactions a spin glass transition is observed as well.

Part 2: A simple method for numerical analytic continuation is developed. It is designed to analytically continue the imaginary time (Matsubara frequency) quantum Monte Carlo

simulation results to the real time (real frequency) domain. Such a method is based on the Padé approximation. We modify it to be a linear regression problem, and then use bootstrapping statistics to get the averaged result and estimate the error. Unlike maximum entropy method, no prior information is needed. Test-cases have shown that the spectrum is recovered for inputs with relative error as high as 1%.

Part 3: In this section, I generalize the (0+1)-dimensional spin-boson problem to the corresponding (1+1)-dimensional version. Monte Carlo simulation is used to find the phase diagram and imaginary time correlation function. The real frequency spectrum is recovered by my newly developed Padé regression analytic continuation method in part 2. We find that, as dissipation strength α is increased, the sharp quasi-particle spectrum is broadened and the peak frequency is lower. The quasi-particle excitation picture will eventually break down when α is large enough. According to the behavior of the low frequency spectrum, we classify the dynamical phase into three different regions: weakly damped, linear k-edge, and strongly damped.

The dissertation of Jian Wang is approved.

Stuart Brown

Yaroslav Tserkovnyak

Marek Biskup

Sudip Chakravarty, Committee Chair

University of California, Los Angeles

2019

To my family and friends

CONTENTS

LIST OF FIGURES

xiii

ACKNOWLEDGMENTS

Firstly, I would like to express my sincere gratitude to my advisor Prof. Sudip Chakravarty for the continuous support of my Ph.D study and related research, for his patience, motivation, and immense knowledge. His guidance helped me in all the time of research and writing of this thesis.

Besides my advisor, I would like to thank the rest of my thesis committee: Prof. Stuart Brown, Prof. Yaroslav Tserkovnyak, and Prof. Marek Biskup, for their insightful comments and encouragement, but also for the hard question which incented me to widen my research from various perspectives.

My sincere thanks also goes to Dr. Arash Bellaford, Dr. Antonio Russo, and Dr. Zhiqiang Wang, who provided me an opportunity to join the group. Without they precious support it would not be possible to conduct this research. I thank my fellow group mates Nicholas Rombes, Ian Powell, Steve Durr in for the stimulating discussions. I am also lucky to have some great friends in UCLA who have enriched my graduate life a lot. Among them are especially Xueping Long, Jiatong Chen. They have given me numerous suggestions and advices on different aspects of life.

Last but not the least, I would like to thank my parents.

<div align="center">CURRICULUM VITAE</div>

2009 – 2013	B.S. in Physics, University of Science and Technology of China (USTC), Hefei, People's Republic of China.
2013 – Present	Ph.D. student in Physics, University of California, Los Angeles (UCLA).

<div align="center">PUBLICATIONS</div>

Jian Wang, Sudip Chakravarty, "Spectra of the Dissipative Spin Chain" (2019),
arXiv:1903.00567 [cond-mat.str-el].

Jian Wang, Sudip Chakravarty, "Rational function regression method for numerical analytic continuation" (2018),
arXiv:1812.01817 [physics.comp-ph].

Jian Wang, Sudip Chakravarty, "Binary disorder in quantum Ising chains and induced Majorana zero modes" (2018),
arXiv:1808.04481 [cond-mat.dis-nn].

CHAPTER 1

Disordered quantum Ising chain

1.1 Introduction

Transverse field Ising model (TFIM) is a prototype to study quantum phase transitions [40, 13] , it describes a variety of quantum magnets ranging from LiHoF$_4$ [39] to CoNb$_2$O$_6$ [10]. It is also a theoretical model to understand adiabatic quantum annealing [11, 9, 38], where the gap closing is important in this problem. With the paper by Kitaev [24] , TFIM can also be a play ground of topological quantum computation, where Majorana zero modes are supported at the boundaries.

In the pure system, the TFIM is well understood. However, disorder is inevitable in reality. It can come from numerous sources. Instead of universal power law near pure system quantum critical point, thermodynamic properties will be highly singular in disordered systems, including log-normal distribution of gaps [5], activated scaling, exponentially slow dynamics, and so on. These can be understood as rare region effects. There has been work on disorder effects on Majorana modes [28, 16, 27] , and the low energy distribution, but little is known about the spatial distribution of the Majorana modes, and their relation with Griffiths-like rare regions. In this paper, we will clarify the relation of rare regions, exponentially slow dynamical excitations, and the exponential degeneracy of Majorana zero modes.

The outline of this chapter is as follows: in section 1.2, the problem is stated quite generally, including three spin interactions studied recently, and the method of calculating spin-spin correlation function, and the dynamical structure factor are given. In section 1.3, the condition for emergent low energy model in disordered system is given for 2-spin model

with binary transverse field disorder. And the nature of phase transition is explained.

In section 1.4, we will argue that these low energy modes are Majorana zero modes (MZM) at the boundaries of Griffiths like rare region by comparing the spin-spin correlation function and the lowest energy Majorana eigenvectors. The size distribution of MZM is also calculated, at the critical point the most probable size is $1/5$ of the system length; we also notice a self similar distribution.

In the Section 1.5, disordered longer range interaction is explored. The rare region induced Majorana zero modes picture is similar to the 2-spin case. As a result of frustration from the longer range interaction, we also notice a spin-glass phase transitions in this case.

1.2 The Hamiltonian

Transverse field Ising chain with longer range interaction with disorder:

$$H = -\sum_{i=1}^{L} h_i \sigma_i^z - \sum_{i=1}^{L-1} \lambda_{1i} \sigma_i^x \sigma_{i+1}^x - \sum_{i=1}^{L-2} \lambda_{2i} \sigma_i^x \sigma_{i+1}^z \sigma_{i+2}^x \tag{1.1}$$

where i is the site. L is the size of 1-D system with open boundary condition. Here h_i is quenched transverse field, λ_{1i} is two-spin couplings and λ_{2i} is three-spin couplings, they can be of constant value, or random variables satisfying certain distributions.

The spin-spin correlation function, is calculated using the ground state average $\langle \cdots \rangle$ and the disorder ensemble average $\overline{\cdots}$

$$C(r,t) := \overline{\langle \sigma_i^x(t) \sigma_j^x(0) \rangle} \tag{1.2}$$

Since our disorder averaged system is translational invariant, we use r as the distance between two sites. The dynamical structure factor $S(k,\omega)$ is the time and spatial Fourier transformation of the spin-spin correlation function:

$$S(k,\omega) = \int dt \int dr \ e^{i\omega t} e^{-ikr} C(r,t) \tag{1.3}$$

1.2.1 Jordan Wigner and the spin-spin correlation function

From Jordan-Wigner transformation the system can be expressed in terms of single particle fermion operators to solve the eigenvalues and eigenvectors for a given lattice with a given disorder configuration

$$
H = \sum_{i=1}^{L} h_i(c_i^\dagger - c_i)(c_i^\dagger + c_i) - \sum_{i=1}^{L-1} \lambda_{1i}(c_i^\dagger - c_i)(c_{i+1}^\dagger + c_{i+1})
$$
$$
- \sum_{i=1}^{L-2} \lambda_{2i}(c_i^\dagger - c_i)(c_{i+2}^\dagger + c_{i+2}) \tag{1.4}
$$

The spin-spin correlation function in terms of fermion operators is given by

$$
\langle \sigma_i^x(t)\sigma_j^x(0)\rangle = \langle (c_1^\dagger(t) + c_1(t)) \cdots (c_j^\dagger(0) + c_j(0)\rangle. \tag{1.5}
$$

Using Wick's theorem, the right hand side can be expressed as a Pfaffian of a $2i + 2j - 2$ dimensional matrix. Each element in the matrix is a free two-fermion correlator.

Suppose we have the eigenvalues $\{\epsilon_i\}$ and eigenvectors $\{v_i\}$ of the quadratic fermion Hamilton kernel $H = \begin{pmatrix} A & B \\ -B & -A \end{pmatrix}$. Our the questions is, how to recover $< \sigma_i^x(t)\sigma_j^x(0) >$ from the result of $\{\epsilon_i\}$ $\{v_i\}$, $(i = 1, 2, \cdots, 2L)$

Replace spin by fermion operators,

$$
\sigma_i^x(t) = \left(\prod_{m=1}^{i-1} \left(c_m^\dagger(t) + c_m(t) \right)\left(c_m^\dagger(t) - c_m(t) \right) \right)\left(c_i^\dagger(t) + c_i(t) \right) \tag{1.6}
$$

The correlation function can be written as:

$$
< \sigma_i^x(t)\sigma_j^x(0) >=< \left(\prod_{m=1}^{i-1} \left(c_m^\dagger(t) + c_m(t) \right)\left(c_m^\dagger(t) - c_m(t) \right) \right)\left(c_i^\dagger(t) + c_i(t) \right)
$$
$$
\left(\prod_{n=1}^{j-1} \left(c_n^\dagger(0) + c_n(0) \right)\left(c_n^\dagger(0) - c_n(0) \right) \right)\left(c_j^\dagger(0) + c_j(0) \right) > \tag{1.7}
$$

L.H.S. of Equation (1.7) is a $2(i + j - 1)$ fermions operator correlation function. Applying Wick's theorem, such a structure can be decomposed as a Pfaffian sum of two fermions correlation.

3

Therefore, the problem can now be asked as how to calculate:

$$< \left(c_m^\dagger(t) \pm c_m(t) \right) \left(c_n^\dagger(t') \pm c_n(t') \right) > \tag{1.8}$$

the strategy is to expand site fermion operators $c^\dagger$ c in terms of free fermion operators $\gamma^\dagger$ γ, these expansion coefficient will involve $\{v_i\}$, and the free fermion correlations $< \gamma_i^\dagger(t)\gamma_j(t') >$ will involve $\{\epsilon_i\}$

The goal of this subsection is to calculate **two fermion correlation** Eq. (1.8) using the free fermion $\gamma^\dagger$ γ.

$$\hat{H} = \begin{pmatrix} c^\dagger & c \end{pmatrix} H \begin{pmatrix} c \\ c^\dagger \end{pmatrix} = \begin{pmatrix} c^\dagger & c \end{pmatrix} VDV^{-1} \begin{pmatrix} c \\ c^\dagger \end{pmatrix} = \begin{pmatrix} \gamma^\dagger & \gamma \end{pmatrix} D \begin{pmatrix} \gamma \\ \gamma^\dagger \end{pmatrix} \tag{1.9}$$

H is the kernel matrix, D and V are $2L \times 2L$ number valued matrices of $\{\epsilon_i\}$ $\{v_i\}$, $(i = 1, 2, \cdots, 2L)$, assuming the ϵ_i are in descending order.

$$D_{2L \times 2L} = \begin{pmatrix} \epsilon_1 & & & & & \\ & \ddots & & & & \\ & & \epsilon_L & & & \\ & & & \epsilon_{L+1} & & \\ & & & & \ddots & \end{pmatrix} = \begin{pmatrix} \epsilon_1 & & & & & \\ & \ddots & & & & \\ & & \epsilon_L & & & \\ & & & \bar{\epsilon}_L & & \\ & & & & \ddots & \end{pmatrix} \tag{1.10}$$

$$V_{2L \times 2L} = \begin{pmatrix} | & | & & | & | & & | \\ v_1 & v_2 & \dots & v_L & v_{L+1} & \dots & v_{2L} \\ | & | & & | & | & & | \end{pmatrix} \tag{1.11}$$

$\begin{pmatrix} c^\dagger & c \end{pmatrix} = (c_1^\dagger, c_2^\dagger, ..., c_L^\dagger, c_1, c_2, ..., c_L)$ is operator valued row vector

$\begin{pmatrix} c \\ c^\dagger \end{pmatrix} = (c_1, c_2, ..., c_L, c_1^\dagger, c_2^\dagger, ..., c_L^\dagger)^T = (c^\dagger\ c)^\dagger$ is operator valued column vector.

The Hamiltonian represented with gamma is decoupled.

$$\hat{H} = \sum_{i=1}^{L} \left(\epsilon_i \gamma_i^\dagger \gamma_i + \bar{\epsilon}_i \gamma_i \gamma_i^\dagger \right) = \sum_{i=1}^{L} (\epsilon_i - \bar{\epsilon}_i)\gamma_i^\dagger \gamma_i + \sum_{i=1}^{L} \bar{\epsilon}_i \tag{1.12}$$

4

Theoretically $(\epsilon_i - \bar{\epsilon}_i) = \epsilon_i - \epsilon_{2L+1-i}$ is equivalent $2\epsilon_i$, when $\{\epsilon_i\}$ is arranged in descending order, because the p-h symmetry $\epsilon_i + \bar{\epsilon}_i = \epsilon_i + \epsilon_{2L+1-i} = 0$, however, in numerical calculations, the relative error $\frac{|\epsilon_i + \bar{\epsilon}_i|}{|\epsilon_i|}$ becomes very large, when $|\epsilon_i|$ is also close the zero. This subtlety warns us that, we shouldn't use half of eigenvalue and eigenvectors. The aim Equation (1.12), is to give us the ground state average

$$< \gamma_i(t)\gamma_j^\dagger(0) > = \delta_{ij} e^{+i(\epsilon_i - \bar{\epsilon}_i)t}$$

Now, going back to the goal of solving Equation (1.8), we need to expand $c_i^\dagger \pm c_i$ in terms of gamma:

$$\begin{pmatrix} c^\dagger + c \\ c^\dagger - c \end{pmatrix} = \begin{pmatrix} 1 & 1 \\ -1 & 1 \end{pmatrix} \begin{pmatrix} c \\ c^\dagger \end{pmatrix} = \begin{pmatrix} 1 & 1 \\ -1 & 1 \end{pmatrix} V \begin{pmatrix} \gamma \\ \gamma^\dagger \end{pmatrix} \tag{1.13}$$

The Hermitian conjugate:

$$\begin{pmatrix} c^\dagger + c & -c^\dagger + c \end{pmatrix} = \begin{pmatrix} \gamma^\dagger & \gamma \end{pmatrix} V^\dagger \begin{pmatrix} 1 & -1 \\ 1 & 1 \end{pmatrix} \tag{1.14}$$

The column vector times the row vector, and then take the ground state average, it will gives result of Equation (1.8):

$$\left\langle \begin{pmatrix} c^\dagger + c \\ c^\dagger - c \end{pmatrix}_t \begin{pmatrix} c^\dagger + c & -c^\dagger + c \end{pmatrix}_0 \right\rangle = \begin{pmatrix} 1 & 1 \\ -1 & 1 \end{pmatrix} V \left\langle \begin{pmatrix} \gamma^\dagger \\ \gamma \end{pmatrix} \begin{pmatrix} \gamma^\dagger & \gamma \end{pmatrix}_0 \right\rangle_t V^\dagger \begin{pmatrix} 1 & -1 \\ 1 & 1 \end{pmatrix} \tag{1.15}$$

$$\left\langle \begin{pmatrix} \gamma \\ \gamma^\dagger \end{pmatrix}_t \begin{pmatrix} \gamma^\dagger & \gamma \end{pmatrix}_0 \right\rangle = \begin{pmatrix} \delta_{ij} e^{+i(\epsilon_i - \bar{\epsilon}_i)t} & 0 \\ 0 & 0 \end{pmatrix} \tag{1.16}$$

Equation (1.15), is a $2L \times 2L$ matrix, the compact form is given by:

$$M_t = SV \begin{pmatrix} P_t & 0 \\ 0 & 0 \end{pmatrix} V^\dagger S^\dagger \begin{pmatrix} 1 & 0 \\ 0 & -1 \end{pmatrix}$$

The p-h symmetric of the system require that, when we diagonalize the Hamiltonian kernel $H = VDV^{-1}$, V has also to be taken in the symmetric form of:

$$V = \begin{pmatrix} X & Y \\ Y & X \end{pmatrix} \qquad H = \begin{pmatrix} A & B \\ -B & -A \end{pmatrix}$$

5

Numerically, this is not going to happen, we have to regulate the column vectors, to satisfy the symmetry. In order to solve this subtly, I am going to follow two steps:

1. **Change the basis**

   Change the basis from $(c^\dagger, c)$ to $(c^\dagger + c, c^\dagger - c)$

   $$\begin{pmatrix} \phi & 0 \\ 0 & \psi \end{pmatrix} = \begin{pmatrix} X + Y & 0 \\ 0 & X - Y \end{pmatrix} \qquad \begin{pmatrix} c^\dagger + c \\ c^\dagger - c \end{pmatrix} = \begin{pmatrix} \phi & 0 \\ 0 & \psi \end{pmatrix} \begin{pmatrix} \gamma^\dagger + \gamma \\ \gamma^\dagger - \gamma \end{pmatrix}$$

   Under this new basis, the Hamiltonian kernel becomes:

   $$\begin{pmatrix} 0 & M^T \\ M & 0 \end{pmatrix} \qquad \text{where } M = A + B \quad M^T = A - B$$

2. **Singular value decomposition (SVD)** [36]

   $$M = \phi \Lambda \psi^T \tag{1.17}$$

   SVD is numerically stable. Here:

   The diagonal terms of Λ are eigenvalues of the system, they are non-negative.

   ψ and ϕ are orthogonal matrices.

From the result of Equation (1.17), we can then calculate Equation (1.8).

$$\begin{pmatrix} c^\dagger + c \\ c^\dagger - c \end{pmatrix} = \begin{pmatrix} \phi & 0 \\ 0 & \psi \end{pmatrix} \begin{pmatrix} \gamma^\dagger + \gamma \\ \gamma^\dagger - \gamma \end{pmatrix} \tag{1.18}$$

$$\left\langle \begin{pmatrix} \gamma^\dagger + \gamma \\ \gamma^\dagger - \gamma \end{pmatrix}_t \begin{pmatrix} \gamma^\dagger + \gamma & -\gamma^\dagger + \gamma \end{pmatrix}_0 \right\rangle = \begin{pmatrix} P & -P \\ -P & P \end{pmatrix} \tag{1.19}$$

$$P = \delta_{ij} e^{+i(\epsilon_i - \bar{\epsilon}_i)t} = e^{i2\Lambda t}$$

$$M_t = \begin{pmatrix} \phi & 0 \\ 0 & \psi \end{pmatrix} \begin{pmatrix} P_t & -P_t \\ -P_t & P_t \end{pmatrix} \begin{pmatrix} \phi^\dagger & 0 \\ 0 & \psi^\dagger \end{pmatrix} \begin{pmatrix} 1 & 0 \\ 0 & -1 \end{pmatrix}$$

The equivalence of the basis. It can be shown that, these representations are equivalent, provided:

$$V = \begin{pmatrix} X & Y \\ Y & X \end{pmatrix} \qquad \begin{pmatrix} \phi & 0 \\ 0 & \psi \end{pmatrix} = \begin{pmatrix} X+Y & 0 \\ 0 & X-Y \end{pmatrix}$$

The constraint

$$V^\dagger V = \begin{pmatrix} X^\dagger & Y^\dagger \\ Y^\dagger & X^\dagger \end{pmatrix} \begin{pmatrix} X & Y \\ Y & X \end{pmatrix} = \begin{pmatrix} I & 0 \\ 0 & I \end{pmatrix}$$

is equivalent to

$$X^\dagger X + Y^\dagger Y = I \tag{1.20}$$

$$X^\dagger Y + Y^\dagger X = 0 \tag{1.21}$$

We can make some modification $(1.20) \pm (1.21)$, to have

$$(X \pm Y)^\dagger (X \pm Y) = I$$

Which is the complete information of orthogonalness of ϕ and ψ:

$$\psi^\dagger \psi = \phi^\dagger \phi = I \tag{1.22}$$

Note: the above is for column orthogonalness, the row orthogonalness can be derived from $VV^\dagger = I$

Comments: the benefit of ϕ ψ over X Y is , the former is decoupled from each other.

Majorana basis. We can also multiple an $\sqrt[2]{-1}$ to the $c_i^\dagger - c_i$, making the basis Majorana fermions operators.

$$\begin{pmatrix} a_i \\ b_i \end{pmatrix} = \begin{pmatrix} c_i^\dagger + c_i \\ -i(c_i^\dagger - c_i) \end{pmatrix} \tag{1.23}$$

$$\hat{H} = \begin{pmatrix} a & b \end{pmatrix} \frac{i}{2} \begin{pmatrix} 0 & B - A \\ A + B & 0 \end{pmatrix} \begin{pmatrix} a \\ b \end{pmatrix} \tag{1.24}$$

a_i and b_i are Majorana fermion operators at site i satisfying

$$a_i^\dagger = a_i \quad b_i^\dagger = b_i \quad \{a_i, a_j\} = 2\delta_{ij} \quad \{b_i, b_j\} = 2\delta_{ij} \quad \{a_i, b_j\} = 0 \tag{1.25}$$

The kernel $\begin{pmatrix} 0 & -M^T \\ M & 0 \end{pmatrix}$ is skew-symmetric matrix. The canonical form [24] is given by:

$$H_{canonical} = \frac{i}{2} \sum_m 2\epsilon_m \tilde{a}_m \tilde{b}_m \tag{1.26}$$

Where $\tilde{a}_m, \tilde{b}_m$ are Majorana operators, satisfying the same commutation as Equation 1.25. It can be prove that, they are related by right and left singular vectors of SVD $M = \phi \Lambda \psi^T$:

$$\tilde{a}_m = \sum_i \phi_{mi} a_i \tag{1.27a}$$

$$\tilde{b}_m = \sum_i \psi_{mi} b_i \tag{1.27b}$$

1.2.2 The Pfaffian technique for spin-spin correlations

Equation (1.8) can be labeled as:

$$M_{L,h_i,\lambda_i,\lambda_i}(\pm, \pm, m, n, t, t') = < \left(c_m^\dagger(t) \pm c_m(t) \right) \left(c_n^\dagger(t') \pm c_n(t') \right) > \tag{1.28}$$

$$= \left\langle \begin{pmatrix} c^\dagger + c \\ c^\dagger - c \end{pmatrix}_{t-t'} \begin{pmatrix} c^\dagger + c & -c^\dagger + c \end{pmatrix}_0 \right\rangle \begin{pmatrix} 1 & 0 \\ 0 & -1 \end{pmatrix}$$

From here we can construct many physical quantities, with the help of Pfaffian. **Construction of** $< \sigma_i^x(t)\sigma_j^x(0) >$

$$< \sigma_i^x(t)\sigma_j^x(0) >= \text{Pf}(S)$$

Here S is a $2(i+j-1)$ dimensional skew-symmetric matrix, its elements are taken from the elements of matrix M_0 and M_t in Equation 1.8.

$$S_{m,n} = M_{t'}(m', n') \quad m < n \tag{1.29}$$

The indexes mapping relation can be found by expanding Equation 1.7

1. $m < n \leq (2i - 1)$

    $t' = 0$

    $m' = [m/2] + L * [\textbf{if } m\%2 == 0]$

    $n' = [n/2] + L * [\textbf{if } n\%2 == 0]$

2. $m \leq (2i - 1) < n$

    $t' = t$

    $m' = [m/2] + L * [\textbf{if } m\%2 == 0]$

    $n' = [(n - (2i - 1))/2] + L * [\textbf{if } (n - (2i - 1))\%2 == 0]$

3. $(2i - 1) < m < n$

    $t' = 0$

    $m' = [(m - (2i - 1))/2] + L * [\textbf{if } (m - (2i - 1))\%2 == 0]$

    $n' = [(n - (2i - 1))/2] + L * [\textbf{if } (n - (2i - 1))\%2 == 0]$

Here $[m/2]$ means the celling, e.g. $[1/2] = 1 \quad [2/2] = 1 \quad [3/2] = 2$

$[\textbf{if } m\%2 == 0]$ gives one or zero, depends on the reminder.

For $m > n$, it is given by $S_{m,n} = -S_{n,m}$

After we got the $2(i+j-1) \times 2(i+j-1)$ dimensional matrix, we are going to calculate its pfaffian. The actual numeric algorithm for Pfaffian are carried out, using method given in Xun's paper [22].

Figure 1.1 is an example of spin-spin real time calculations, the spin is chosen on the same site. The axis are real and imaginary part of $< X_{20}(t)X_{20}(0) >$. At time zero, the value starts at $(1,0)$, then it evolves in a spiral pattern. The second graph, show the same system, but with longer evolving time, the orange trajectory, is irregular. This is a boundary effect, the correlation feels the boundary after certain time.
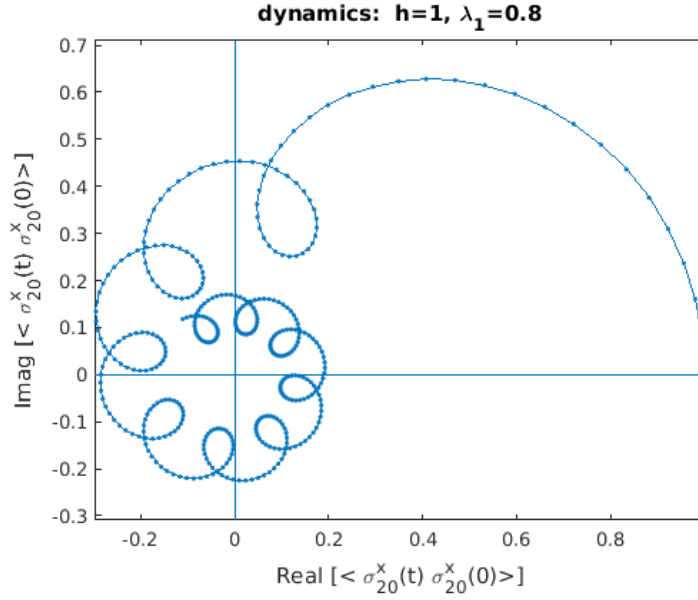
(a) spiral patterns
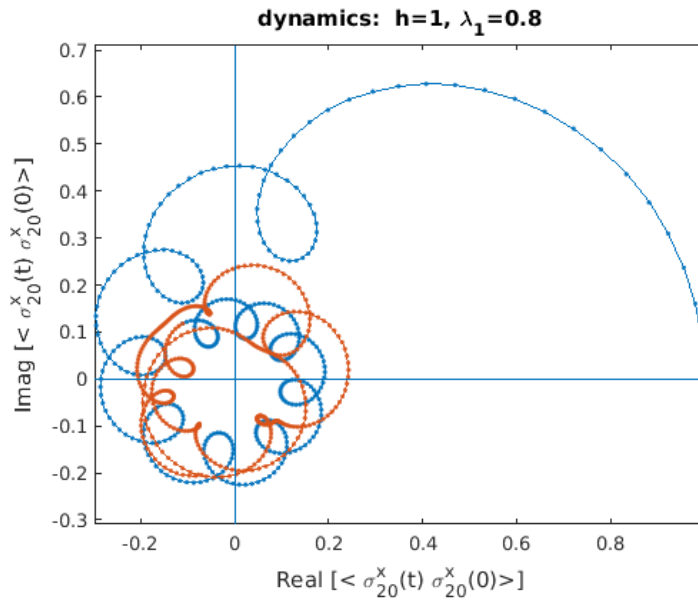
(b) longer time, boundary effects

Figure 1.1: Real and imaginary part of $z(t) = < \sigma_{20}^x(t)\sigma_{20}^x(0) >$

80 sites, paramagnetic phase: $h = 1$ $\lambda_1 = 0.8$

(a) the regular spiral pattern

(b) at longer time, the boundary influence come in ,the irregular pattern.

11

Figure 1.1 is in paramagnetic phase ($h = 1, \lambda_1 = 0.8$), the spin-spin correlation will approach zero after long enough time. In Figure 1.2, I show a critical point dynamics ($h = \lambda_1 = 1$). Compared with Figure 1.1, the critical dynamics of Figure 1.2 is slower, and more irregular: it start from point $(1, 0)$ at zero time, evolve in a spiral way shifting to the left. Then after passing throw the imaginary axis, it moves in a irregular pattern. It remains a question, whether this is due to the finite size boundary effect, or due to the critical behavior. Or does irregular pattern have something to do with chaos.
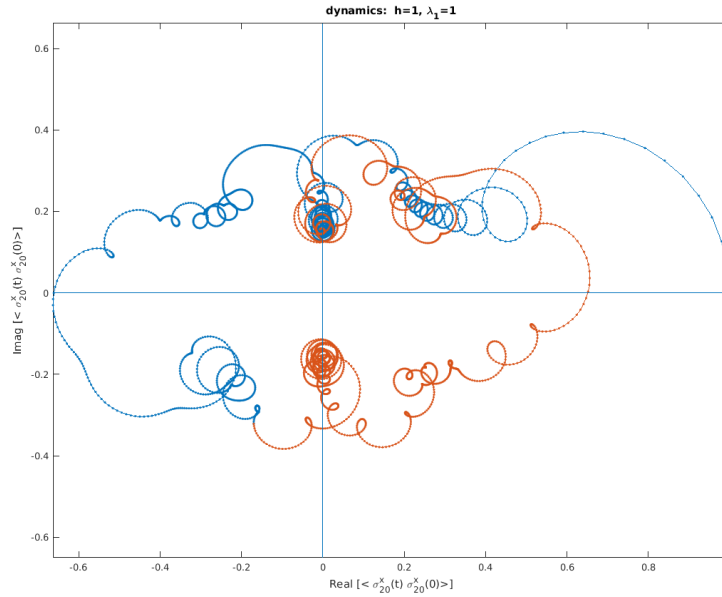
Figure 1.2: Plot of spin-spin correlation $z(t) =< X_{20}(t)X_{20}(0) >$ at quantum criticality $h = \lambda_1 = 1$, with 80 sites system
the critical dynamics is slow, and irregular compared to the paramagnetic phase dynamics Figure 1.1

1.2.3 Pure system

Figure 1.3 is the phase diagram of the pure 3-spin model [32]. The transverse field $h = 1$ is set to unity. The horizontal line $\lambda_2 = 0$ corresponds to the transverse field Ising model, with critical point at e. In this phase diagram, the $n = 1$ regions correspond to the magnetically

ordered regions.

To explore the dynamics in the phase diagram, we plot a few examples of $S(k, \omega)$ in figure FIG.1.4 ($h = 1, \lambda_1 = 0.5, \lambda_2 = 0$) ; FIG. 1.5 ($h = 1, \lambda_1 = 1, \lambda_2 = -0.5$); FIG. 1.6 ($h = 1, \lambda_1 = 1, \lambda_2 = 1$). Note that Fig. 1.6 is in the magnetically ordered region $n = 1$; m^2 has been subtracted from the spin-spin correlation function, and the excitation is two-particle continuum.

1.3 Emergent low energy modes in disorder chain

In this chapter, let's only consider the 2-spin interaction $H_2 = -\sum_{i=1}^{L} h_i \sigma_i^z - \sum_{i=1}^{L-1} \sigma_i^x \sigma_{i+1}^x$ with $\lambda_1 = 1$ and $\lambda_2 = 0$, the random transverse field has the binary distribution: the larger field h_L and the smaller field h_S, with probability $P_L + P_S = 1$ As P is changed from 0 to 1, we will show that, for $0 < h_S < 1 < h_L$ there is a phase transition as we change P, and there will be low energy emergent modes. Consider, $h_L = 3.0, P_L = 0.6,$ and $h_S = 0.2, P_S = 0.4$ For these parameters we get the spectra shown in Fig. 1.7. The spectral density has a very strong peak near the zero energy $\omega = 0$, and near $k = 0$. At high energies, the spectra breaks up into horizontal stripes. The central question of this paper is to understand what is the natural of the low energy signals.
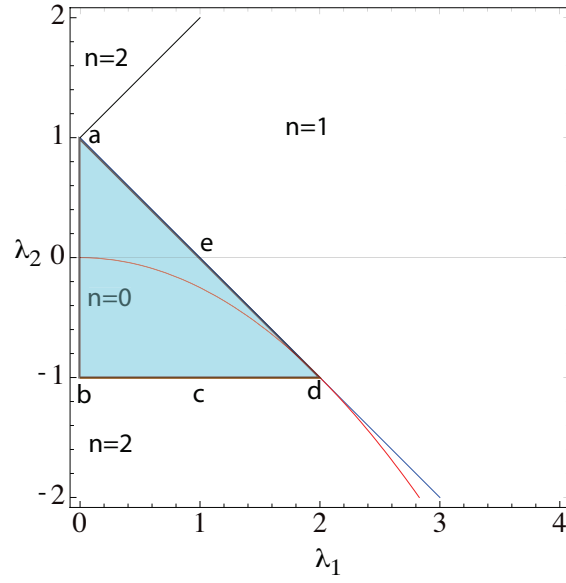
(a) theoritical prediction
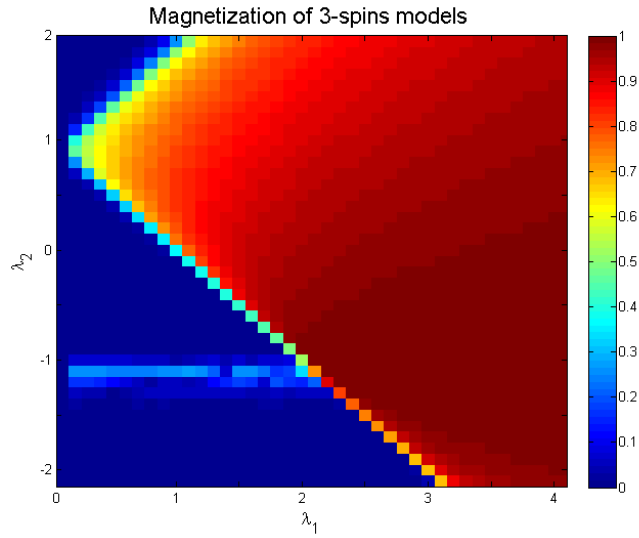
(b) numerical result (color is magnetization per site)

Figure 1.3: Pure system phase diagram of 3-spin model H. The transverse field is taken to be unity. The labels $n = 0, 1, 2$ are the topological numbers, denoting pairs of Majorana modes at open boundaries.
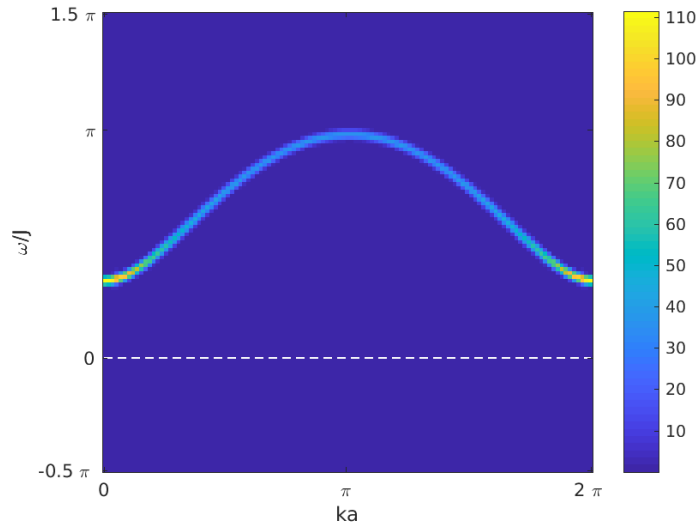
Figure 1.4: The dynamical structure factor 120 sites, paramagnetic phase: $h = 1$ $\lambda_1 = 0.5$ $\lambda_2 = 0$
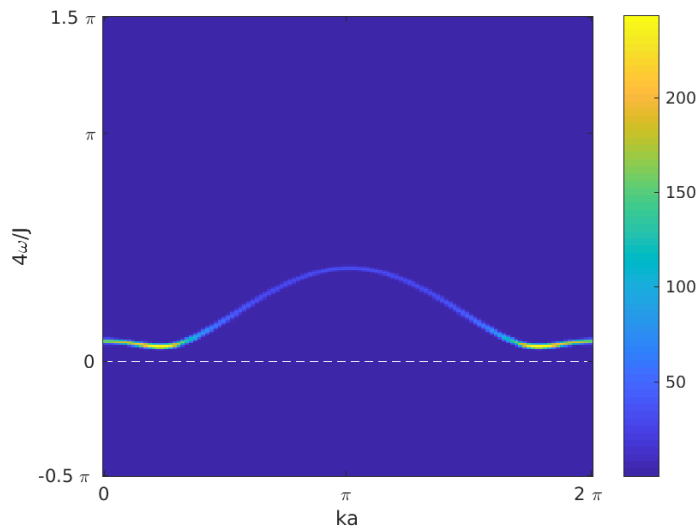
Figure 1.5: Dynamical structure factor of pure system $h = \lambda_1 = 1$ $\lambda_2 = -0.5$, 120 sites the dispersion curve has a dip at non-zero k value, that gap can also be closed at non-zero k by tuning parameters
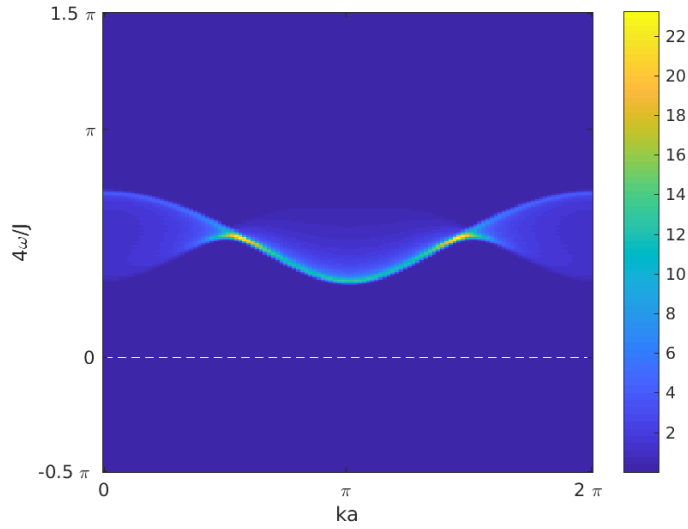
Figure 1.6: Dynamical structure factor of pure system $h = \lambda_1 = \lambda_2 = 1$, 120 sites this is in the two particles continuum region, single spinon excitation is forbidden in this $n = 1$ phase
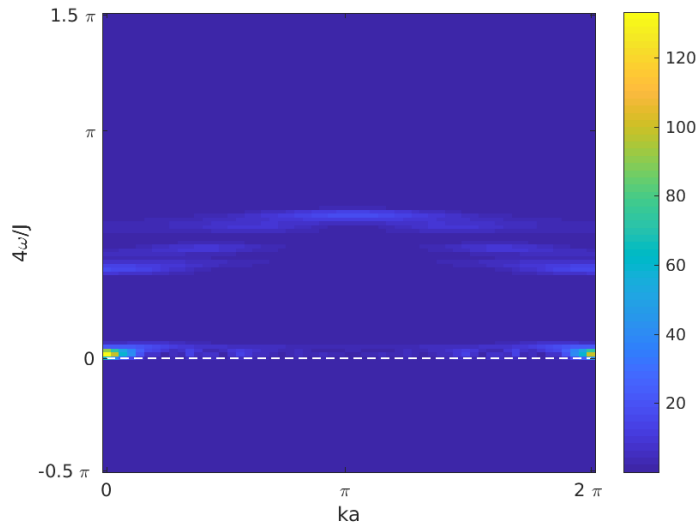
Figure 1.7: $S(k,\omega)$ of a 2-spin model: the quenched disorder transverse field h_i satisfies binary distribution with $P(h_i = 3.0) = 0.6$ and $P(h_i = 0.2) = 0.4$

To answer the question, let's fix h_S and h_L, and take P as a tuning parameter. Then it can be converted into another question: how do the zero energy modes emerge as a function

16

of P? We plotted the density of states in Fig. 1.8. There are 11 graphs for different P values. The $P_L = 0.6$ corresponds to Fig. (1.7). Notice that, density of state $\rho(\omega)$ and integrated $\int S(k,\omega)dk$ are related, but not identical.

In FIG. 1.8, the two extreme cases $P = 0$ and $P = 1$ are gapped, with no zero energy modes. For intermediate values, we can see the zero energy modes.
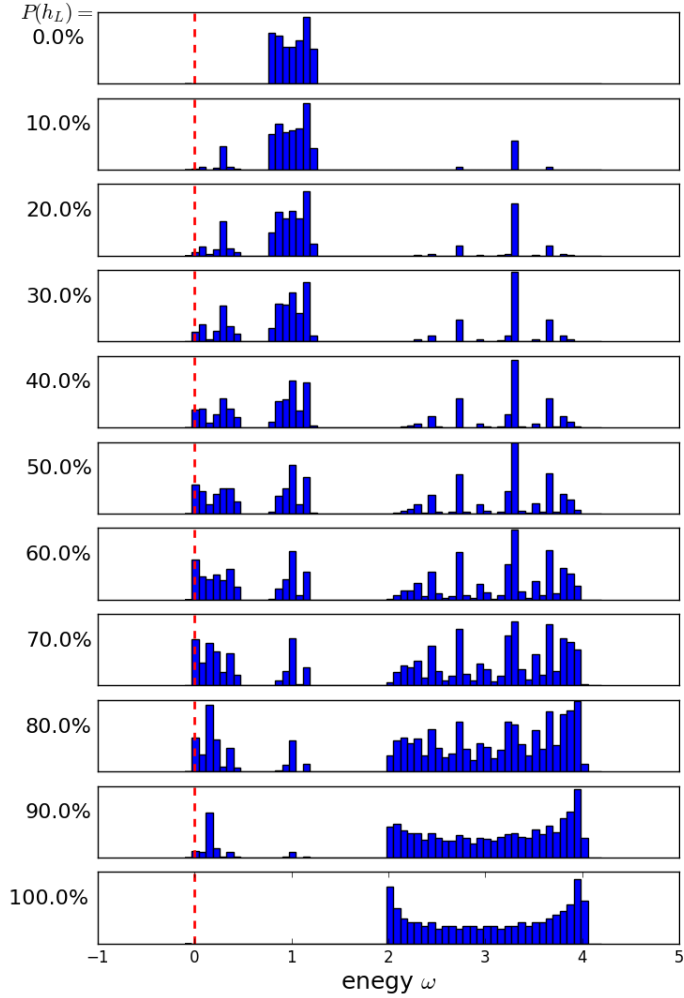
Figure 1.8: 11 density of state plots for system with binary transverse field disorder. All of the graphs have the same large field $h_L = 3.0$ and small field $h_S = 0.2$, the difference is their binary disorder percentage. The two extreme D.O.S. plots on the top $P = 0\%$ and in the bottom $P = 100\%$ correspond to pure system in ferromagnetic phase and in paramagnetic phase. From top to bottom, the probability of large field is increasing, the probability of small field is decreasing

In FIG 1.9, we plot the density of states near the zero energy, on a log-scale. It capture

the details about how the gap is closed. We find that, near $P = 0.6$ the zero mode disappears.
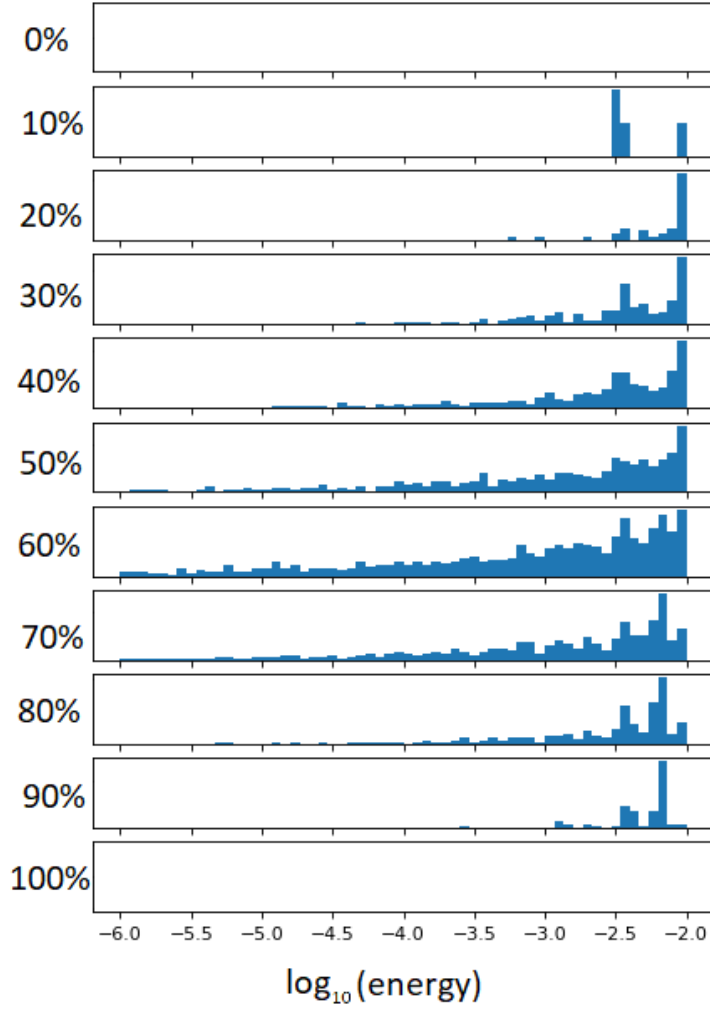
Figure 1.9: Density of state plot near zero energy of FIG 1.8. The horizontal axis is in $\log_{10}$ scale. This detailed study shows that, although the gap looks closed for all disorder case in FIG. 1.8, there is a optimal percentage, where the closing is the best

From Fig. 1.8, we can also find the excitations are grouped into three regions.

1. $h_L - 1 < \omega < h_L + 1$ corresponds to the excitations in the paramagnetic region.

2. $1 - h_S < \omega < 1 - h_S$ corresponds to the ferromagnetic phase. The two-particle continuum excitations is not obvious in $S(k, \omega)$ graph.

3. $\omega < \omega_0$ corresponds to the emergent low energy modes.

The energy is always bounded by these groups, no matter what the disorder is. For the emergent low energy modes do not always exist. By tuning h_L, h_S, we find:

- It exists when large field and small field straddle the critical point $0 < h_S < 1 < h_L$. For the cases of $1 < h_S < h_L$ or $0 < h_S < h_L < 1$, no low energy mode emerges, no matter what P is.

- In the proper case $0 < h_S < 1 < h_L$, there is a value of P which generates maximum numbers of low energy modes, and the gap is minimized. We will show that such a point is the infinite randomness fixed point, give by $\overline{\ln h_i} = \overline{\ln J_i}$ [?]

1.3.1   The critical point

In the two extreme cases in Fig. 1.8, i.e. with no disorder, $P = 0$. represents the ferromagnetic phase, and $P = 1$ represents the para-magnetic phase. At an intermediate value of P_L the system must have a quantum phase transition. The critical value of P_C is given by:

$$\overline{\ln h_i} = \overline{\ln J_i}$$
$$h_L^{P_C} h_S^{1-P_C} = 1$$
$$P_C = \frac{\ln h_S}{\ln h_S - \ln h_L} \tag{1.30}$$

In Fig. 1.10 the magnetization is plotted, for $h_S = 0.2$ $h_L = 3.0$, the vertical line is the critical value $P_C = \frac{\ln 0.2}{\ln 0.2 - \ln 3.0} \approx 0.5943$. The magnetization is calculated by $m = \sqrt{\langle \sigma_{+\infty}^x(0) \sigma_0^x(0) \rangle}$, with 129 random configurations for the ensemble average. Due to the randomness, the magnetization takes large computational resources in the averaging procedure.
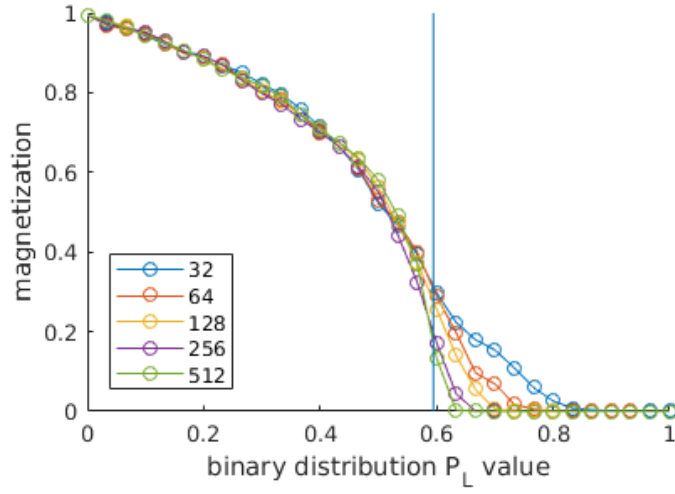
Figure 1.10: Magnetization as a function of binary distribution parameter P, the random transverse field $h_i \sim P\delta(h - h_L) + (1 - P)\delta(h - h_S)$. $h_L = 3.0$ $h_S = 0.2$ we can see the critical behavior predicted by $P_C = \frac{\ln h_S}{\ln h_S - \ln h_L} = 0.59$

The Fig. 1.11 is the energy gap plotted against P. In our calculation, we choose periodic boundary condition for the fermions. We also choose logarithmic scale for the energy. Without the log-scale, they all look close to zero; see Fig. 1.8.
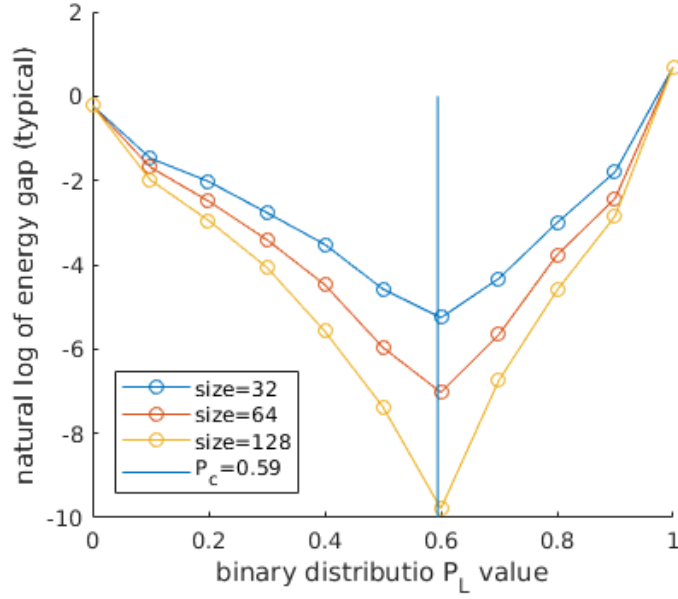
Figure 1.11: Log of energy gap as a function of binary distribution parameter P , the random transverse field $h_i \sim P\delta(h - h_L) + (1 - P)\delta(h - h_S)$. $h_L = 3.0$ $h_S = 0.2$ we can see the critical behavior predicted by $P_C = \frac{\ln h_S}{\ln h_S - \ln h_L} = 0.59$. Notice that the ensemble average is typical average, it is mean$\{\epsilon_{gap_i}\}$, not the min$\{\epsilon_{gap_i}\}$

The Figs. 1.8, 1.10, and 1.11 have already shown that, the critical point exists, and it is predicted by Eq. (1.30). The Figs. 1.12 and 1.13 demonstrate the activated scaling at the quantum critical point; the energy gap is proportional to $e^{-\alpha\sqrt{L}}$
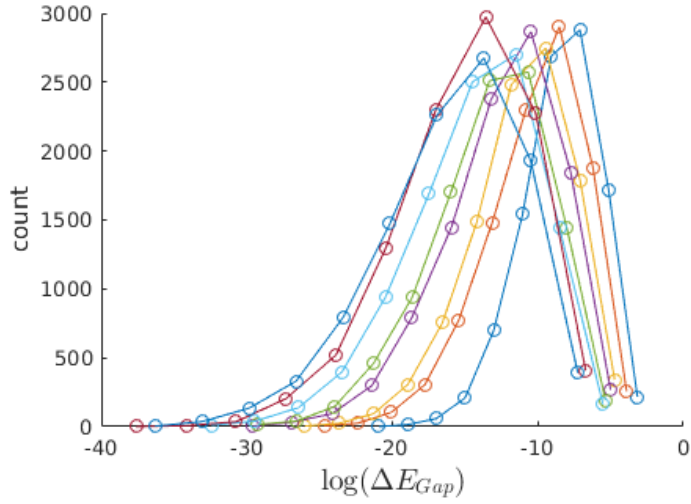
Figure 1.12: Gap distributions for different system sizes. horizontal axis is log of energy gap $\log(\Delta E)$; vertical axis is the distribution count. system size from right to left $L = 32, 48, 64, 80, 96, 112, 128, 114$; average of 10000 random samples
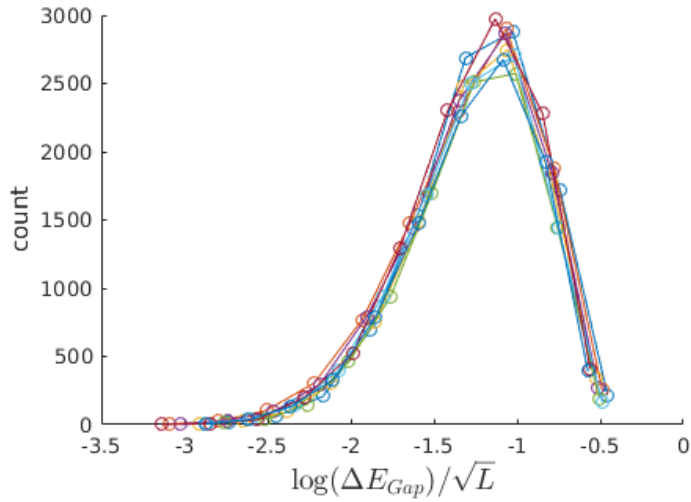
Figure 1.13: The collapse of the data in Fig. 1.12. The horizontal axis is rescaled by the squared root of the system size. This collapse only happens at the critical point $P_C = 0.59$

1.4 Griffiths-like phase and the Majorana zero modes

In the last section we have shown that there is a phase transition as a function of P, and the low energy modes emerge close to the critical point. In this section, we will explore the nature of the low energy modes.

1.4.1 Disorder induced rare regions

We know that in a pure system, Majorana modes exist at the boundaries of a topologically non-trivial phase. In a disordered system, since the system is not uniform, it is possible that a spatial region is in the non-trivial phase, while the surrounding is still in the trivial phase. Thus the low energy Majorana zero modes are created by rare regions of magnetization, the "Griffiths phase".

To understand, let's plot the equal time spin-spin correlation function for a specific random configuration:

$$< \sigma_n^x \sigma_m^x > \tag{1.31}$$

n and m run from 1 to L; so this plot contains the correlation of each pair at equal times. Here are some important properties: (1) the diagonal term is always unity, $< \sigma_n^x \sigma_n^x >= 1$; (2) it is symmetric under $m \leftrightarrow n$; (3) it is real because, $< \sigma_n^x \sigma_n^x >^* =< \sigma_n^x \sigma_n^x >$

From Fig. 1.14, one can see the rare regions clearly by watching which site is correlated with which site.
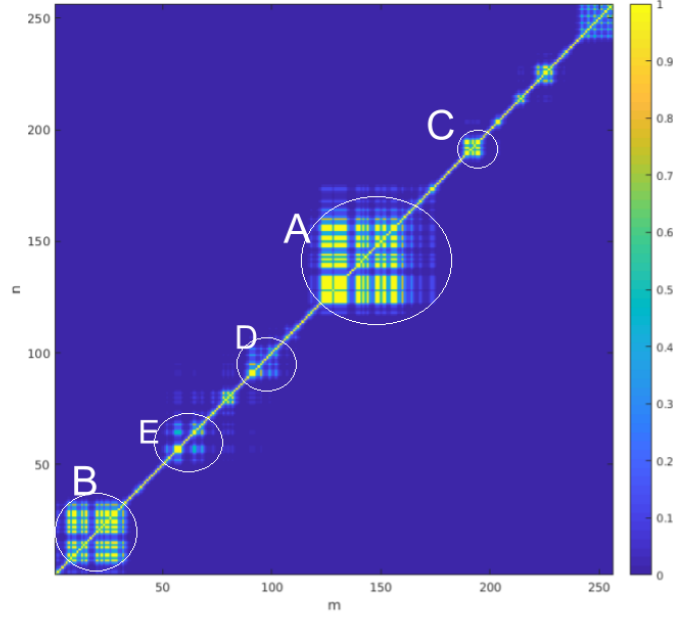
Figure 1.14: Equal time spin-spin correlation $< \sigma_n^x \sigma_m^x >$, the horizontal axis is m the vertical axis is n, the color is the strength of $< \sigma_n^x \sigma_m^x >$

It is a spin-spin correlator plot: $h_L = 3.0$ with 60% probability and $h_S = 0.2$ with 40% probability. We can see the cluster of rare regions A,B,C,D,E. The largest region A spans about 30 sites from 125 to 160, it is where the small field $h_S = 0.2$ are gathered. Since the field is weak there, the spins tend to be coupled by interaction, and correlated to form magnetic order. Although, at certain sites, the cluster may contain large field, the cluster is not broken by it. At a coarse grained level, it is single giant spin.

The quadratic fermion Hamiltonian in Eq. 1.4, can also be rewritten in the of Majorana representation: $a_i = c_i^\dagger + c_i$ and $b_i = i(c_i^\dagger - c_i)$ The Hamiltonian is then

$$H = i \sum_{i=1}^{L} h_i b_i a_i + i \sum_{i=1}^{L-1} \lambda_{1i} b_i a_{i+1} + i \sum_{i=1}^{L-2} \lambda_{2i} b_i a_{i+2} \tag{1.32}$$

Equation 1.32 can be solved with singular value decomposition, into decoupled Majorana pairs:

$$H = i \sum_{n=1}^{L} \epsilon_n \tilde{a}_n \tilde{b}_n \tag{1.33}$$

25

The Fig. 1.15 shows the five lowest eigenvectors of $\tilde{a}_n = \sum_i \psi_{ni} a_i$ and $\tilde{b}_n = \sum_i \phi_{ni} b_i$, the vertical axis labels the eigenenergy $\epsilon_n = \Lambda_{nn}$.

These Majorana pairs are the eigenstates representing the many-body excitations. From top to bottom, those Majorana pairs in Fig. 1.15 correspond to the rare regions A,B,C,D,E in Fig. 1.14

- Majorana pairs reside at the boundary of magnetic rare regions.

- If the magnetic rare region's boundary is not sharp, the Majorana mode will span a large distance

- When the Majorana pairs get closer, their energy increase
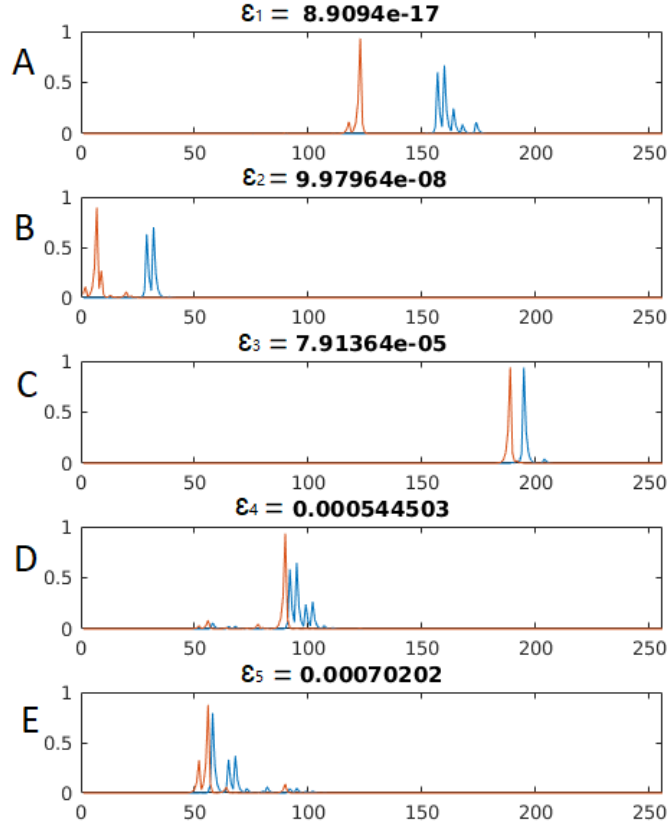
Figure 1.15: Five lowest eigenvectors, titles are the energy ϵ_n, index n is in ascending order of eigen-energy. The horizontal axis is the lattice site, the vertical axis is the value of ψ_{ni} and ϕ_{ni}. The orange and blue curves correspond to decoupled Majorana pairs real part $\tilde{a}_n = \sum_i \psi_{ni} a_i$ and imaginary part $\tilde{b}_n = \sum_i \phi_{ni} b_i$. A,B,C,D,E graphs correspond to the rare regions in FIG. 1.14

1.4.2 The separation between the Majorana zero mode pairs

The separation size of a Majorana pair is defined by:

$$s_n = |\frac{\sum_i i|\psi_{in}|^2}{\sum_i |\psi_{in}|^2} - \frac{\sum_i i|\phi_{in}|^2}{\sum_i |\phi_{in}|^2}| \tag{1.34}$$

the n labels the different eigenmodes; i is the lattice site. The above definition works for any Majorana eigenvectors (not necessarily the zero mode) . But we are interested in the behavior

of the low energy modes, because for high energy modes, ψ_{in} and ϕ_{in} will significantly overlap, and s_n will be trivially small.

We define $n = 1$ to be the lowest energy mode (eigenvalues are in ascending order). Then s_n will be the largest separation distance. We plot the distribution of relative sizes, s_n/L, for a random ensemble, at the critical point (infinite randomness fixed point).
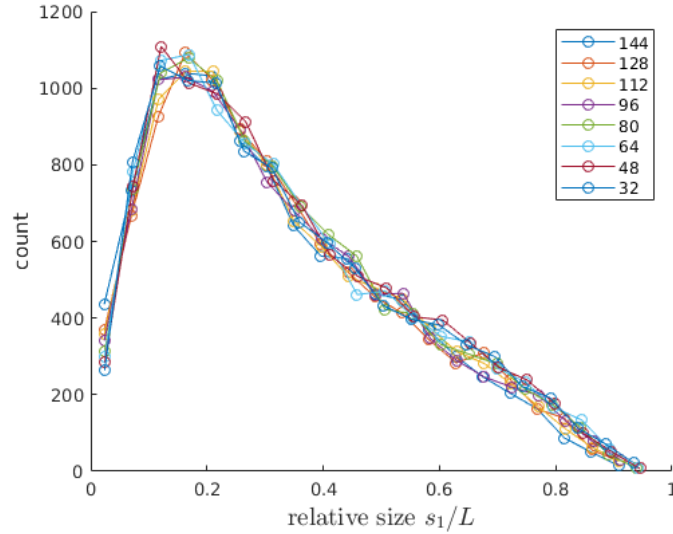
Figure 1.16: The distribution of the size of Majorana pair seperation at the critical point $P = P_C = 60\%$

We can see from the Fig. 1.16, at the critical point, that the separation distance of Majorana pairs scales linearly with the system size, all system sizes collapse. This is fractal behavior, the distribution of rare region size, looks the same at all length scale. And the size distribution is very broad. large sizes have high probabilities.

In contrast, in Fig. 1.17 is plotted the size distribution in the off-critical case. The distribution is very narrow, most of them is less than 0.3 of the system size. These don't collapse on the same distribution curve, as the system size increases; the distribution shifts to the left, which means that the relative size of rare regions are getting smaller and smaller. This does not mean that the rare regions will vanish in the thermodynamic limit $L \to \infty$. The the size of the rare regions may still grow as $s_1 \sim L^\theta$, but with $\theta < 1$. And the

macroscopic number of zero modes will contribute to the non-universal power law behavior of the thermodynamics properties.
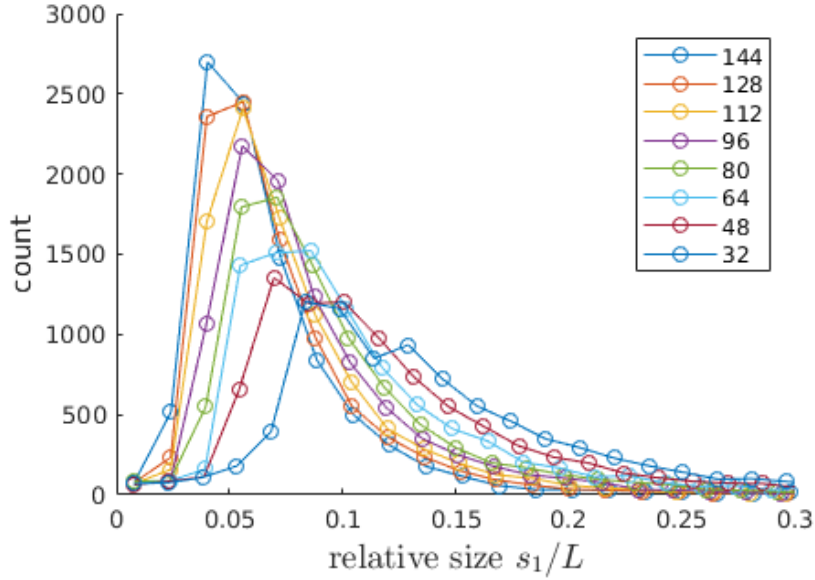
Figure 1.17: The distribution of the size of Majorana pair seperation, off the critical point $P = 40\%$

Now, the low energy mode in the previous chapter can be explained by the emergent Majorana modes. The Eq. 1.34 is much easier to calculate than the spin-spin correlation function, and the rare region information can be derived from the Majorana picture.

1.5 Disorder with longer range interaction

1.5.1 Induced Majorana modes

Let λ_1 be non-zero. The results are given in Fig. 1.18 and Fig. 1.19; the rare region diagram is shown in Fig. 1.20. Due to the competition between λ_1 and λ_2, the Majorana zero mode oscillation pattern shifts to a new k value, between 0 and π. In Fig. 1.18, we can see the zero energy modes exist below the minimum of the dispersion curve. This is a very general phenomenon, the zero mode in the disordeed system is usually located where the pure system

has the smallest gap. The calculation is carried with the following Hamiltonian. Note that, the rare region C is inside another rare region A in Fig. 1.19.

$$H = -\sum_{i=1}^{L} h_i \sigma_i^z - 0.4 \sum_{i=1}^{L-1} \sigma_i^x \sigma_{i+1}^x + \sum_{i=1}^{L-2} \sigma_i^x \sigma_{i+1}^z \sigma_{i+2}^x$$

$$h_i = \begin{cases} h_L = 1.6 & \text{probability} = 95\% \\ h_S = 0.1 & \text{probability} = 5\% \end{cases} \tag{1.35}$$
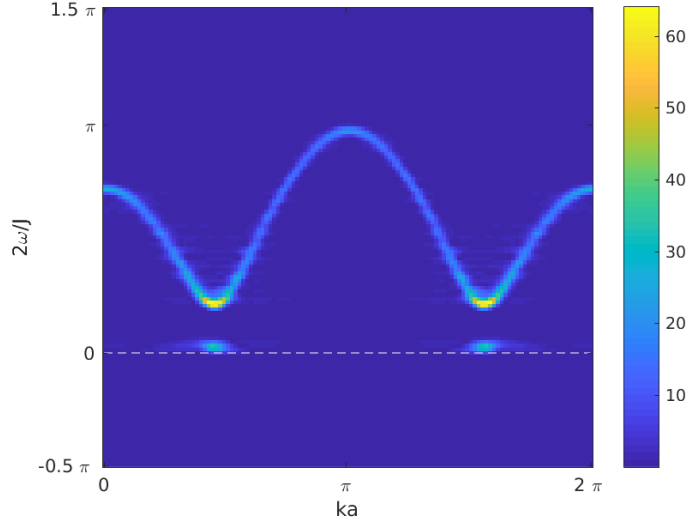
Figure 1.18: $S(k,\omega)$ for the binary distribution of the transverse field: $P(h_L = 1.6) = 95\%$ $p(h_S = 0.1) = 5\%$; here $\lambda_1 = 0.4$ $\lambda_2 = -1.0$
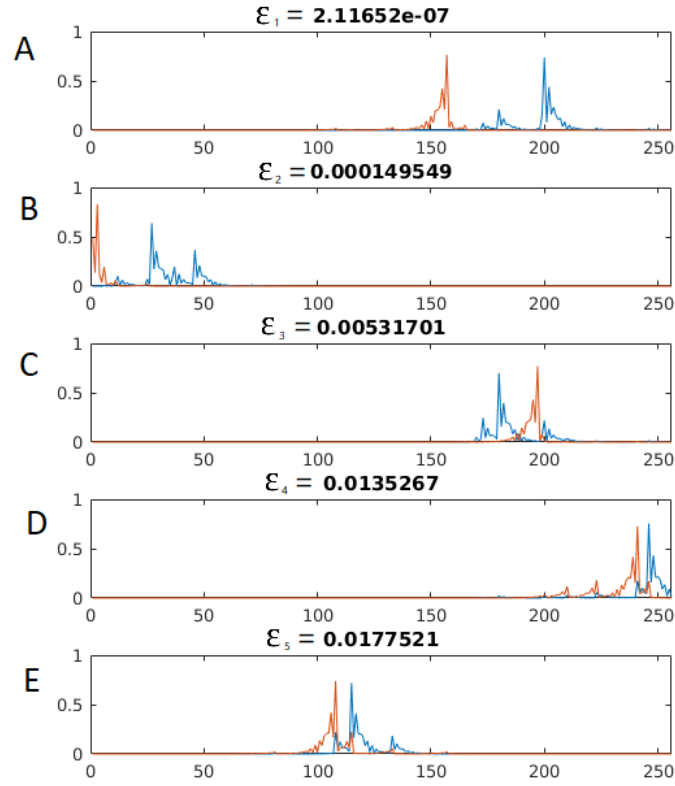
Figure 1.19: Five lowest eigenvectors, titles are the energy ϵ_n, index n is in ascending order of eigen-energy The horizontal axis is the lattice site, the vertical axis is the value of ψ_{ni} and ϕ_{ni}. The orange and blue curves correspond to decoupled Majorana pairs real part $\tilde{a}_n = \sum_i \psi_{ni} a_i$ and imaginary part $\tilde{b}_n = \sum_i \phi_{ni} b_i$. A,B,C,D,E graphs correspond to the rare regions in FIG. 1.20
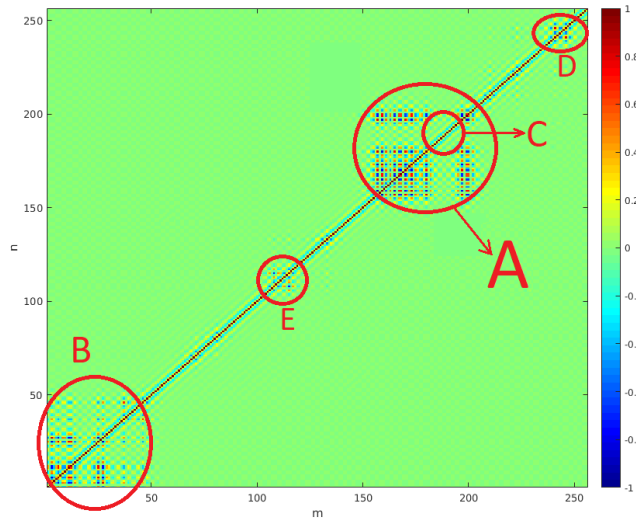
Figure 1.20: Equal time spin-spin correlation $< \sigma_n^x \sigma_m^x >$, the horizontal axis is m the vertical axis is n, the color is the strength of $< \sigma_n^x \sigma_m^x >$

1.5.2 Spin glass phase

In the three spin problem, we set the transverse field and the next nearest coupling to be

$$h = 1 \qquad \lambda_2 = -0.3$$

The nearest couplings λ_{1i} are chosen to be random variables, satisfying the uniform distribution. $[\lambda_1 - \delta J, \lambda_1 + \delta J]$. With λ_2 provides frustration and λ_{1i} provides disorder, we expect to see a spin-glass phase transition for enough disorder strength δJ

The spin glass [SG] order is defined by:

$$\chi_{SG} = \Big[\sum_{i,j=1}^{L} \langle \sigma_i^x \sigma_j^x \rangle^2 \Big]$$

There are L^2 terms in the summation, the square parenthesis corresponds to disorder average.

- When all sites are correlated, deep in the SG phase,

$$\chi_{SG} \sim L^2$$

32

- In the other extreme case, non-SG phase, i and j are correlated only within some distance ξ

$$\chi_{SG} \sim \xi L$$

In the Fig. 1.21, we plot χ_{SG}/L^2
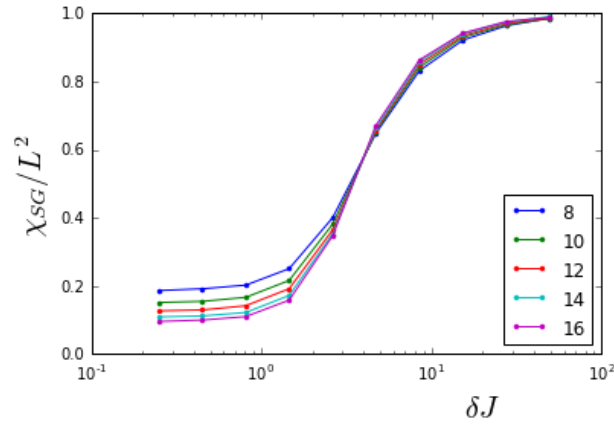
Figure 1.21: Spin glass order for different system sizes. There is a phase transition near the disorder strength $\delta J_c \approx 4$
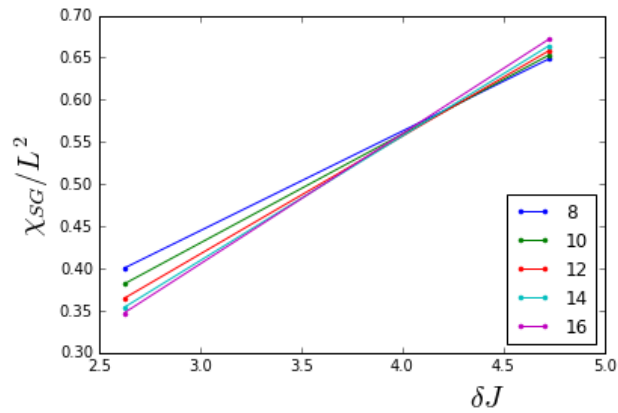
Figure 1.22: Zoom of the plot of the spin glass order Fig. 1.21, the critical point is near $\delta J_c \approx 4$

1.6 Conclusion

In this paper, We have shown that, quenched binary disorder can induce rare regions, and there can be zero energy Majorana modes at the boundaries of these regions. The existing condition of low energy mode is, the disorder parameters have to take values from different phases. The quality(gap closing and number percentage) of the low energy mode will reach a peak value at the infinite randomness fixed point. The separation distance distribution of lowest energy Majorana mode pairs, is defined. This quantity is very easy to calculate. We have shown it will have fractal behavior at the critical point, at the most probable size of Majorana mode is about $1/5$ of the system size. With longer range interaction turning on, the rare region induced MZM picture still hold, and a spin-glass phase transition is observed as the result of both frustration and disorder.

1.7 Diagonalizing a Hamiltonian with particle-hole symmetry

After the Jordan-Wigner transformation, we get a single particle Hamiltonian Equation (1.4), we can also write it in a compact Nambu basis $\Psi^\dagger = (c_1^\dagger, \cdots, c_L^\dagger, c_1, \cdots, c_L)$

$$H = \Psi^\dagger \begin{pmatrix} A & B \\ -B & -A \end{pmatrix} \Psi \tag{1.36}$$

where $A = \frac{1}{2}(M + M^T)$ and $B = \frac{1}{2}(M - M^T)$. M is an $L \times L$ dimensional matrix, which contains all the information of transverse fields and couplings:

$$M = \begin{pmatrix} h_1 & -\lambda_{11} & -\lambda_{21} & & & \\ & h_2 & -\lambda_{12} & -\lambda_{22} & & \\ & & h_3 & -\lambda_{13} & \ddots & \\ & & & \ddots & \ddots & -\lambda_{2,L-2} \\ & & & & \ddots & -\lambda_{1,L-1} \\ & & & & & h_L \end{pmatrix} \tag{1.37}$$

We can diagonalize the Hamiltonian kernel $\begin{pmatrix} A & B \\ -B & -A \end{pmatrix}$ and get $2L$ eigenvalues and eigenvectors. But this method doesn't take advantage of the particle-hole symmetry of the Hamiltonian kernel. That is, if $\begin{pmatrix} x \\ y \end{pmatrix}$ is an eigenvector with eigenvalue ϵ, then $\begin{pmatrix} y \\ x \end{pmatrix}$ is also an eigenvector with eigenvalue $-\epsilon$.

For ϵ close to zero, the $\pm\epsilon$ pairs will have great relative error. If the system has multiple zero modes, the mixing error is even more complicated. Unfortunately, these zero Majorana modes are just our interest points. We need an new eigenvalue solver, taking advantage of the particle-hole symmetry. Then I asked a question on math.stackexchange.com [36]. The solution is to use the singular value decomposition of M (SVD).

$$M = \phi \Lambda \psi^T \tag{1.38}$$

The columns of ϕ and ψ gives the coefficients in Majorana representation Equation (1.32)

$$\tilde{b}_n = \sum_i \phi_{in} b_i \qquad \tilde{a}_n = \sum_i \psi_{in} a_i \qquad \epsilon_n = \Lambda_{nn}$$

1.8 A numerical method to calculate Pfaffian

I'm using a very simple and effective method of calculating Pfaffian for any $2N \times 2N$ skew-symmetric matrix invented by Xun Jia's in the paper [22]

Let X be an $2N \times 2N$ skew-symmetric matrix, with decomposition :

$$X = \begin{pmatrix} A & B \\ -B^T & C \end{pmatrix}. \tag{1.39}$$

. Then

$$\begin{pmatrix} I_2 & 0 \\ B^T A^{-1} & I_{2N-2} \end{pmatrix} X \begin{pmatrix} I_2 & -A^{-1}B \\ 0 & I_{2N-2} \end{pmatrix} = \begin{pmatrix} A & 0 \\ 0 & C + B^T A^{-1} B \end{pmatrix} \tag{1.40}$$

We have:

$$\det(X) = \det(A)\det(C + B^T A^{-1}B) \tag{1.41}$$

Equation (1.41) gives us a iteration method. Each iteration, we find an $A = \begin{pmatrix} 0 & a_{12} \\ -a_{12} & 0 \end{pmatrix}$ from the X, such that $|a_{12}|$ is the largest(for stability purpose). Then recall that $\mathrm{pf} \sim \sqrt{\det}$ up to an undetermined sign, but the sign of $\mathrm{pf}(A) = a_{12}$ is clear, so we have:

$$\mathrm{pf}(X) = a_{12}\,\mathrm{pf}(C + B^T A^{-1}B) \tag{1.42}$$

Before next iteration step, set:$X' \to C + B^T A^{-1}B$, then do it again and again, we expect to see the final result looks like:

$$\mathrm{pf} = a_{12}a'_{12}a''_{12}a'''_{12}a''''_{12}\cdots$$

Notice that, the matrix A doesn't have to be in the position shown in Equation (1.41), but we can always trivially exchange the columns $1 \leftrightarrow i$ and rows $2 \leftrightarrow j$, making $A = \begin{pmatrix} 0 & a_{ij} \\ -a_{ij} & 0 \end{pmatrix}$ to be $A = \begin{pmatrix} 0 & a_{12} \\ -a_{12} & 0 \end{pmatrix}$.

FIG. 1.23 is a benchmark test of three different algorithm for Pfaffian calculation. The other two algorithms are by M. Wimmer [58]. During the benchmarking, I'm using random complex valued skew-symmetric matrices, with increasing size from 20 to 300. The Pfaffian value given by the three methods are all agree with each others, within machine precision. We can see that, Jia's method ranks the 2nd fast. Not the fastest, but I should stress that, the implementation algorithm is far more simpler that Wimmer's method.
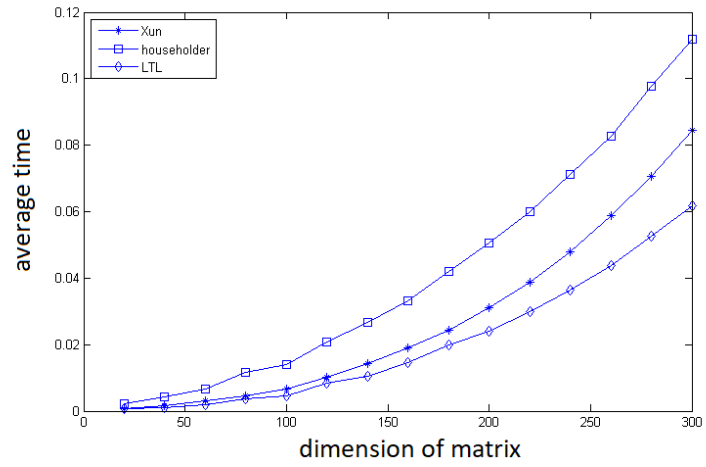
Figure 1.23:   Benchmark test of Pfaffian, horizontal axis is the size of matrix, vertical axis is the average computing time in seconds

CHAPTER 2

Numerical analytic continuation by rational function regression

2.1 Introduction

One of the bottlenecks of quantum Monte Carlo study is how to perform a reliable analytic continuation from imaginary time to real time. Two major families are the Padé method [50, 4, 19, 33, 44, **?**] and the kernel based maximum entropy method [21, 45, 15, 26, 61, 2, 14, 34, 17, 41, 3, 42, 48]. They both have their pros and cons [18, 43]. The Padé method needs very accurate imaginary time input data. The maximum entropy method requires *a priori* information.

In this work, we are going to use the Padé method by casting it to a standard rational function regression problem. In order to estimate the error, bootstrapping statistics is used to generate an ensemble of imaginary input data. Compared with the traditional kernel based method, the rational function representation is more natural, because the zeros and poles will capture all the information, if the physical system is made of finite elements of RLC (resistor-inductor-capacitor) components.

2.2 The statement of the problem

2.2.1 Notations

The spectral function $\rho(\omega)$ is a $\mathbb{R} \to \mathbb{R}_{\geqslant 0}$ function. The analytic Green function $G(z)$ is a $\mathbb{C} \to \mathbb{C}$ function. They are related by:

$$G(z) = \int_{-\infty}^{+\infty} \rho(\omega) \frac{1}{\omega - z} d\omega \tag{2.1}$$

The analytic Green function, is compact and elegant, because the Matsubara Green function and the retarded Green function can be represented as imaginary and real part of the analytic Green function:

$$G^M(\omega_n) = G(i\omega_n) \tag{2.2}$$

$$G^R(\omega) = G(\omega + i0^+) \tag{2.3}$$

The spectral function

$$\rho(\omega) = -\frac{1}{\pi} \text{Im}[G^R(\omega)] \tag{2.4}$$

contains all the information of the dynamics. And it is easy to get the entire $G(z)$ from $\rho(\omega)$ by integrating Eq. 2.1 directly. However, it is hard to recover $\rho(\omega)$ from the information of $G^M(\omega_n)$ via:

$$G^M(\omega_n) = \int_{-\infty}^{+\infty} \rho(\omega') \frac{1}{\omega' - i\omega_n} d\omega' \tag{2.5}$$

This is an inverse problem. G^M comes from Monte Carlo simulation, with error, and ω_n's are discrete and finite.

2.2.2 Statement

Input: estimated Matsubara frequency Green function with the error $G^M(\omega_n) \pm \delta G^M(\omega_n)$ for $\omega_n \in \{\Omega, 2\Omega, \cdots, N\Omega\}$, where $\Omega = \frac{2\pi}{\beta}$ [1]

---

[1] We are using Boson Matsubara frequencies throughout this paper. However, identical considerations apply for Fermionic Matsubara frequencies. Also, in a better treatment, the error of Matsubara Green function would be an $N \times N$ co-variant matrix. But here we treat $G^M(\omega_n)$ as independent random variables.

Output: the estimated spectral function and its uncertainty $\rho(\omega) \pm \delta\rho(\omega)$

2.2.3 Test

A good method to test is as follows:

Generation: choose a test function $\rho_{\text{True}}(\omega)$

Encryption: use Eq. 2.1 and 2.2 to generate $G_{\text{True}}^{M}(\omega_n)$, then add random noise $\delta G^{M}(\omega_n)$ to get $G^{M}(\omega_n)$

Recovery: using $\delta G^{M}(\omega_n)$ and $G^{M}(\omega_n)$ in the last step as input, use the Padé Regression method to get the output $\rho(\omega) \pm \delta\rho(\omega)$

Comparison: compare the recovered $\rho(\omega)$ and the original $\rho_{\text{True}}(\omega)$

2.3 The method

2.3.1 Polynomial Fitting and regression

As a warm up, let's first take a look at the Taylor approximation of real-to-real mapping functions: Given N points $(x_i, y_i = f(x_i))$, our motivation is to find out a polynomial

$$p_M(x) = a_0 + a_1 x + a_2 x^2 + ...a_M x^M \tag{2.6}$$

which can be used to fit the unknown function form $y = f(x)$. There are three situations of the polynomial degree:

- $M + 1 < N$ over-determined fitting

- $M + 1 = N$ unique fitting
  (number of parameters $\{a_i\}$ = number of equations $\{y_i = f(x_i)\}$)

- $M + 1 > N$ under-determined fitting

To determine the coefficient a_i, we can solve a linear equation with **vandermonde ma-**

trix.

$$\mathbf{X}A = Y \quad \text{(defined as below)}$$

$$
\begin{pmatrix}
x_1^0 & x_1^1 & x_1^2 & \cdots & x_1^M \\
x_2^0 & x_2^1 & x_2^2 & \cdots & x_2^M \\
\vdots & & & & \\
\vdots & & & & \\
x_N^0 & x_N^1 & x_N^2 & \cdots & x_N^M
\end{pmatrix}
\begin{pmatrix}
a_0 \\
a_1 \\
a_2 \\
\vdots \\
a_M
\end{pmatrix}
=
\begin{pmatrix}
y_1 \\
y_2 \\
y_3 \\
\vdots \\
y_N
\end{pmatrix}
\tag{2.7}
$$

$$A = \mathbf{X}^{-1}Y$$

It has to be stress that: (1) The vandermonde matrix is problematic matrix, with larege condition number, numerically unstable to inverse. So, the expediency solution is to make the matrix dimensional smaller, within the computer's precision. (2) In the cases, other than unique fitting, $\mathbf{X}$ is not a square matrix anymore, we can generalized the definition of $A = \mathbf{X}^{-1}Y$ such that $||\mathbf{X}A - Y||$ is minimized, which is the least square fitting.

2.3.2 Rational function method

The Padé method assumes that the analytic Green function $G(z)$ takes the form of a rational function

$$Q_{L,M}(z) = \frac{p_L(z)}{p_M(z)} = \frac{a_0 + a_1 z + a_2 z^2 + \ldots a_L z^L}{b_0 + b_1 z + b_2 z^2 + \ldots b_M z^M} \tag{2.8}$$

Where L and M are the degrees of the polynomials; as a normalization convention, we shall also choose $b_0 = 1$. The idea is to use $(L+M+1)$ complex parameters $\{a_0, a_1, \cdots, a_L, b_1, \cdots, b_M\}$ to represent an arbitrary $G(z)$. Instead of using the value of $\rho(\omega)$ on discrete ω to represent $G(z)$, as in the maximum entropy method. An alternative form of Eq. 2.8 can be more physicially meaninguful, it is given by:

$$Q_{L,M}(z) = \frac{p_L(z)}{p_M(z)} = \frac{a_0(z - A_1)\cdots(z - A_L)}{(z - B_1)\cdots(z - B_M)} \tag{2.9}$$

There are L zeros and M poles, and a complex amplitude a_0. As a result of causality, $G(z)$ should be analytic in the upper half plane. In a reasonable regression, all B_i should be in the lower half plane, or B_i should be canceled by A_j in the upper half plane. Also, for physics problems with symmetry, the distribution of zeros and poles should have those symmetries. This reduces the degrees of freedom of the parameters.

2.3.3 The regression problem

As a regression problem, our input data are N Matsubara frequencies $z_n = i\Omega n$, and the values of Green function $u_n = G(z_n)$ at these frequencies. The output are the coefficients a_i and b_i in the rational polynomial of Eq. 2.8. There are N equations, and $L + M + 1$ parameters to be fit. N of those Eq. 2.8 can be written in a linear regression form: Eq. 3.24 and Eq. 2.11 [2]. Where the matrix $\boldsymbol{X}$ and the vector $\boldsymbol{y}$ contain input data, the vector $\boldsymbol{\beta}$ contains the parameters to be calculated.

$$
\left(
\begin{array}{cccc|cccc}
-u_1 z_1^1 & -u_1 z_1^2 & \cdots & & z_1^0 & z_1^1 & z_1^2 & \cdots \\
-u_2 z_2^1 & -u_2 z_2^2 & \cdots & & z_2^0 & z_2^1 & z_2^2 & \cdots \\
\vdots & \vdots & \vdots & & \vdots & \vdots & \vdots & \vdots \\
\vdots & \vdots & \vdots & & \vdots & \vdots & \vdots & \vdots \\
\vdots & \vdots & \vdots & & \vdots & \vdots & \vdots & \vdots \\
\vdots & \vdots & \vdots & & \vdots & \vdots & \vdots & \vdots \\
\vdots & \vdots & \vdots & & \vdots & \vdots & \vdots & \vdots \\
-u_N z_N^1 & -u_N z_N^2 & \cdots & & z_N^0 & z_N^1 & z_N^2 & \cdots
\end{array}
\right)
\left(
\begin{array}{c}
b_1 \\ b_2 \\ \vdots \\ \vdots \\ \hline a_0 \\ a_1 \\ a_2 \\ \vdots
\end{array}
\right)
=
\left(
\begin{array}{c}
u_1 \\ u_2 \\ \vdots \\ \vdots \\ \vdots \\ \vdots \\ u_{N-1} \\ u_N
\end{array}
\right)
\tag{2.10}
$$

$$
\boldsymbol{X}_{N\times(L+M+1)}\boldsymbol{\beta}_{(L+M+1)\times 1} = \boldsymbol{y}_{N\times 1}
\tag{2.11}
$$

Eq. 2.11 is the compact form of Eq. 3.24

---

[2] the equal sign "=" in Equation 3.24 and 2.11 should be understood in a linear regression manner: find $\boldsymbol{\beta}$, such that $||\boldsymbol{X}\boldsymbol{\beta} - \boldsymbol{y}||^2$ is minimized

Sub-index n in z_n and u_n labels one Matsubara frequency point, and they are all at the n-th row of $\boldsymbol{X}$. $\left[n^{\text{th}} \text{ row of } \boldsymbol{X}\right]\boldsymbol{\beta} = u_n$ has the same meaning of Eq. 2.8

2.3.4 Choice of L and M

In (2.11), we can normalizes and set $b_0 = 1$, then parameters degrees of freedom is $2L+2M+2$, and the N complex points give us $2N$ equations, therefore:

- $L + M + 1 < N$ over-determined fitting

- $L + M + 1 = N$ unique fitting

- $L + M + 1 > N$ under-determined fitting

In the unique fitting case, people's experience is, $\frac{N}{2} \approx M \leqslant L \approx \frac{N}{2}$ gives the best fitting performance. The degree of nominator is no less than the degree of denominator. To be more precise, the so called diagonal Pade polynomial:

- if $N = 2n$, then $L = n$, $M = n - 1$

- if $N = 2n + 1$, then $L = M = n$

As a rule of thumb, in this paper we take:

$$L \approx M \approx N/2$$

The argument is as follows: For too large M and L, the model might be over-fitting. In the case of $L + M + 1 = N$, the number of equations is the same as the numbers of fitting parameters. For small L, and M, we are afraid that, there will not be enough poles and zeros to represent $G(z)$. $L \approx M$ tends to cancel zeros and poles, and the real $G(z)$ only contain a few poles. In a fully developed Bayesian method, both $\boldsymbol{\beta}$ and L, M are taken as estimation random variables. But for simplicity, we are going to choose the most representative $N/2$ value as L and M

43

2.3.5 Bootstrapping statistics

In the Padé method [50], single $\boldsymbol{X}$ and $\boldsymbol{y}$ are used to generate a single $\boldsymbol{\beta}$ without error estimation. Here, we treat $\boldsymbol{X}$ and $\boldsymbol{y}$ as the mean value of a distribution with standard errors $\delta\boldsymbol{X}$ and $\delta\boldsymbol{y}$. These errors come from Monte Carlo result: u_i and δu_i.

The idea of bootstrapping statistics is to generate *an ensemble* of input data: $\{\boldsymbol{X}\}$ and $\{\boldsymbol{y}\}$. Then perform the regression individually to get an ensemble of $\{\boldsymbol{\beta}\}$, and then get a collection of spectrum $\{\rho(\omega)\}$. From the ensemble of spectrum, we take the best estimation and its uncertainty as mean$\{\rho(\omega)\}$ and std$\{\rho(\omega)\}$ (standard deviation). Compared to the traditional model based regression and error estimation, bootstrapping is simple and natural — various slightly different inputs are thrown into this black-box, then we check the difference among those output spectra. If those outputs are close to each other, it indicates the spectrum recovery is reliable.

Now, we need to generate those resamplings, $\{\boldsymbol{X}\}$ and $\{\boldsymbol{y}\}$. It is done by replacing the best values u_i in Equation (3.24) by a distribution of themselves. Our assumption is that the Monte Carlo estimation of Green function value u_i has a normal distribution $\mathcal{N}(u_i, \delta u_i)$. This is a result of the central limit theorem. In this paper, we take the relative error $\frac{\delta u_i}{u_i} \leq 1\%$. The assumption is even better satisfied for smaller relative errors. The procedure is summarized as follows:

- Generate an ensemble of resampling $\{\boldsymbol{X}\}, \{\boldsymbol{y}\}$. This is done by replacing the best value u_i in Equation (3.24), with its distribution $u_i \rightarrow \mathcal{N}(u_i, \delta u_i) = \mathcal{N}(\hat{G}^M(\omega_n), \delta_{G^M}(\omega_n))$

- Perform least square linear regression for individual input data pair $\boldsymbol{\beta} = \boldsymbol{X}^{-1}\boldsymbol{y}$ so that we have an ensemble $\{\boldsymbol{\beta}\}$

- Use $\{\boldsymbol{\beta}\}$ to generate $\{\rho(\omega)\}$ and then calculate mean$\{\rho(\omega)\}$ and std$\{\rho(\omega)\}$

The number of resamplings is defined as $\mathfrak{N}$. It should be large enough, so that mean$\{\rho(\omega)\}$ and std$\{\rho(\omega)\}$ (std stands for standard deviation) converge. Our answer is therefore given

by

$$\rho(\omega) \pm \delta\rho(\omega) \approx \text{mean}\{\rho(\omega)\} \pm \text{std}\{\rho(\omega)\} \tag{2.12}$$

Notice that the estimated error $\delta\rho(\omega)$ *is not* $\frac{\text{std}\{\rho(\omega)\}}{\sqrt{\mathfrak{N}}}$. $\delta\rho(\omega)$ is the variation of the output spectrum, subject to slightly different input data. It represents the robustness of such "input-blackbox-output" system (Fig. 2.1), therefore should be $\text{std}\{\rho(\omega)\}$. Eq. 2.12 is asymptotically reliable as the relative error $\delta\rho/\rho$ becomes smaller and smaller. If this relative output error is larger than order 1 (for example $\frac{1}{3}$), we need to continue Monte Carlo simulation for a higher precision $u \pm \delta u$, and then use it as the input data of the blackbox.

Such bootstrapping doesn't take too much time to run, the major time cost still comes from Monte Carlo. In a problem with $N = 35$ Matsubara frequency points, taking $\mathfrak{N} = 20000$ resamplings for good convergence, it only costs one minute in a laptop. The overall time complexity is $O(\mathfrak{N}N^3)$, as it performs $O(N^3)$ linear regression $\boldsymbol{\beta} = \boldsymbol{X}^{-1}\boldsymbol{y}$ for $\mathfrak{N}$ times. The choice of discrete lattice ω only affects the plotting.
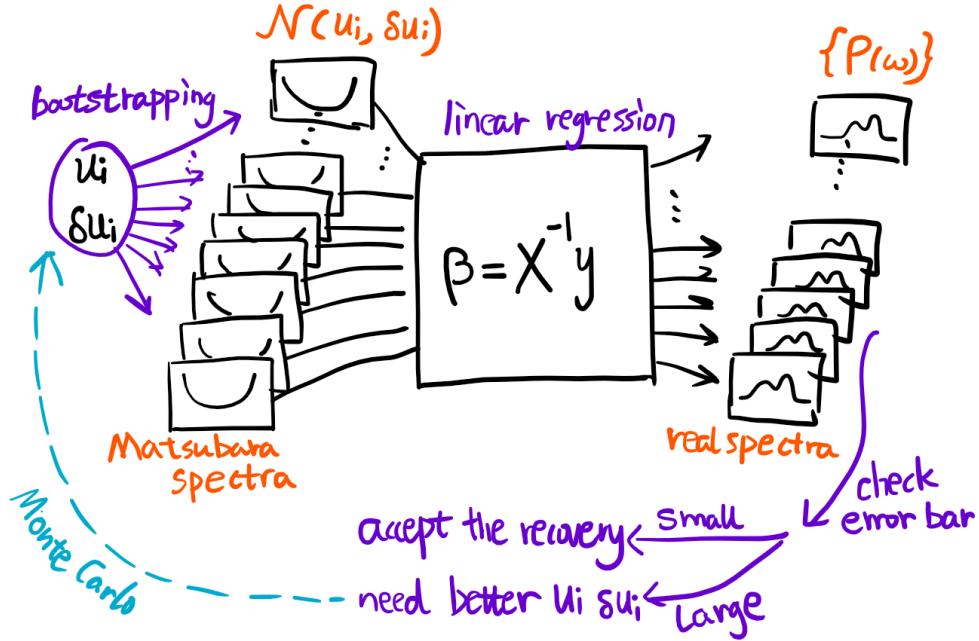
Figure 2.1: A schematic of the method. (1) The Monte Carlo data u_i and δu_i is used to generate an ensemble of Matsubara spectra. (2) Perform linear regression individually. (3) Get an ensemble of real spectra. Check the relative error of those spectra, if too large, then we need longer time Monte Carlo calculation for a smaller $\delta u_i/u_i$.

2.4 Test cases

Two factors can change the testing results, which we should be aware of. The first factor is the number of Matusbara frequency data points N and the interval $\Omega = \frac{1}{\beta}$. They should be chosen such that the most of the spectral weight is within the range $[-N\Omega, N\Omega]$, or say $\int_{+N\Omega}^{-N\Omega} \rho(\omega)d\omega \approx 1$(normalized $\rho(\omega)$). The second factor is the relative error of input data $\eta = \delta u/u$. We take $\eta = 10^{-15}, 10^{-6}, 10^{-4}, 10^{-3}, 10^{-2}$, representing the error of most diagrammatic expansion or Monte Carlo simulation. In this section, we are going to use a piece-wise linear function (Fig 2.2) as the test spectrum; more test cases are given in the appendix.

2.4.1 Input data with small error

In Fig. 2.2, the orange curve is the exact test spectral function. The blue curve is a Padé recovery from blurred imaginary Green function with machine precision percentage error (10^{-15}).
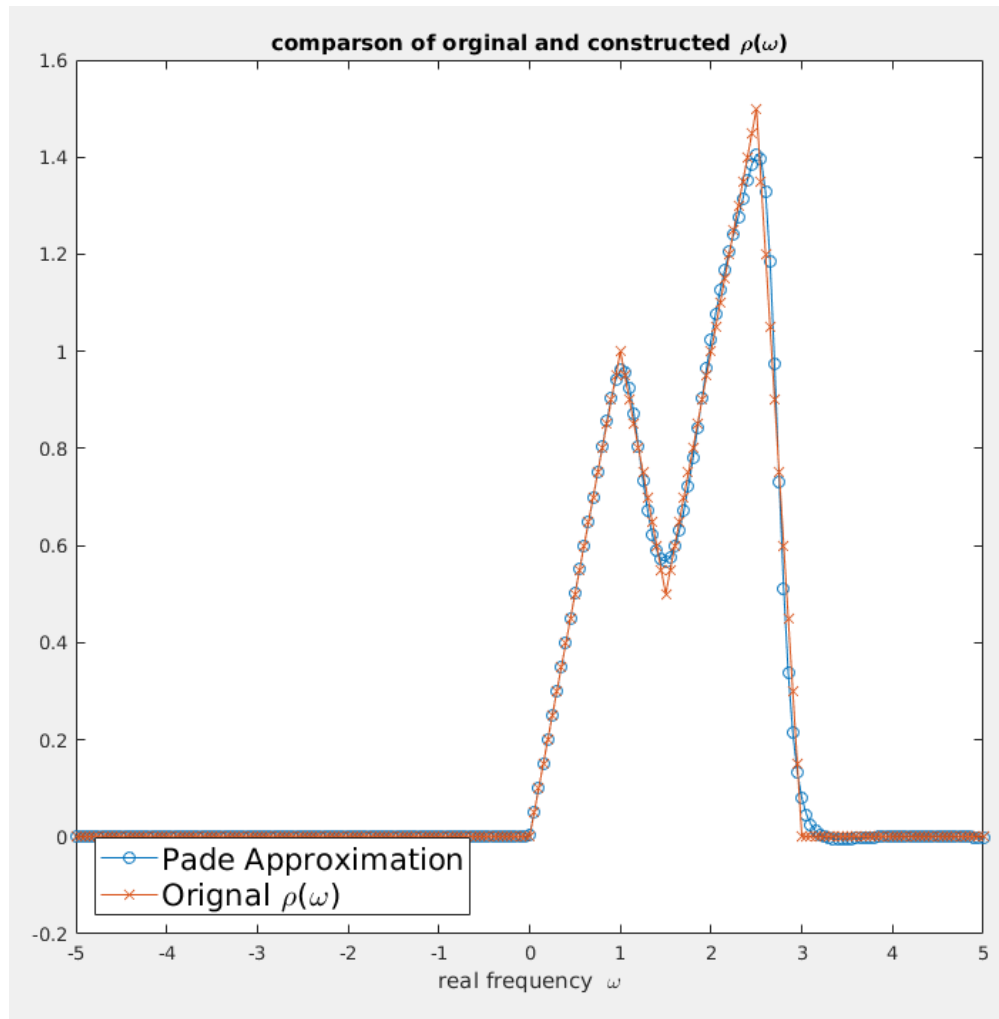
Figure 2.2: Padé approximation spectrum recovery, number of input Matsubara frequency points $N = 35$; error of input Matsubara frequency Green function $\eta = 10^{-15}$. The orange curve is the piece-wise linear test function, the blue curve is the recovered spectrum. They agree very well, except for a few sharp tuning points

In Fig. 2.3, a lot of poles and zeros are paired together; it probably means that $N = 35$

parameters correspond to over-fitting. But this pairing-canceling mechanism makes the result robust, even for over-fitting parameters. This is also the reason why, we approximately chose $L \approx M \approx N/2$ in section 2.3.4. Also, as a result of causality, the upper half plane should have no poles. We see that all the poles are cancelled by zeros in the upper half plane. The locations of zeros and poles, and the coefficient a_0 in Eq. 2.9 carry all the information. Actually, it is the zeros and poles, which are closest to the real axis that will mostly influence the shape of the spectral function. In other other words, if some zeros or poles are far away from the origin, it will have very little influence in the result. This is the second reason for the robustness.
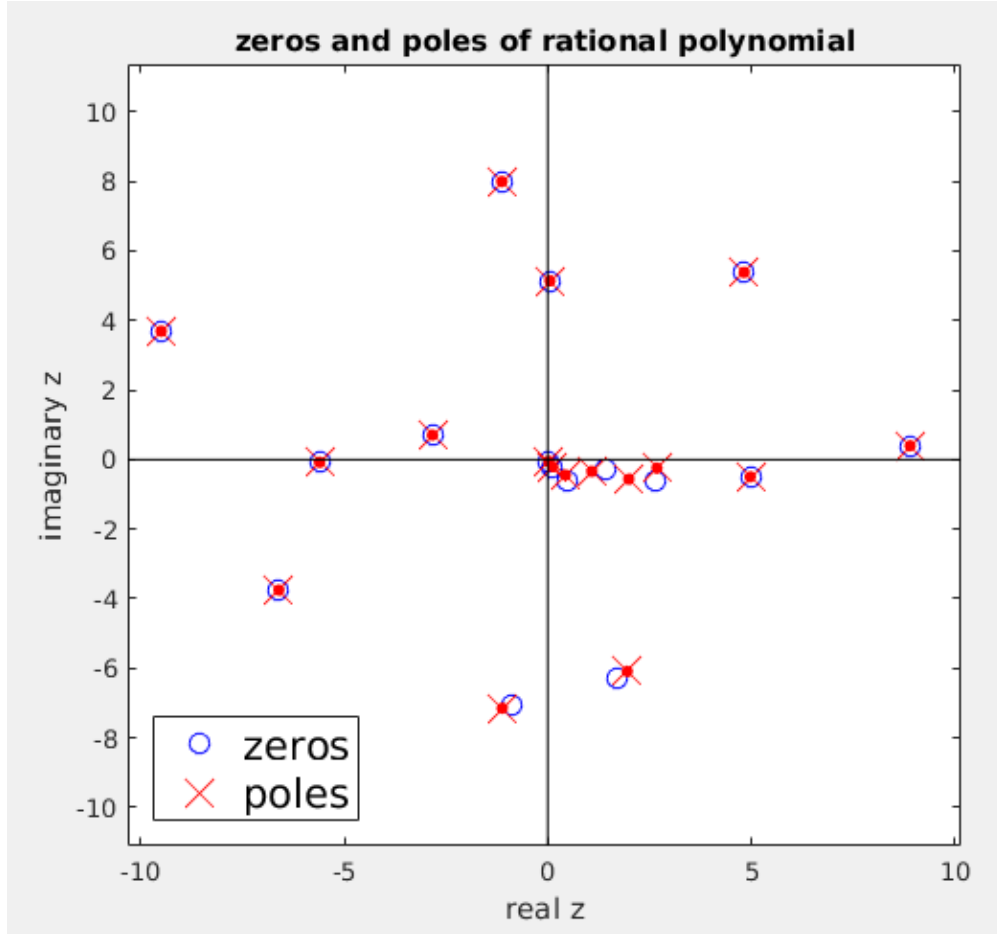
Figure 2.3: Distribution of zeros and poles. Input fitting points $N = 35$, degree of nominator polynomial $L = 17$, degree of denominator polynomial $M = 17$. There are exactly 17 poles on the complex plane. In the upper half plane, the zeros cancels the poles (removable singularity), thus making it analytic (causality). The poles close to the real axis has a huge influence on the shape of the approximation spectrum $\rho(\omega)$: they are the most important part of Padé approximation.

2.4.2 Input data with large error

Here we consider $\eta = 10^{-6}, 10^{-4}, 10^{-3}, 10^{-2}$ are large error compared with $\eta = 10^{-15}$. The computational time scales as [CPU Time] $\propto 1/\sigma^2 = (\frac{u}{\delta u})^2$. Clearly, we cannot have machine precision Monte Carlo data for really large systems. Below is a test with large error in

the input Matsubara frequency data. Fig. 2.4 is an ensemble of recovered real frequency spectrum using bootstrapping statistics. The relative error of input Matsubara frequency data is 0.0001%. Fig 2.5 is the averaged value and error bars.
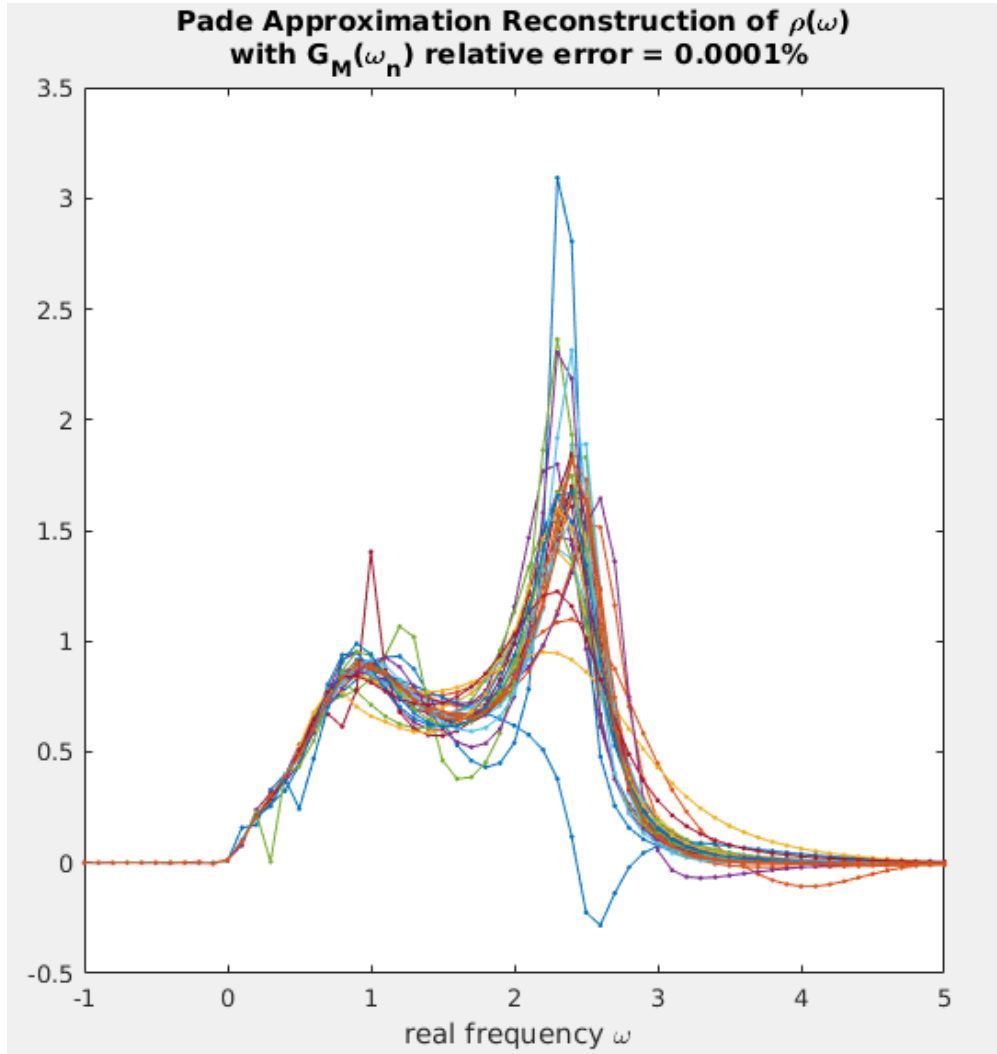
Figure 2.4: The $\{\rho(\omega)\}$ ensemble. Each $\rho(\omega)$ curve is one recovery using Padé regression, there are 30 of them in the plot. The input data's relative error is $\eta = 0.0001\%$ (6 significant digits).
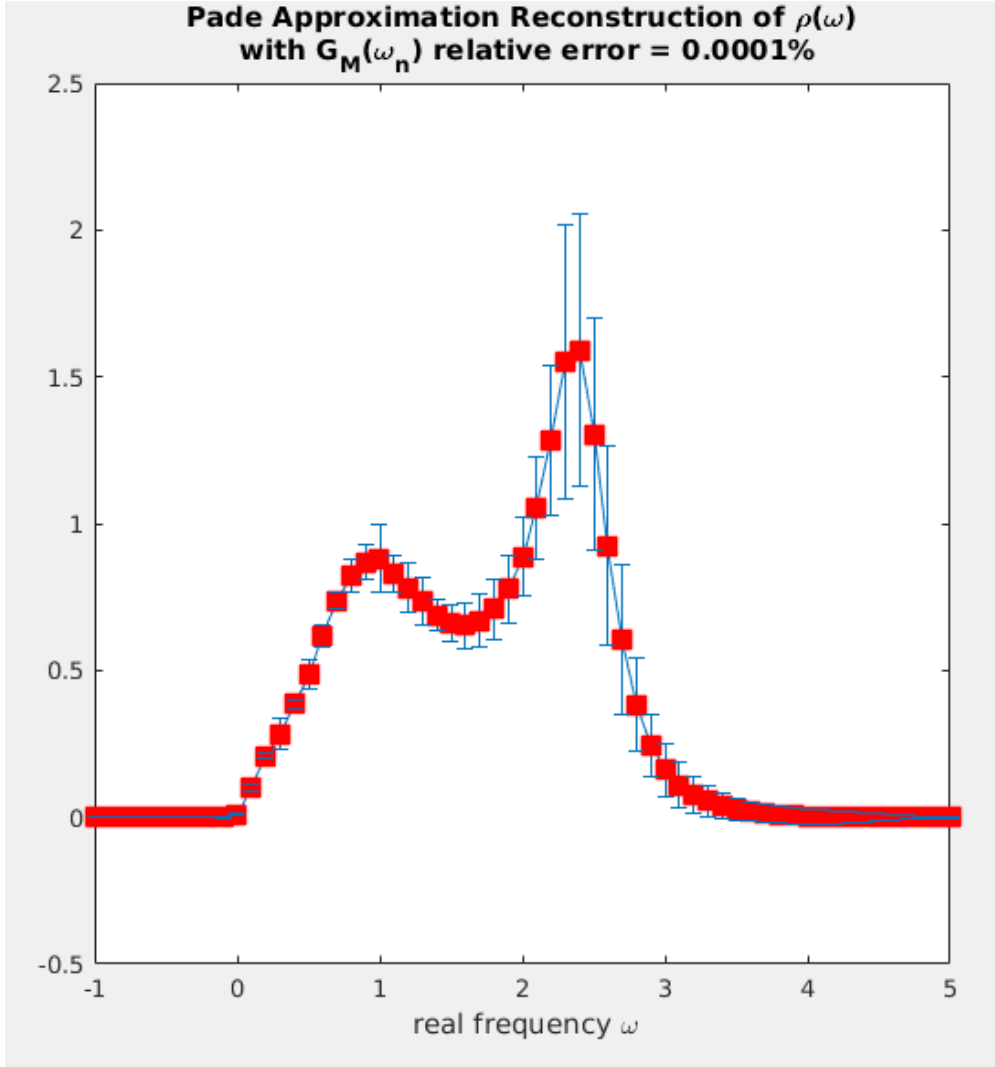
Figure 2.5: 6 significant digits input recovery. Red dots are the mean$\{\rho(\omega)\}$, the blue error bars are std$\{\rho(\omega)\}$. The relative error of the output spectrum is less than $\frac{1}{3}$, detailed shape is reliable.

Figures 2.6, 2.7, and 2.8 give the results of relative error $0.01\%, 0.1\%, 1\%$ respectively. We can see that, the 0.01% result still gives the accurate locations of double peaks $\omega = 1, 2.5$, and the valley at $\omega = 1.5$, and linear shape of the curves. Even for the 1% error data, our method generates a very reasonably recovered spectrum, it locates the spectrum's location $0 < \omega < 3$ and gives the correct peak height around 1 to 1.5. Notice that, for such test spectrum, double peak triangles, is a difficult function to recover. In the appendix, a family

of physically sensible spectrum are tested.
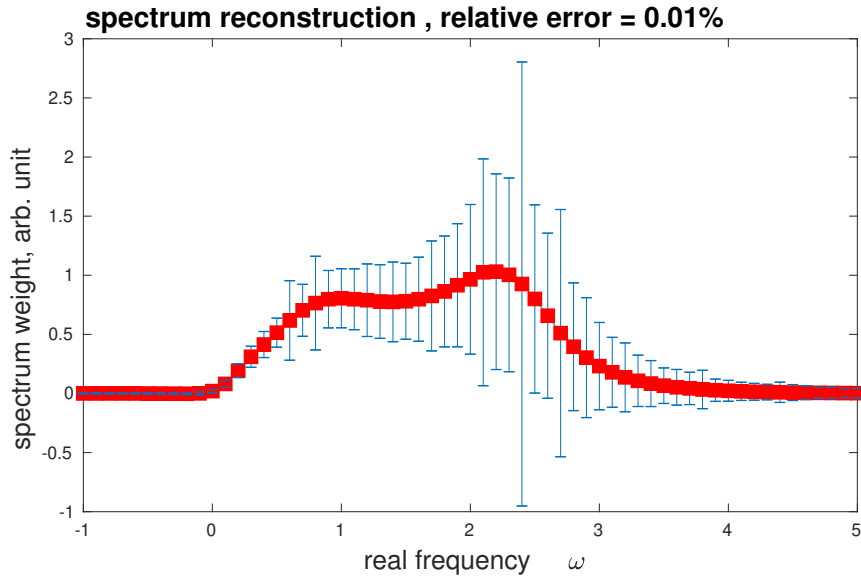
Figure 2.6: 4 significant digits input recovery. Red dots are the mean$\{\rho(\omega)\}$, the blue error bars are std$\{\rho(\omega)\}$. The relative error is of order one, the detailed shape is not reliable.
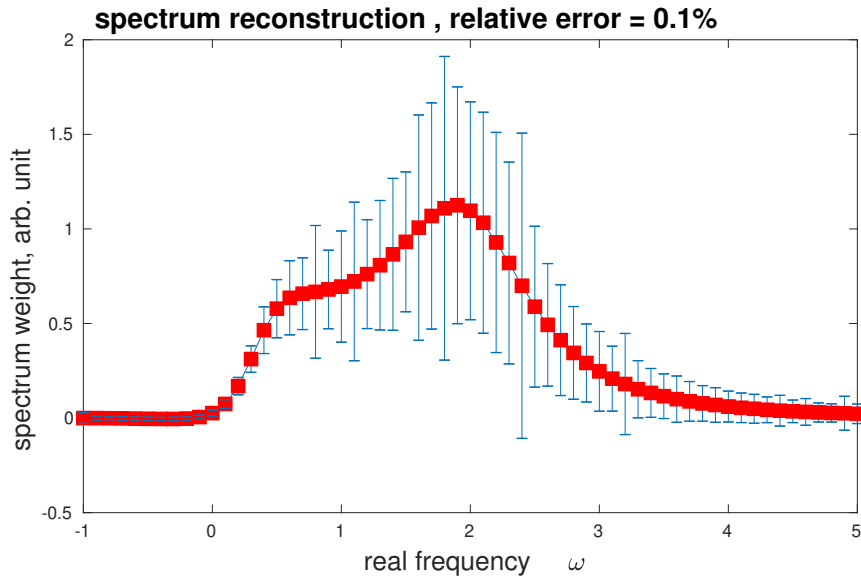
Figure 2.7: 3 significant digits input recovery. Red dots are the mean$\{\rho(\omega)\}$, the blue error bars are std$\{\rho(\omega)\}$. The relative error is of order one, the detailed shape is not reliable.

In order to check that $\eta = 1\%$ recovery is not an accident, we shift the double triangle

spectrum reconstruction , relative error = 1%
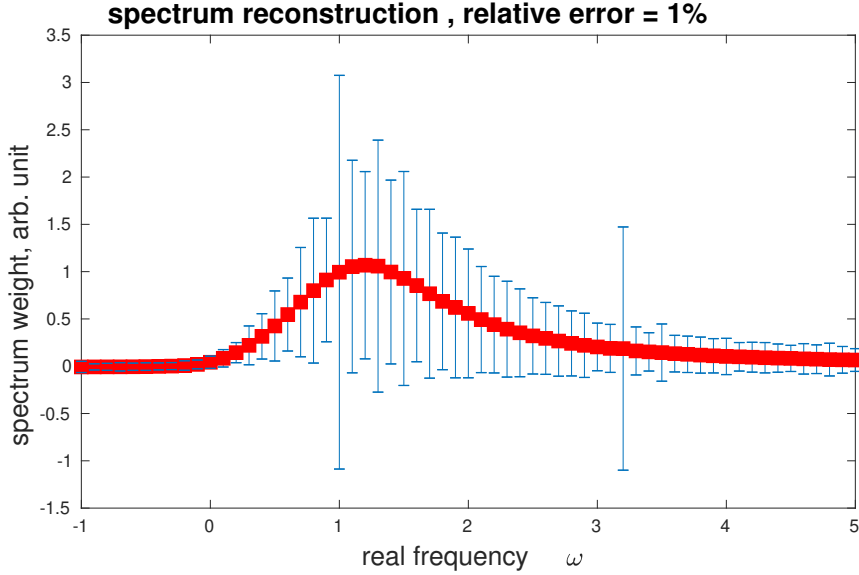
Figure 2.8: 2 significant digits input recovery. Red dots are the mean$\{\rho(\omega)\}$, the blue error bars are std$\{\rho(\omega)\}$. The relative error is at order one, the detailed shape is not reliable.

spectrum horizontally by -4,-2,0,2 to get four difference test functions (Fig. 2.9), we can see that the recovered spectrum all falls in the correct range. And the performance is surprisingly well for the lower frequency blue curve, because its spectral weight is closer to the imaginary axis.

However, if we want to recover the *detailed shape* of an unknown spectrum, we should really check the error bar std$\{\rho(\omega)\}$. When the error bar is large (same order as the value), the detailed shape is not reliable, which is the case of Fig. 2.6 2.7 2.8. In the case of Fig. 2.5, the error bar is no larger than $\frac{1}{3}$ of the best value, we are then sure that the detailed shape is reliable.

2.5 Conclusion

In this chapter we use rational function to represent the physical system. A matrix form is constructed, to convert it to a standard linear regression problem. Bootstrapping statistics is applied, to get best estimation and estimated errors. For high precision recovery, the
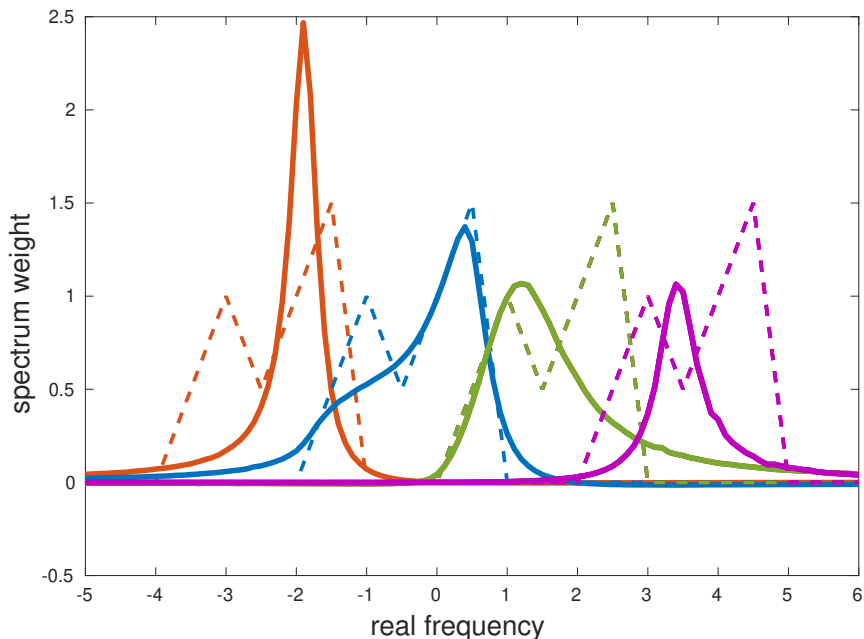
Figure 2.9: Spectrum recovery for 1% relative error input data. Solid curves are the recovered spectrum; dashed curves are the original test function, they are shifted by 2 for comparison. There are 4 pairs, same color is the pair. We can see that, the position of spectrum falls in the correct range of each original test function, the magnitude is also at the same order of the test function. The blue curve agrees reasonably well. This method performs better for low frequencies, because low frequency points are closer to imaginary axis' input data.

error gives information about whether or not we need to increase the Monte Carlo data's accuracy. For low precision recovery, our method still gives correct position and amplitude of the spectrum even for 1% relative error input data. This regression form can be used for further study, either combined with maximum entropy, or machine learning methods [61, 2, 14]. Future work can also be done utilizing the symmetry aspect of zeros and poles and the fully Bayesian choices of L and M.

2.6 Recovery test for more functions

Below, a few other functions are given as examples. The dashed green thick line is the exact spectral function. The other 4 solid lines are Padé regression recovered results for different relative errors, ranging from 1% to 0.001% First of all, we see that, this method all gives the correct location of spectral weight, even for 1% error. Secondly, Lorentzian curves are exactly recovered, (single peak 0.1 %, double peak 0.001%), because they are rational functions. For the Gaussian curve, we cannot recover the detail shape, but the location of the peak is still accurate. For the semicircle and square, the exact shapes are not recovered, but the starting and the ending frequencies agree reasonably well. As the error gets smaller, the more peaks is added to approach the exact result.
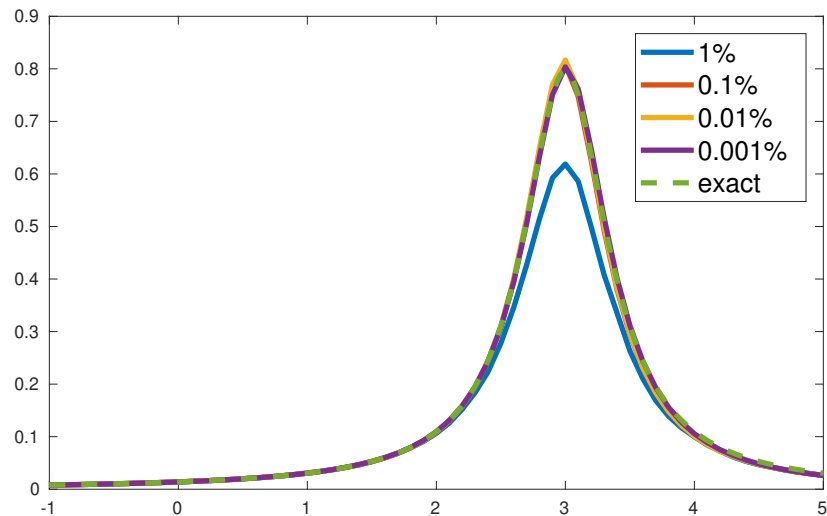
Figure 2.10: Dashed line is the Lorentzian distribution test spectrum. Colored solid lines are recovered spectra with different input errors.
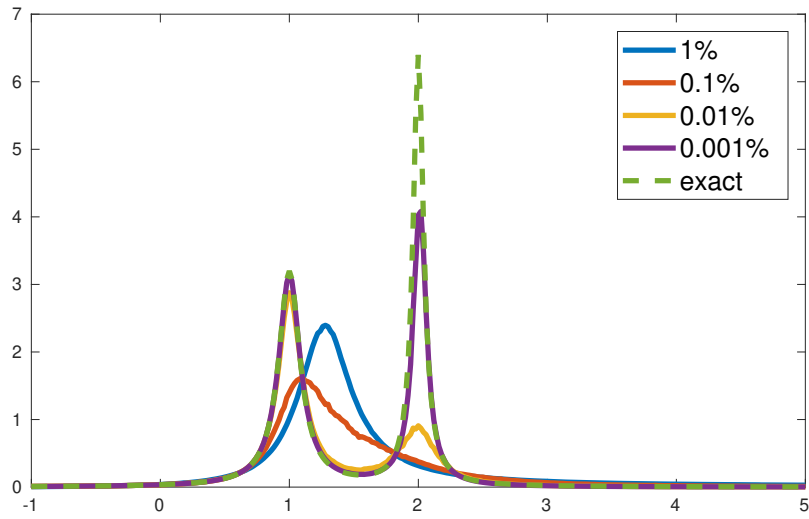
Figure 2.11: Dashed line is the double Lorentzian distribution test spectrum. Colored solid lines are recovered spectra with different input errors.
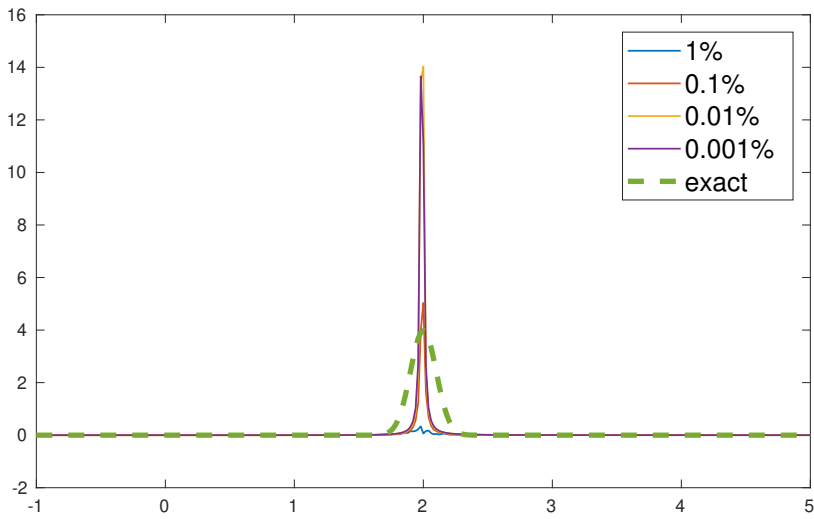
Figure 2.12: Dashed line is the Gaussian distribution test spectrum. Colored solid lines are recovered spectra with different input errors. As the input accuracy is increasing, neither mean$\{\rho(\omega)\}$ nor std$\{\rho(\omega)\}$ converge. Gaussian analytic function is a very special case.
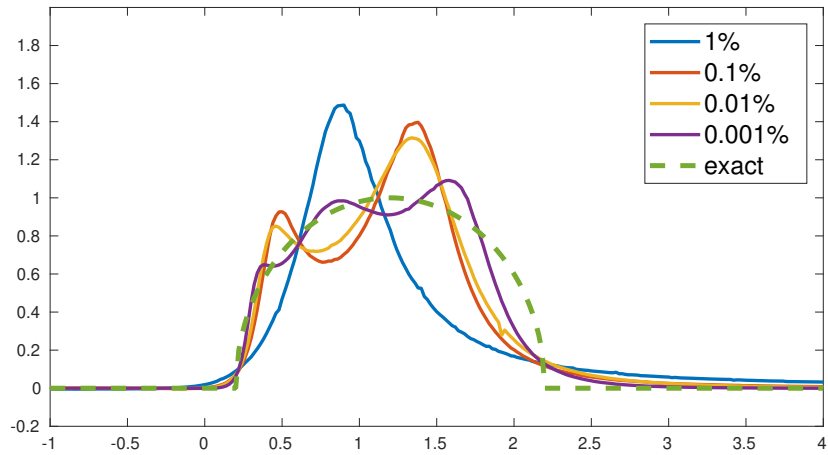
Figure 2.13: Dashed line is the semicircle distribution test spectrum. Colored solid lines are recovered spectra with different input errors.
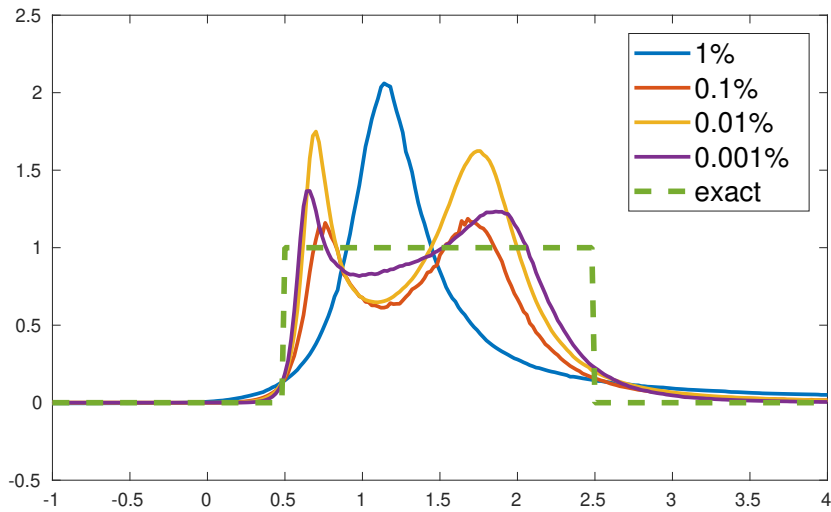
Figure 2.14: Dashed line is the square distribution test spectrum. Colored solid lines are recovered spectra with different input errors.

2.6.1 Other possible methods

2.6.1.1 Maximum Entropy Method

Give an input vector $\mathbf{b}$ and a kernel matrix $\mathbf{A}$ (very large conditional number.), our aim is to recover the vector $\mathbf{x}$, from the relation:

$$\mathbf{A}_{N \times M} \mathbf{x}_{M \times 1} = \mathbf{b}_{N \times 1}$$

This is called **the inverse problem**. The difficulty lies in $\mathbf{A}^{-1}$ is often ill defined, problematic to calculate. The formal solution $\mathbf{x} = \mathbf{A}^{-1}\mathbf{b}$ is not going to work. Therefore, people use optimization point of view, the question becomes, to find a nice $\mathbf{x}$ such that, $||\mathbf{A}\mathbf{x} - \mathbf{b}|| = \sum_i |(\sum_j A_{ij} x_j) - b_i|^2$ is minimized. However, the input data $\{b_i\}$ may has error $\{\sigma_i\}$, the smaller error b_i should have greater priority to be fit, therefore we divide that part by σ_i, we target function becomes $\sum_i |\frac{(\sum_j A_{ij} x_j) - b_i}{\sigma_i}|^2$. In practical problems, the vector $\mathbf{x}$ may subject to some constraint, or a default model $\mathbf{D}$ [15]

2.6.1.2 Cauchy-Riemann equation

Rewrite $G(z)$ as real and imaginary parts:

$$G(z) = G(x + iy) = U(x, y) + iV(x, y) \tag{2.13}$$

since $G(z)$ is analytic in the upper half plane, it must satisfy the **Cauchy-Riemann condition**, in that domain:

$$\begin{cases} \partial_x U = \partial_y V \\ \partial_y U = -\partial_x V \end{cases} \tag{2.14}$$

or written in a decoupled form

$$\begin{cases} \Delta U = 0 \\ \Delta V = 0 \\ \nabla U \cdot \nabla V = 0 \end{cases} \tag{2.15}$$

Equation 2.14 or 2.15 and the Matsubara frequency data, can be served as the input of a **PDE initial value problem**, we are trying to solve the values on the real axis boundary. It is possible to use neuron network method to solve PDE.

2.6.2 Properties of analytic Green functions

The spectrum $A(\omega)$ or $\rho(\omega)$ contains all the information of analytic Green function. There are many different definition conventions, up to a coefficient of $\pi, 2\pi, (-1), i$. This is my convention:

$$G(z) = \int_{-\infty}^{+\infty} \frac{A(\omega_0)}{z - \omega_0} d\omega_0 \tag{2.16}$$

$$G_R(\omega) = G(\omega + 0^+) \tag{2.17}$$

$$G_M(\omega_n) = G(i\omega_n) \tag{2.18}$$

$$A(\omega) = -\frac{1}{\pi}\text{Im}[G_R(\omega)] \tag{2.19}$$

To prove 2.19, we need to understand

$$\frac{1}{\omega + i\epsilon - \omega_0} = \frac{(\omega - \omega_0) - i\epsilon}{(\omega - \omega_0)^2 + \epsilon^2} \approx \frac{1}{\omega - \omega_0} - i\frac{\epsilon}{(\omega - \omega_0)^2 + \epsilon^2}$$

Recall the Cauchy-Lorentz distribution $P = (1/\pi)\frac{\gamma}{(x-x_0)^2+\gamma^2}$, when $\gamma \to 0$ the distribution looks like a delta peak $\delta(x - x_0)$, therefore

$$\lim_{\epsilon \to 0^+} \frac{1}{\omega + i\epsilon - \omega_0} = \text{P.V.}\frac{1}{\omega - \omega_0} - i\pi\delta(\omega - \omega_0)$$

The equation above should be understood in the context of integrate kernel. Plug it into 2.16, we have:

$$G_R(\omega) = G(\omega + 0^+) = \left[\text{P.V.} \int_{-\infty}^{+\infty} \frac{A(\omega_0)}{\omega - \omega_0} d\omega_0\right] + i\left[(-\pi)A(\omega)\right]$$

With $\left[\text{Re}\right] + i\left[\text{Im}\right]$ the structure now is very clear, we have proved 2.19 #

Cauchy's integral formula

$$f(z) = \frac{1}{2\pi i} \int \frac{f(\xi)}{\xi - z} d\xi \tag{2.20}$$

Cauchy's differentiation formula

$$f^{(n)}(z) = \frac{n!}{2\pi i} \int \frac{f(\xi)}{(\xi - z)^{n+1}} d\xi \qquad (2.21)$$

CHAPTER 3

Spectra of the dissipative spin chain

3.1 Introduction

Dissipation plays an important rule in quantum phase transitions [7, 25, 8, 55, 23, 35, 49, 54, 31, 60]. There can be localization-delocalization transitions and coherence-decoherence transitions as the dissipative strength is tuned. Dissipative dynamics is also the bottleneck to build a reliable quantum computer. [20] However, exactly solvable dissipative quantum systems are few and far between and often numerical approaches are needed, However, extracting reliable real time dynamics from numerical simulation in the imaginary time simulation is difficult. Ironically, it is the real time results that are mostly relevant to experiments.

In this section, we are going to extend the (0+1) dimensional [12, 51] spin-boson system to (1+1) dimension. It is a transverse Ising chain, with each spin coupled to a Ohmic bosonic heat bath. We use Monte Carlo method [59, 47, 29, 6] to explore the system and generate imaginary time spin-spin correlations [57, 46, 56]. For analytic continuation to the real time, we use our newly developed Padé Regression method [53] to get the real time dynamical spectra.

In the limit of no dissipation, the real frequency spectrum can be exactly solved via Jordan-Wigner transformation [37, 62, 52]. Hence our quantum Monte Carlo and the analytic continuation methodology can be checked to some extent by comparing with the exact results in the case of no dissipation Fig. 3.6. In Sec. II we define the model and describe the Monte Carlo simulation in III. In Sec. IV we discuss the results and the conclusions are discussed in V.

3.2 Single spin in a dissipative bath

Each spin is coupled to a Ohmic heat bath independently.

$$H_{iD} := H_{iI} + H_{iB} = \alpha \sigma_i^z \sum_n \left(b_{in}^\dagger + b_{in}\right) + \sum_n \omega b_{in}^\dagger b_{in} \tag{3.1}$$

H_{iD} is the dissipation Hamiltonian at spin site i. When $\alpha = 0$, the spin σ_i and environment are decoupled, there is no dissipation. The general dissipative spin problem can be written as Eq. (3.2), where the first part Hamiltonian only involves spins, the second part Hamiltonian is a summation over Eq. (3.1) for every spin.

$$H_{no\ dissipation} + \sum_i^\oplus H_{iD} \tag{3.2}$$

Spin-boson problem (0+1 D) is a single spin with dissipation. When α is small, the two level system are non degenerate, the particle are de-localized in double well potential; when α is large, the two levels system gets two degenerate ground states, the particle can be in either of the double wells potential, localized.

$$\Delta \sigma_1^z + H_{1D} \tag{3.3}$$

degenerate ground states $\leftrightarrow$ symmetry broken

A broken symmetry in the classical ensemble means the quantum system has degenerate ground state.
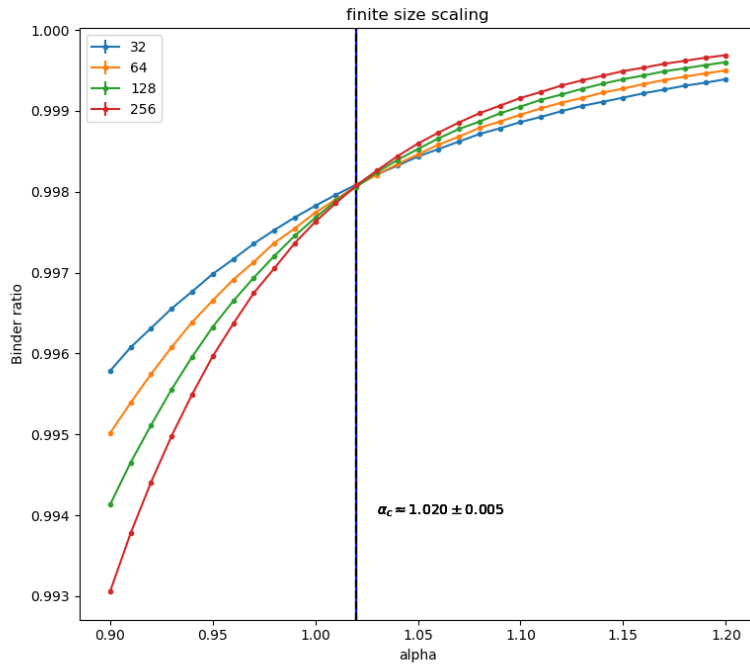
Figure 3.1: Finite size scaling, notice the 1.020 ± 0.005 comes from the periodic long range interaction $\frac{1}{\sin^2(\pi r/L)}$
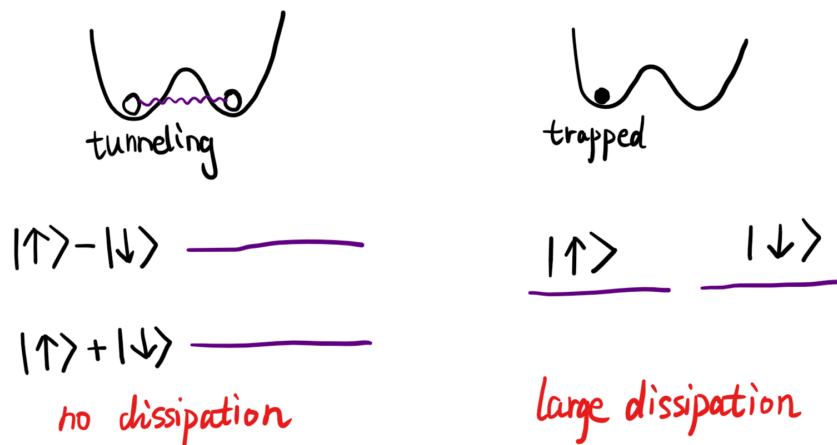
Figure 3.2: A physical picture of the dissipation effect. When the particle has large dissipative interaction with its environment, the particle is trapped locally. The environment "knows" the particle's position

Let's focus on the dynamics of the quantum spin system. The power spectrum is defined as:

$$S(\omega) = \text{Im}[\chi(\omega)]/\omega \tag{3.4}$$

$$\chi(\omega) = \text{Fourier Transform}[\langle \sigma^z(t)\sigma^z(0)\rangle \Theta(t)]$$

We can see, when the dissipation strength is zero. The spectrum is a sharp delta function peak, it's the isolated two level system. As alpha is increasing, the peak center is shifted down, the peak is getting broaden. Finally, the peak is centered at zero frequency. It's because the system get doubly degenerate ground states.
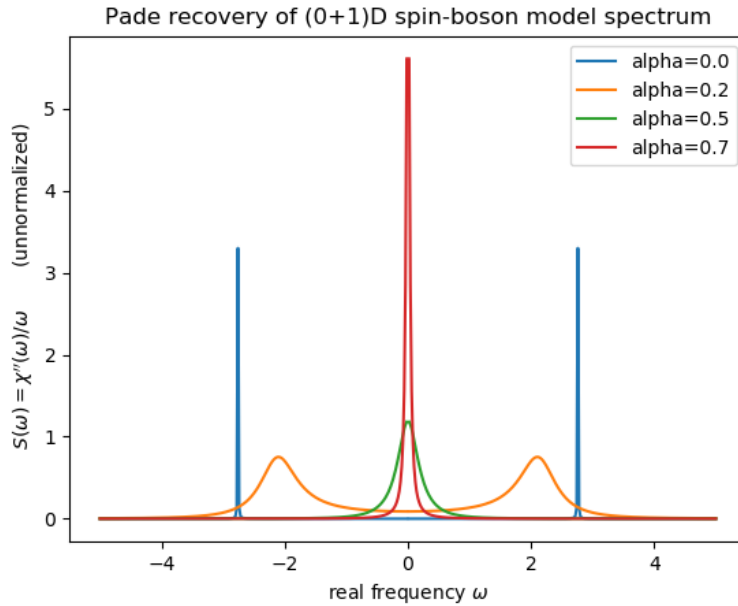
Figure 3.3: Spectrum of (0+1)D spin-boson model for different dissipation strength.

The above calculation is using quantum Monte Carlo simulation and analytic continuation. It can be applied to any $H_{\text{pure spin system}} + H_{\text{dissipation}}$ models. The pro is, this is a universal method. The con is, the Monte Carlo simulation need lots of computer resources. Our goal is to calculate the spin-spin correlation function $\langle s_i(t)s_j(0)\rangle$ of these dissipative Ising model. Or the equivalent power spectrum in frequency or momentum space.

3.3 Spin chain in a dissipative bath

The model has 3 parts: H_S is the transverse field Ising chain, H_B is the dissipative bosonic bath, H_I is the coupling of the Ising chain with the bath. The influence of environment to the i-th spin in the Ising chain can be completely describe by the correlation $J_i(\omega) = \sum_k c_{i,k}^2 \delta(\omega - \omega_{i,k})$. By assuming Ohmic bath, we are assuming that the correlation takes the linear form at low frequency: $J(\omega) = 2\pi\alpha\omega e^{-\omega/\omega_0}$, where ω_0 is some high energy cut off, it doesn't affect the lower energy physics.

$$H = H_S + H_I + H_B \tag{3.5}$$

$$H_S = -\Delta \sum_{i=1}^{L} \sigma_i^x - J \sum_{i=1}^{L} \sigma_i^z \sigma_{i+1}^z$$

$$H_I = \sum_{i=1}^{L} \sum_{k=1}^{N} c_{i,k} \left(a_{i,k}^\dagger + a_{i,k} \right) \sigma_i^z$$

$$H_B = \sum_{i=1}^{L} \sum_{k=1}^{N} \omega_{i,k}(a_{i,k}^\dagger a_{i,k} + \frac{1}{2})$$

Path integral formalism is carried out to map the quantum Hamiltonian into classical action [7]. The dissipative Bosonic heat bath is traced out, leaving a $1/r^2$ longer range interaction in imaginary time ($\propto \tau$), α becomes A_0. $\sin^2$ is for the periodic boundary condition. [30]

Table 3.1: classical-quantum mapping

quantum	classical	relation
L	N_1	$L = N_1$
β	N_0	$\beta = N_0$
J	K_1	$J = K_1$
Δ	K_0	$\tanh(\Delta) = \exp(-2K_0)$

$$S_{\text{classical action}} = -K_1 \sum \sum s_{i,\tau} s_{i+1,\tau}$$
$$-K_0 \sum \sum s_{i,\tau} s_{i,\tau+1}$$
$$-\frac{\alpha}{2} \sum \sum_{\tau<\tau'} s_{i,\tau} s_{i,\tau'} \left(\frac{\pi}{N_\tau}\right)^2 \frac{1}{\sin^2\left(\frac{\pi}{N_\tau}|\tau-\tau'|\right)} \tag{3.6}$$

3.4 Quantum Monte Carlo method

The Monte Carlo simulation is carried out on system sizes $N_0 \times N_1 = 128 \times 64$ with Wolff clustering updating algorithm. The total updating steps are [Jump] $\times 2^{26}$. Here we update every [Jump] steps to keep the samples as uncorrelated as possible [1]. In order to increase the acceptance rate of long range interaction in the imaginary time, N_0, direction, cumulative probability method is applied [29]. We ran on a single CPU core for two weeks; the relative error for the $I[\omega_n, k]$ (see below) is less than 0.1%.

3.4.1 Updating

In this part, we are going to focus on the Monte Carlo updating algorithm. I am using the Wolff cluster updating method. The essential part of Swendsen-Wang or Wolff algorithm, is to draw bonds between site i and j with probability:

$$p = 1 - \exp(-2K_{ij}\delta_{s_i,s_j}) \tag{3.7}$$

To understand Eq. (3.7), let's take a look at two spin system $S = Ks_1s_2$ [1] There are four states in total, their unnormalized probability can be written as:

$$\uparrow\uparrow = e^K, \uparrow\downarrow = e^{-K}, \downarrow\uparrow = e^{-K}, \downarrow\downarrow = e^K$$

The partition function can be written as

$$Z = Z_{same} + e^{-2K}Z_{diff} = (1 - e^{-2K})Z_{same} + e^{-2K}(Z_{diff} + Z_{same})$$

---

[1] $H = -Js_1s_2$, the probability $P \propto e^{-\beta H} = e^{-\beta(-J)s_1s_2} = e^{Ks_1s_2} = e^S$ where S is the action, K absorbs inverse temperature β and coupling J, wish the sign does not confuse you.

$$= pZ_{connected} + (1-p)Z_{unconnected}$$

When two partion functions $(Z_{diff} + Z_{same})$ are added with equal weight, that means there is no energy difference between them. No bond need to be added as constraint. However, in the case of Z_{same}, it is a constraint (a bond), and the overall weight is given by $p = 1 - e^{-2K}$. That's the probability to given a constraint bond, because there *is* a case that the spins are the same but not connected. After drawing the bonds, we just flip the cluster's spin. This completes one update.

3.4.1.1 Pseudo-codes

Algorithm 1 Wolff algorithm

1: Selection a spin i, append to Q

   (Whenever a spin is append to Q, it is also added to wasQ)

2: **repeat**

3:    Pop the head j out of Q

4:    Find j's neighbour append to Q

     neighbour:={ same color **and** never in Q **and** probability okay }

5: **until** nothing in the Q

6: Flip all elements in wasQ

To get the neighbour of j, we need extra array **wasQ[k]** to chech if k was in Q. Also, I am trying to use hashing instead of converting index from i to (i0,i1,i2,...) then find neigbhours. The neigbour index searching is done many times, so it is wise to use hashing get save repeating calculations. There are two hashing arrays **hashingK[i][h]** (h=1,2,3,...,2d) and **hashingA[i][h]** (h=0,1,2,...,N0-1), they are storing the index of nearest neigbhour and long range neighbour respectively. Their dimensions are: $(N_0 \times \cdots \times N_d) \times 2d$ and $(N_0 \times \cdots \times N_d) \times N_0$. Notice that the two neigbours in N_0 are repeating in two hashing arrays. There is no problem for that, because they represent different couplngs. The couplings are additive in terms of connective probabilities.

3.4.1.2 Sampling long range interaction bonds

As the acceptance rate $p = 1 - e^{-2K}$ is very low for the long range interaction bonds, we don't want do N_0 times to see who is connected by bond. A general problem can be stated as follows:

*Give probability $p_1, p_2, \cdots, p_m$, we wish to select several numbers. Here, p_i means the probability to select i. Instead of running m times **rand()** $\leq p_i$ comparison. We can use the accumulated probability technique.*

$$C_{01} = p_1$$
$$C_{0j} = (1 - p_1) \cdots (1 - p_{j-1}) p_j$$
$$C_{0m} = (1 - p_1) \cdots (1 - p_{m-1}) p_m$$
$$C_{0,m+1} = (1 - p_1) \cdots (1 - p_{m-1})(1 - p_m)$$

C_{0j} means the probability to select j start from 0. Nothing is selected between 0 and j. For the sites after j, it is to be determined later. $C_{0,m+1}$ means nothing is selected among the m numbers. All the accumulated probability summed up to 1. $\sum_{i=1}^{m+1} C_{0,i} = 1$

Suppose we get j after one selection. Then we should do the same jump as start from 0.

$$C_{j,j+1} = p_{j+1}$$
$$C_{j,k} = (1 - p_{j+1}) \cdots (1 - p_{k-1}) p_k$$
$$C_{j,m} = (1 - p_{j+1}) \cdots (1 - p_{m-1}) p_m$$
$$C_{j,m+1} = (1 - p_{j+1}) \cdots (1 - p_{m-1})(1 - p_m)$$

This procedure is done iteratively, until we hit the end. The last few element need to be carefully treated. $C_{m,m+1} = 1$ means to exit this procedure.

$$C_{m-1,m} = p_m$$
$$C_{m-1,m+1} = (1 - p_m)$$
$$C_{m,m+1} = 1$$

Algorithm 2 Luijten algorithm

1: Prepare $p_1, \cdots, p_m$ and $C_{01}, \cdots, C_{0m}, C_{12}, \cdots, C_{2m}, C_{23}, \cdots, C_{m-1,m}$

    Begin at 0, set i=0

2: **repeat**

3:    Generate a $[0,1)$ random number r

4:    Locate j such that $C_{ij} \leq r < C_{i,j+1}$

5:    Set $i = j$, push j to Q

6: **until** i = m+1

7: Flip all elements once in Q

3.4.1.3 Time complexity notes

There are a few places, where time complexity can be improved.

1. **Locate i such that $a[i] \leq r < a[i+1]$.** For an array a[N] with length N, simple method would take O(N) time. If we use order list data structure, the search time becomes $O(\log(N))$.

2. **Check if s[j] is already in the cluster.** This is done many times in one update loop. I should create a global variable flag[i] to show if i is already in the cluster. This takes only O(1) time to check. But the drawback is, we need to reset flag[i] to zero every loop, which takes O(N) time. Anyway this runs every loop, and we can combine this O(N) reset zero procedure with the cluster flip together. Then it should in total cost O(cluster size) time each loop.

3. **No wasQ is needed.** Flip the sign at the same time of push to the Q. s[loc] is flipped during the cluster growth: this prevents revisiting sites already included in the cluster.

In case of anti-ferromagnetic coupling, the sites should be connected if the have opposite sign. To increase the CPU speed of accessing the sites and the neighbours of a site. We are using the hashing rules as follows:

Algorithm 3 Wolff algorithm 2

1: Selection a spin i, append to Q

(whenever a spin is append to Q, also flip the sign)

2: **repeat**

3:     Pop the head j out of Q

4:     Find j's neighbour append to Q

neighbour:={ same color **and** probability okay }

5: **until** nothing in the Q

---

1. **Rule for sites.** Suppose the dimension runs for $N_0, N_1, N_2, \cdots$. The site $(i_0, i_1, i_2, \cdots)$ where $i_n = 0, 1, \cdots, N_n - 1$. The FORTRAN notation

$$s = i_0 + N_0 * (i_1 + N_1 * (i_2 + \cdots))$$

2. **Rule for sites' neighbour** The general philosophy is "(1) lower index dimension comes first; (2) long range first, nearest neighbour second; (3) if site collides, first absorbs second (4) left first, right second; "

3. **0+1 D with long range** N_0

$$\text{hashing}[N_0][N_0 - 1]$$

4. **1+1 D with long range** N_0, N_1

$$\text{hashing}[N_0 * N_1][(N_0 - 1) + 2]$$

3.4.1.4   Programs

```
1  class  Ising
2  {
3      int  dimension;
4      vector<int> N;
5      vector<doube> K;
6      double  A;
```

```
 7
 8      int *s;
 9      int *flag;
10
11      int hashingK;
12
13      updating()
14      {
15          Q
16          wasQ
17      }
18 }
```

Code 3.1: Ising.h

Each simulation's input is:

- Dimension d

- Length vector $N_0, N_1, N_2, \cdots$

- Nearest coupling vector $K_0, K_1, K_2, \cdots$

- Long range coupling in 0-direction A_0

To store the spin array $s[i_0, i_1, \cdots, i_{d-1}]$ in d-dimensional space, I am using Fortran order (column-major order) array, then the index becomes one dimension $s[i]$

$$i = i_0 + N_0 * (i_1 + N_1 * (i_2 + \cdots))$$

The zeroth dimension data is stored continuously, as there is long range interaction in the dimension naturally. The power spectrum $I[k_0, k_1, \cdots, k_{d-1}]$ is the absolute squared FFT of $s[i_0, i_1, \cdots, i_{d-1}]$

$$\tilde{s}[k_0, k_1, \cdots, k_{d-1}] = \mathbf{FFT}\big[s[i_0, i_1, \cdots, i_{d-1}]\big] \tag{3.8}$$

$$I[k_0, k_1, \cdots, k_{d-1}] = |\tilde{s}[k_0, k_1, \cdots, k_{d-1}]|^2 \tag{3.9}$$

To store d-dimensional I into one-d, I'm using the same FORTRAN order. All of the indices k_p and i_p are periodic in N_p

3.4.2   Order parameters

Order parameters are key to understand phase transitions. Instead of magnetization, Binder ratio is more often used in Monte Carlo simulation, because of its scale invariant property.

$$m = \frac{1}{[R]} \sum_{i \in R} s_i \tag{3.10}$$

$$\langle |m| \rangle = \frac{1}{T} \sum_{n=1}^{T} \left| \frac{1}{[R]} \sum_{i \in R} s_i \right| \tag{3.11}$$

$$\langle m^2 \rangle = \frac{1}{T} \sum_{n=1}^{T} \left(\frac{1}{[R]} \sum_{i \in R} s_i \right)^2 \tag{3.12}$$

$$\langle m^4 \rangle = \frac{1}{T} \sum_{n=1}^{T} \left(\frac{1}{[R]} \sum_{i \in R} s_i \right)^4 \tag{3.13}$$

The index $m = 1, 2, 3, \cdots, T$ labels the Monte Carlo step. R is region of interests. It does not have to be the entire region. For example, in the two qubits problem. R_1 and R_2 are the two spins respectively.

$$R_2 = \frac{\langle m^4 \rangle}{\langle m^2 \rangle^2} \tag{3.14}$$

$$U_2 = 1.5 - 0.5 R_2 \tag{3.15}$$

In the infinite system size limit, Binder ratio R_2 takes 1 at magnetic ordered phase, and takes 3 at disorder phase (as a result of Gaussian distribution). The value of Binder ratio is dimensionless, it is scale invariant. We can define a U_2 which takes 1 in the ordered phase and 0 in the disordered phase.

3.4.2.1 Correlation

Due the periodic boundary condition, the correlation function is also periodic is space (and imaginary time)

$$\langle \textbf{correlation} \rangle = \frac{1}{T} \sum_{n=1}^{T} \left(\sum_{i \in R} s_{1i} s_{2i} \right) \tag{3.16}$$
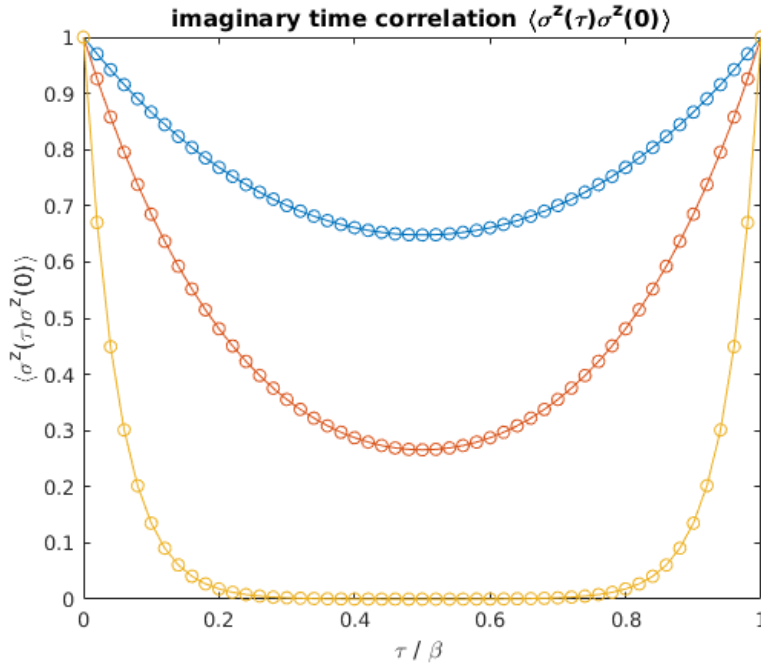
Figure 3.4: Spin-spin correlation function is a periodic function.

3.4.3 Spin-spin correlation

The standard method   Given 2D Ising spin $s[\tau, x] = \pm 1$ on a discrete lattice with periodic boundary condition, where $\tau \in \{0, 1, 2, \cdots N_0 - 1\}$ is in the imaginary time direction and $x \in \{0, 1, 2, \cdots N_1 - 1\}$ is in the spatial direction, our goal is to calculate spin-spin correlation function $c[\tau, x] = \langle s[0, 0] s[\tau, x] \rangle$. Here $\langle \cdots \rangle$ is the Monte Carlo average. Since our problem is translational invariant. We also have $c[\tau, x] = \langle s[1, 1] s[1+\tau, 1+x] \rangle = \langle s[1, 2] s[1+\tau, 2+x] \rangle = \cdots = \langle s[\tau_0, x_0] s[\tau_0 + \tau, x_0 + x] \rangle$ for any initial site τ_0, x_0. Therefore we can write the correlation

73

function as:

$$c[\tau, x] = \left\langle \frac{1}{N_0 N_1} \sum_{\tau_0=0}^{N_0-1} \sum_{x_0=0}^{N_1-1} s[\tau_0, x_0] s[\tau_0 + \tau, x_0 + x] \right\rangle \qquad (3.17)$$

We need to perform $N_0 N_1$ multiplications to get one value of $c[\tau, x]$. There are $N_0 N_1$ values of $c[\tau, x]$ for each index $[\tau, x]$. Therefore, to get a 2D correlation function $c[\tau, x]$, we need $O((N_0 N_1)^2 M)$ total multiplications. Where M is the Monte Carlo updating steps. Then we can perform a 2D discrete Fourier transform on $c[\tau, x]$ to get the $I[\omega_n, k]$

$$I[\omega_n, k] = \frac{1}{\sqrt{N_0 N_1}} \sum_{\tau=0}^{N_0-1} \sum_{x=0}^{N_1-1} e^{i(\tau \omega_n + xk)} c[\tau, x] \qquad (3.18)$$

If we make the analytic continuation from Matsubara frequency $i\omega_n$ to real frequency ω, the function $I[\omega_n, k]$ becomes $S[\omega, k]$. It is the dynamical structure factor of the quantum spin system.

A faster method   The convolution theorem and fast Fourier transform can make the above calculation faster. The acceleration is from $O((N_0 N_1)^2 M)$ to $O(N_0 N_1 \log(N_0 N_1) M)$. The equation is given by

$$I[\omega_n, k] = \left\langle \left| \tilde{s}[\omega_n, k] \right|^2 \right\rangle \qquad (3.19)$$

Where $\tilde{s}[\omega_n, k]$ is the 2D discrete Fourier transformation of the Ising spin field $s[\tau, x]$

$$\tilde{s}[\omega_n, k] = \frac{1}{\sqrt{N_0 N_1}} \sum_{\tau=0}^{N_0-1} \sum_{x=0}^{N_1-1} e^{i(\tau \omega_n + xk)} s[\tau, x] \qquad (3.20)$$

We have used the fact that the order of the Fourier transform and the summation can be exchanged due to linearity. Equation (3.20) and 3.19) will give the same $I[\omega_n, k]$ as Eqs. (3.17) and (3.18), but with a logarithmic acceleration.
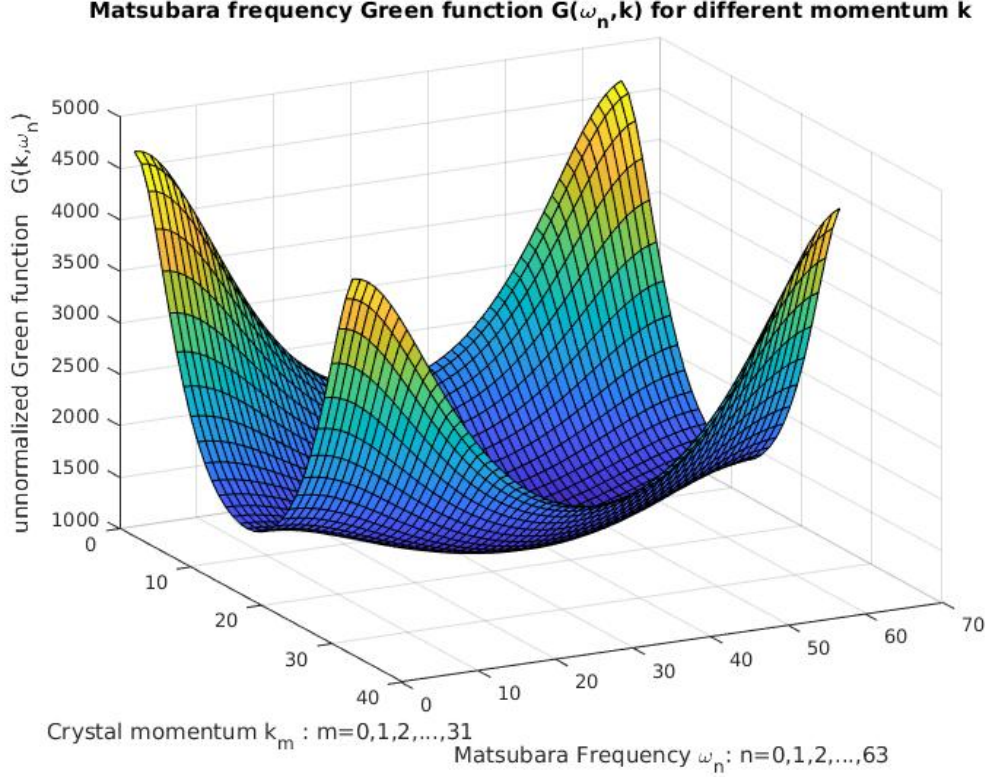
Figure 3.5: Fourier transformation of 2D spin-spin correlation function.

3.4.4 Analytic continuation

To begin, we have a classical system of size $N_0 \times N_1 = 128 \times 64$. Consider the correlation $C[\tau, x] = \langle s[\tau_0, x_0] s[\tau_0 + \tau, x_0 + x] \rangle$ and perform a 2D discrete Fourier transformation on $C[\tau, x]$, to get $I[\omega_n, k]$, which is also the quantum $G(i\omega_n, k)$. The values of ω_n, k run through discrete points in the Brillouin zone. Where $\Omega = \frac{2\pi}{\beta} = \frac{2\pi}{N_0}$ is the Matsubara frequency interval.

$$G(i\omega_n, k) \equiv I[\omega_n, k] \qquad (3.21)$$

$$\omega_n = 0, \Omega, 2\Omega, \cdots, (N_0 - 1)\Omega$$

$$k = 0, \frac{2\pi}{N_1}, 2\frac{2\pi}{N_1}, \cdots, (N_1 - 1)\frac{2\pi}{N_1} \qquad (3.22)$$

$$G(i\omega_n, k) \to G(\omega + i0^+, k) \to S(\omega, k) \qquad (3.23)$$

The analytic continuation Eq. (3.23) is done for each fixed k value, using our newly developed Páde regression method [53]. The Páde regression assumes the analytic function $G(z)$ takes the specific form of a rational function $\frac{P_L(z)}{P_M(z)} = \frac{a_0 + a_1 z + \cdots + a_L z^L}{1 + b_1 z + \cdots + b_M z^M}$. The polynomial in the numerator is of degree is L and the denominator is of degree M. Therefore there are $L + M + 1$ parameters to be determined. Given N Matsubara points, there are N fitting equations $G(z_n = i\omega_n) = u_n$ $(n = 1, 2, \cdots, N)$. We then modify the problem to a linear regression problem: given $\mathbf{X}$ and $\mathbf{y}$ find the β that minimizes $||\mathbf{X}\beta - \mathbf{y}||^2$. Here the explicit form of $\mathbf{X}_{N \times (L+M+1)} \beta_{(L+M+1)} = \mathbf{y}_N$ is in Eq. (3.24)

$$
\begin{pmatrix}
-u_1 z_1^1 & -u_1 z_1^2 & \dots & z_1^0 & z_1^1 & z_1^2 & \dots \\
-u_2 z_2^1 & -u_2 z_2^2 & \dots & z_2^0 & z_2^1 & z_2^2 & \dots \\
\vdots & \vdots & \vdots & \vdots & \vdots & \vdots & \vdots \\
\vdots & \vdots & \vdots & \vdots & \vdots & \vdots & \vdots \\
\vdots & \vdots & \vdots & \vdots & \vdots & \vdots & \vdots \\
\vdots & \vdots & \vdots & \vdots & \vdots & \vdots & \vdots \\
\vdots & \vdots & \vdots & \vdots & \vdots & \vdots & \vdots \\
-u_N z_N^1 & -u_N z_N^2 & \dots & z_N^0 & z_N^1 & z_N^2 & \dots
\end{pmatrix}
\begin{pmatrix}
b_1 \\
b_2 \\
\vdots \\
\vdots \\
\hline
a_0 \\
a_1 \\
a_2 \\
\vdots
\end{pmatrix}
=
\begin{pmatrix}
u_1 \\
u_2 \\
\vdots \\
\vdots \\
\vdots \\
\vdots \\
u_{N-1} \\
u_N
\end{pmatrix}
\tag{3.24}
$$

Starting from this standard linear regression problem, we can apply Bayesian inference to choose the optimal L and M or use bootstrapping to estimate the error.

3.5 Result

3.5.1 Calibration

Let's first look at the case without dissipation. This is just the transverse field Ising model; the exact spectrum is $\epsilon(k) = \sqrt{\Delta^2 + J^2 - 2\Delta J \cos(k)}$. Therefore we can use the exact result to verify our Monte Carlo plus analytic continuation approach. The classical-quantum mapping, will map $K_0 = 0.136, K_1 = 0.2, N_0 = 128, N_1 = 64$ to the quantum parameter $\Delta = 1, J = 0.2, \beta = 128, L = 64$.

Fig 3.7 is the $S(\omega, k)$ result for each individual k. Lower momenta have always higher spectral weight. We can also see the symmetry of the spectrum, $S(\omega, k)$ and $S(\omega, 2\pi - k)$ have the same shape: Fig 3.6 is the color version. The blue dashed line is the exact spectrum $\omega(k) = \sqrt{1 + 0.2^2 - 2 \times 0.2 \cos(k)}$, we can see that the exact result and the analytic continuation agree reasonably well.
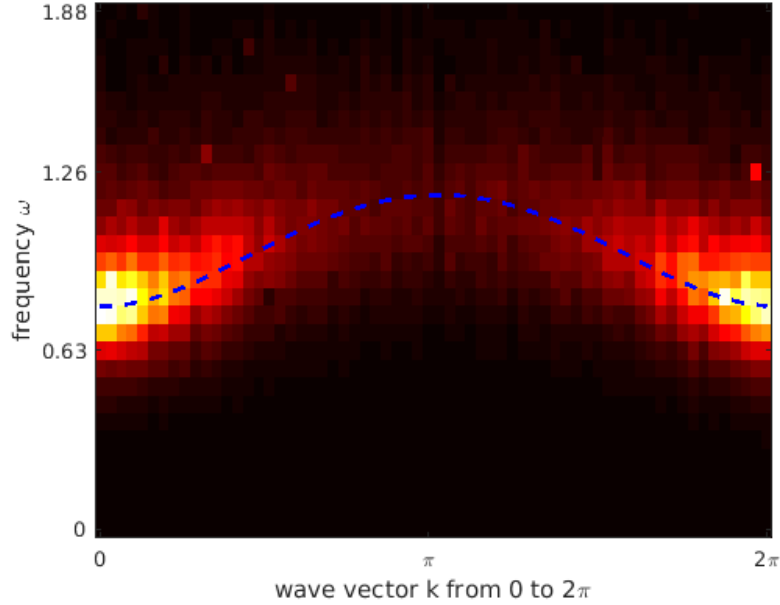
Figure 3.6: $S(\omega, k)$ of transverse field Ising chain $\Delta = 1.0, J = 0.2$ with no dissipation, $\alpha = 0$. The recovered spectrum is compared with the exact result (the dashed blue curve).

The broadening is due to two reasons (1) finite size (classical $N_0 = 128$) or the finite temperature effects (quantum $T = 1/\beta = 1/N_0$) ; (2) our current Monte Carlo imaginary time correlation function has 5 significant digits (relative error 10^{-5}), which is still a large error.

3.5.2 Spectrum with dissipation

We turn on the dissipative strengths to be $\alpha = 0.05, 0.1, 0.2, 0.3, 0.5$. Fig. (3.8 3.9 3.10 3.11 3.12) are the spectral plots for individual k. Fig. (3.13 3.14 3.15 3.16 3.17) are the corresponding density plots of $S(\omega, k)$. From these results, we can see that as the dissipation

strength is increased, the energy peak is shifted down. The energy distributions also get broadened, implying shorter life time of the quasi-particle excitation.

Figure 3.7: Transverse field Ising chain $\Delta = 1.0, J = 0.2$ with no dissipation $\alpha = 0$. Each curve is $S(\omega, k)$ with fixed k value.

The energy gap is more subtle. Only in the non-dissipative system, can we observe a clean energy gap. As the dissipation is turned on a little bit, it forms a pseudo-gap, and closes softly. At low energies $S(\omega) \propto \omega^\delta$, we can classify the gap closing into three cases: $\delta > 1$ soft closing, $\delta = 1$ linear closing, $\delta < 1$ hard closing. The low energy exponent $\delta = \delta(\alpha, k)$ is a function of dissipation strength α, and momentum k.

For $\alpha = 0.1$, see Fig 3.9. The spectral curve is convex at low energy for all momentum. $\delta(0.1, k) < 1$ For $\alpha = 0.2$, see Fig 3.10. It's very interesting. At low momentum, the spectrum is convex $\delta > 1$, while at high momentum, the spectrum is concave $\delta < 1$. And there exist a special momentum k_c such that the dispersion is linear $\delta(\alpha, k_c) = 1$, which divides the convex and concave regions. (in the $\alpha = 0.2$ case, it is $k_c \approx \frac{\pi}{2}, \pi$) For $\alpha = 0.3$, see Fig 3.11. The spectrum shifts to low frequency and the gap is closing. The low energy
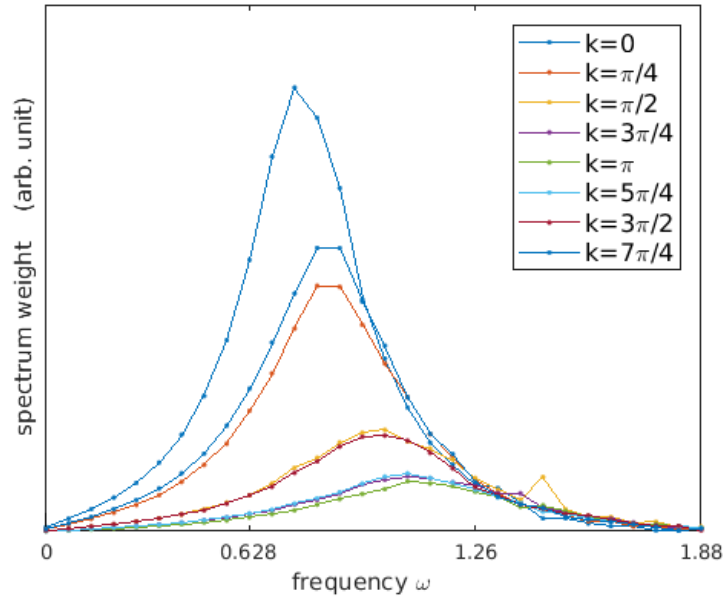
Figure 3.8: Transverse field Ising chain $\Delta = 1.0, J = 0.2$ with dissipation $\alpha = 0.05$. Each curve is $S(\omega, k)$ with fixed k value.
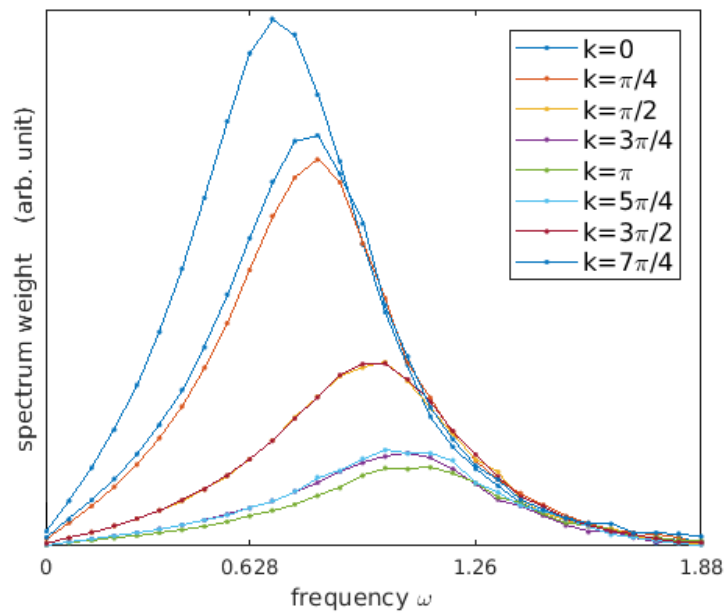
Figure 3.9: Transverse field Ising chain $\Delta = 1.0, J = 0.2$ with dissipation $\alpha = 0.1$. Each curve is $S(\omega, k)$ with fixed k value.
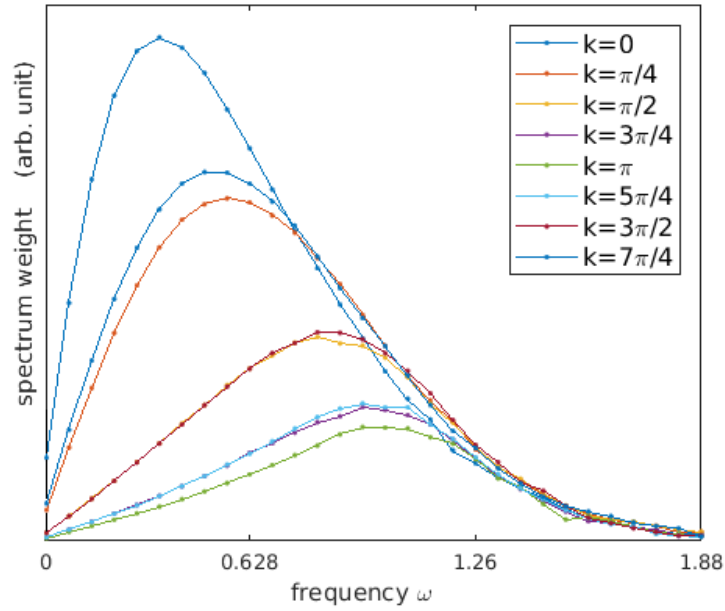
Figure 3.10: Transverse field Ising chain $\Delta = 1.0, J = 0.2$ with dissipation $\alpha = 0.2$. Each curve is $S(\omega, k)$ with fixed k value.
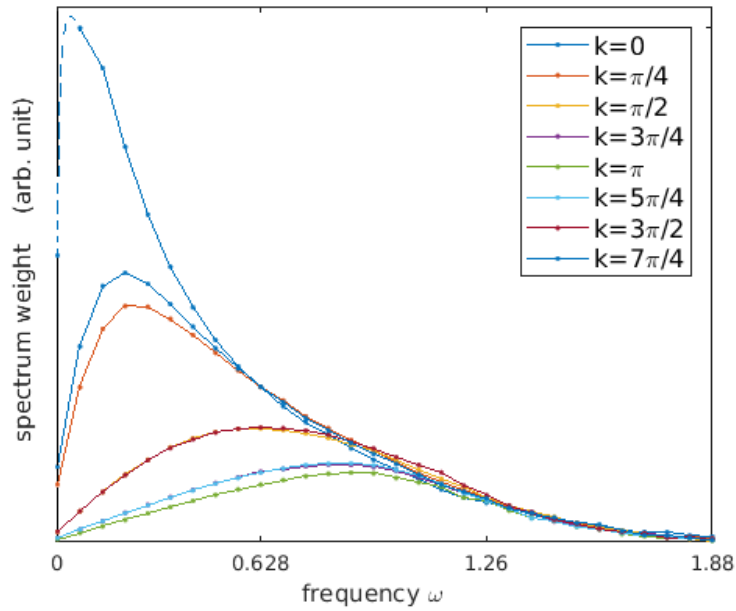
Figure 3.11: Transverse field Ising chain $\Delta = 1.0, J = 0.2$ with dissipation $\alpha = 0.3$. Each curve is $S(\omega, k)$ with fixed k value. The $k = 0$ curve changes violently near zero frequency, we use dashed line to interpolate.
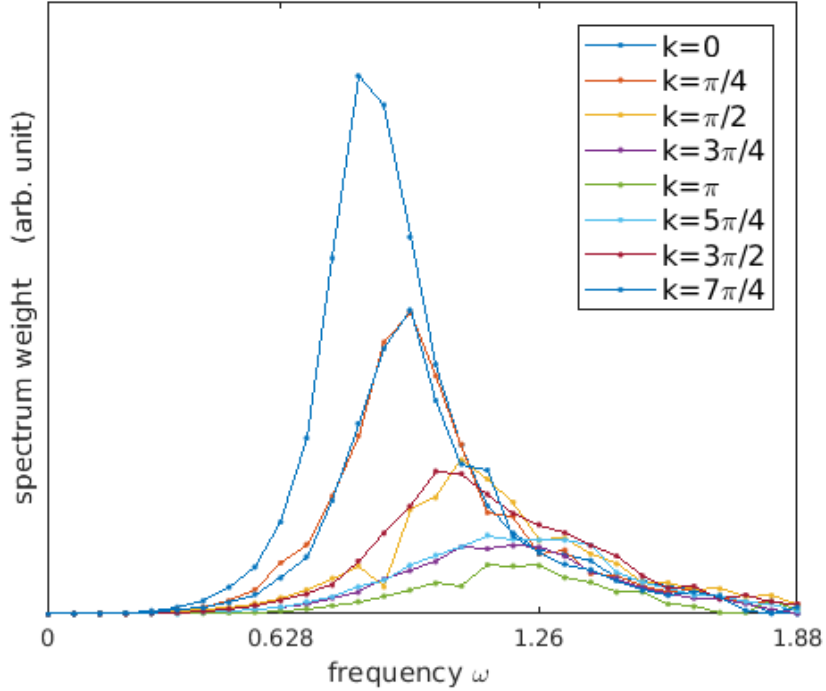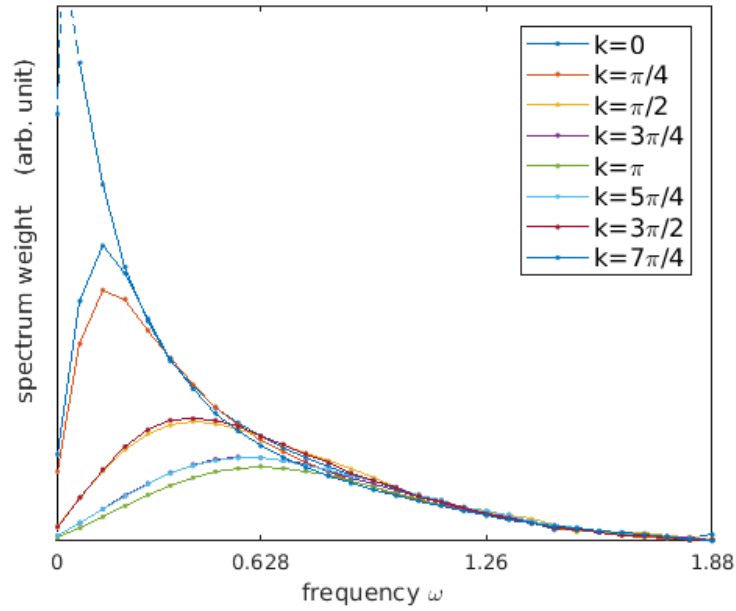
Figure 3.12: Transverse field Ising chain $\Delta = 1.0, J = 0.2$ with dissipation $\alpha = 0.5$. Each curve is $S(\omega, k)$ with fixed k value. The $k = 0$ curve changes violently near zero frequency, the peak will be out of the graph. We use dashed line to interpolate.
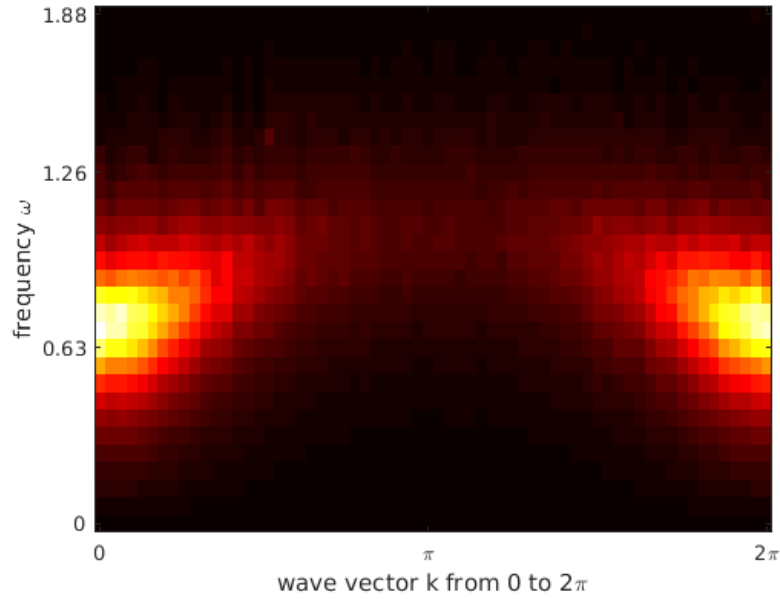
Figure 3.13: $S(\omega, k)$ of transverse field Ising chain $\Delta = 1.0, J = 0.2$ with dissipation $\alpha = 0.05$.

81
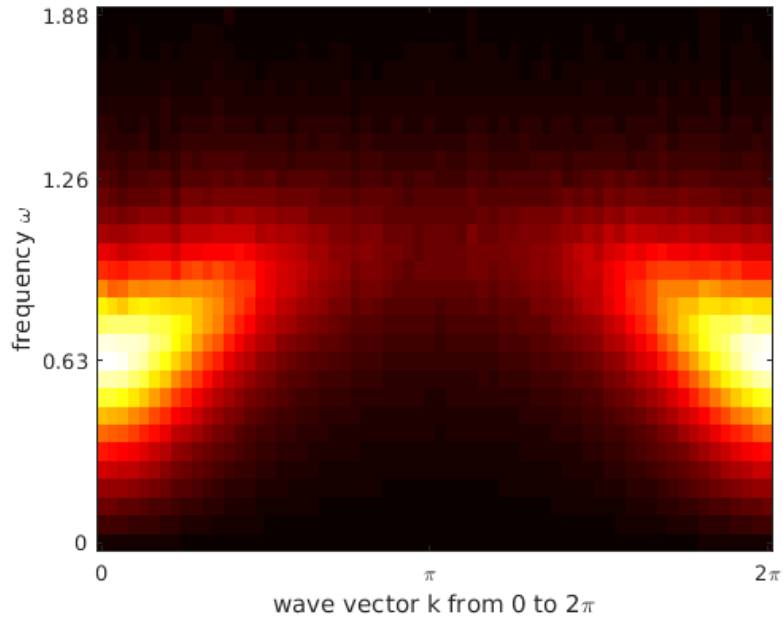
Figure 3.14: $S(\omega, k)$ of transverse field Ising chain $\Delta = 1.0, J = 0.2$ with dissipation $\alpha = 0.1$.
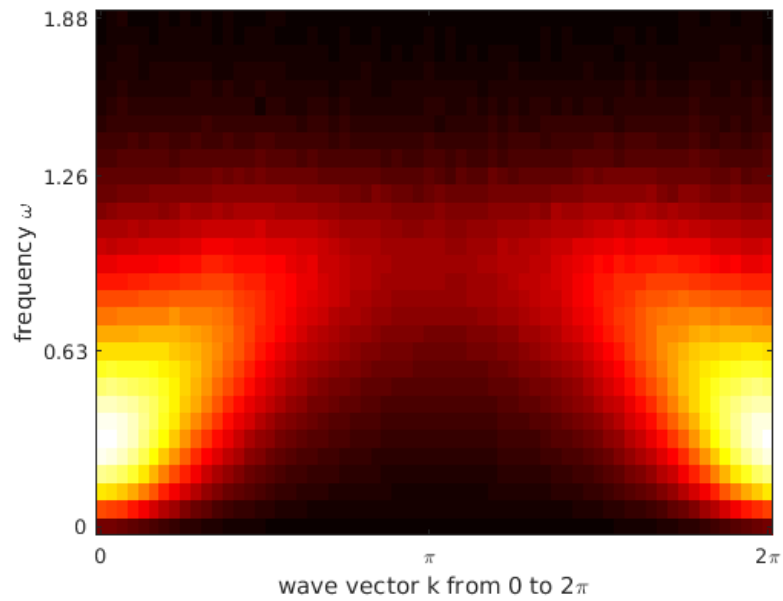
Figure 3.15: $S(\omega, k)$ of transverse field Ising chain $\Delta = 1.0, J = 0.2$ with dissipation $\alpha = 0.2$.
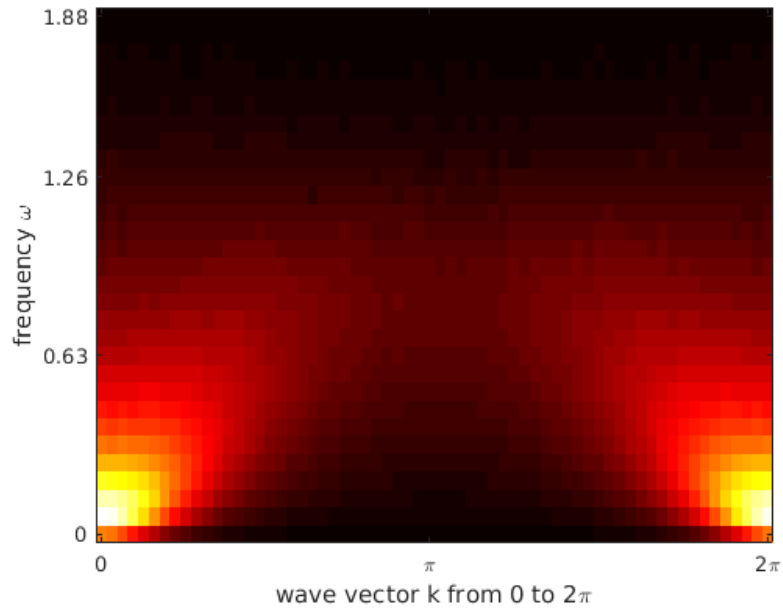
Figure 3.16: $S(\omega, k)$ of transverse field Ising chain $\Delta = 1.0, J = 0.2$ with dissipation $\alpha = 0.3$.
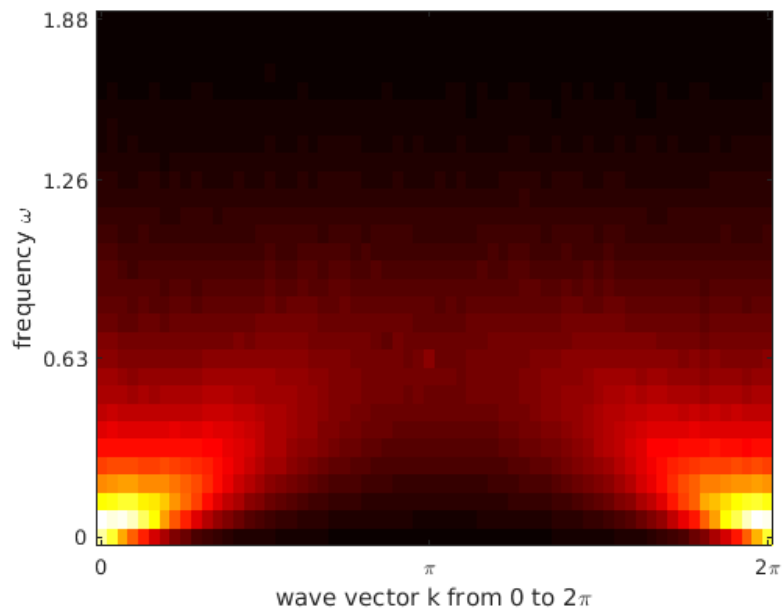
Figure 3.17: $S(\omega, k)$ of transverse field Ising chain $\Delta = 1.0, J = 0.2$ with dissipation $\alpha = 0.5$.

shape is concave ($\delta < 1$) for all momenta.

3.5.3   Three dynamical phases

As dissipation is turned on, the low momentum spectrum gets damped faster than the high momentum, in terms of the δ value. Therefore we can classify the system into three different regions:

1. Weakly damped region

2. Linear k-edge region

3. Strongly damped region

In Fig 3.18, the schematics of these three regions are plotted. Fig 3.19 is the phase diagram. The light yellow and grey region correspond to the magnetically disordered and ordered phases in the imaginary time simulation. Green, red, blue dots correspond to the three dynamical phases of the real time spectra.
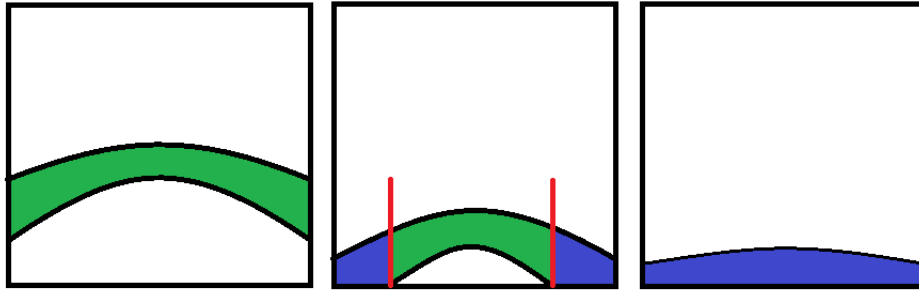
Figure 3.18: A schematic showing three dynamical phases (from left to right: weak damped $\alpha = 0.1$, linear k-edge $\alpha = 0.2$, strong damped $\alpha = 0.3$). The horizontal axis is k, the vertical axis is ω, same as Fig. (3.14,3.15,3.16). The band is colored green if $\delta(k) > 1$, blue if $\delta(k) < 1$ and red if $\delta(k) = 1$.

In the limit of zero dissipation, it is the transverse field Ising model, which is an integrable system. For each k the excitation has infinite life time. In the limit of large dissipation, the
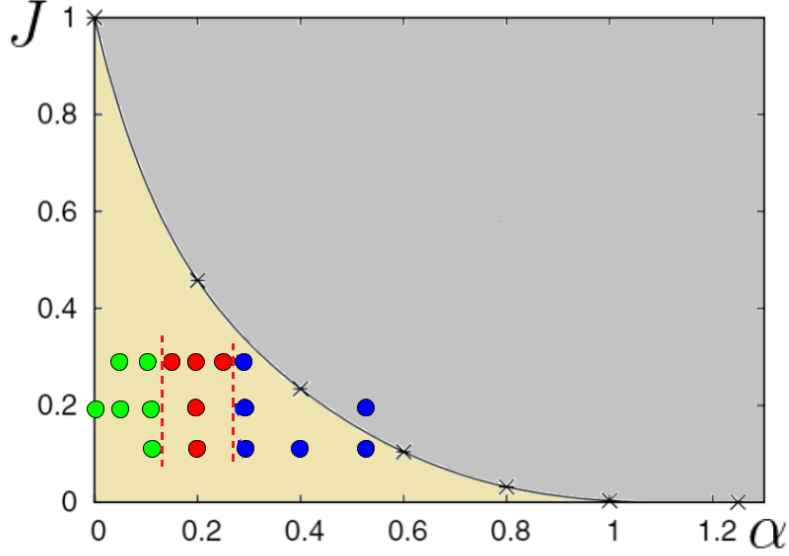
Figure 3.19: Phase diagram of dissipative Ising chain. Vertical axis J is the nearest neighbour $\sigma_i^z \sigma_{i+1}^z$ coupling, horizontal axis α is the dissipation strength, transverse field is set to $\Delta = 1$ or $K_0 = 0.136$. The yellow and grey regions are the disordered and ordered magnetic phases from the imaginary time simulation [57]. Green, red, and blue dots represent weakly damped, linear k-edge, and strongly damped regions respectively.

Hamiltonian is dominated by the environmental noise term. The quasi-particles will decay faster than its energy time scale. In the intermediate dissipation range, low momentum will not have quasi-particle excitation, while high momentum will. The critical damping edge momentum k_c, is given by $S(\alpha, \omega, k_c) \propto \omega$.

3.6 Conclusion

To summarize, we have used extensive quantum Monte Carlo simulation, plus the rational function (Padé) regression method to recover the spectra of the dissipative Ising chain. As

the dissipation strength is increased, the spectral speak is broadened and lowered in energy. Quasi-particle picture $S(\omega, k) = \delta(\omega - \omega(k))$ does not hold; $\frac{1}{\omega - \omega'(k) - i\omega''(k)}$ is generalized to an arbitrary rational function. According to lower energy exponent of $S(\omega, k) \sim \omega^{\delta(k)}$ three dynamical regions are introduced to understand the role of dissipation.

APPENDIX A

Python package for transverse field Ising chain

The software package works as follows. The input are coefficient of Hamiltonian, which is represented by M. If it is the disordered system, then the input should be an ensemble of Ms. We are using the input to create an object. Then use that object to calculate various physical quantities.

A.1   Transverse field Ising model package (tfim)

In the following github repository, the folder "package" contains the code.

https://github.com/Jian2017/python_package_for_tfim_0.0

```python
class tfim(object):
    def __init__(self,M):
        return none

    def correlator_equal_time(self,i,j):
        return # equal time correlator of site i and site j
    def correlator_equal_time_Matrix(self):
        return # a matrix

    def correlator_dynamics(self,i,t,j):
        return # correlator of site i and j at time t
    def correlator_dynamics_sector(self,i,j,dt,tSteps):
        return # a sector
    def Swk(self,i,j,dt,tSteps):
        return # a sector, the dynamical structure factor
```

```
16
17      def correlator_dynamics_AABB(self,i,t,j,AABB):
18          return # out of time order correlator
19      def correlator_dynamics_sector_AABB(self,i,j,dt,tSteps):
20          return # a sector of OTOC
21
22      def orderParameter_1(self):
23          return # magnetization
24      def orderParameter_2(self):
25          # this is the Edward-Anderson order parameter
26          # for a single quenced configuration
27          # disorder average need to be done, for better convergence
```

Code A.1: tfim.py

```
1  from package.hamiltonian import simplePureHamiltonian
2  from package.PPFtfim import *
3  import matplotlib.pyplot as plt
4
5  M=simplePureHamiltonian(20,1,1,-0.3) #create Hamiltonian matrix
6  t=tfim(M) #create the transverse field Ising model object using matrix M
7
8  mat=t.correlator_equal_time_Matrix()
9
10 plt.matshow(mat)
11 plt.colorbar()
12 plt.show()
```

Code A.2: Create an object t.

A.2 Pfaffian package

The the following github repo is the python package assessing the Pfaffian. The time complexity is $O(N^3)$: https://github.com/Jian2017/python_package_assessing_pfaffian

```python
import numpy as np
from pf import pf

N=20
X=np.random.random((2*N,2*N))
S=X.transpose()-X

pf(S)   # evaluting the pfaffian of matrix S
```

Code A.3: the Pfaffian package

APPENDIX B

Matlab package for Padé regression

The essential code is in the file "PadeRegression.m" in the following repository:

https://github.com/condensedmatter/PadeRegression_Matlab

```matlab
function [rho_best,rho_error]=PadeRegression(z,u_real,u_imag,err_u_real,
    err_u_imag,x,RR)
%% average over RR Pade-Regressions
% best value and standard error is produced
rho_ensemble=zeros(RR,size(x,2)*size(x,1));
parfor R=1:RR
    rho_ensemble(R,:)=PadeRegressionOne(z,u_real,u_imag,err_u_real,err_u_imag,
    x,R);
end
rho_best=mean(rho_ensemble);
rho_error=std(rho_ensemble);
end
```

Code B.1: Bootstrapping size is RR.

APPENDIX C

CPP codes for longer range Ising model

The cpp source codes are in the following github repository:

https://github.com/condensedmatter/SpinBosonND_cpp

C.1 Updating and FFT spectrum

```cpp
#include <cmath> //exp()
#include <random>  // class my_random{};
#include <numeric> // accumulate();

class Ising{
    bool *s;//pointer to the Ising field

    Ising(int N0,double K0,double A0);
    Ising(int N0,int N1,double K0,double K1,double A0);
    Ising(int N0,int N1,int N2,double K0,double K1,double K2,double A0);

    void updating();
    void updating(int n);//update n times
}
```

Code C.1: Ising.h

```cpp
#include <fftw3.h>

class powerSpectrum{
    double * m_spectrum;//output is here
```

```
5
6     powerSpectrum(int N0 );
7     powerSpectrum(int N0, int N1);
8     powerSpectrum(int N0, int N1, int N2);
9
10    void calculate(bool *s);//input is here
11 }
```

Code C.2: calculate_powerSpectrum.h

This header file calculates the power spectrum of s and stores it in m_spectrum.

C.2   Averaging and saving files

```
1 class writeFiles{
2     writeFiles(int seed);//create a file writing obj, seed as part of name
3     void save(vector<double> vd);//save spectrum vd as "00seed_00count.txt"
4 }
5
6 class Summation{
7     std::vector<double> c;
8     Summation(int spinsize ,int sumN);//initialize
9     void add(double *s);
10    void ave();
11 }
```

Code C.3: file_generator.h

C.3   Main program

Random seeds need to be changed each time when we add a new parallel Monte Carlo
process. This main function takes argv[1] as the parameter for different seeds.

```
1 #include "file_generator.h"
2 #include "calculate_powerSpectrum.h"
3 #include "Ising.h"
4
```

```cpp
#include <iostream>
#include <string>
#include <ctime>

int main(int argc, char const *argv[]) {

    //large enough
    int thremoLOOPS=1000*500;
    int LOOPS=1000000;

    //set to be optimal by  main_proj_1.cpp
    int sumN=800000;
    int J=610;

    //set seed  from arguments
    int seed=3;
    seed=std::stoi(argv[1]);
    rng.mt.seed(seed);



    //this is the physics parameters
    int N0=128;
    int N1=64;
    double K0=0.136;
    double K1=0.2;
    double alpha=0.2;

    Ising e1(N0,N1,  K0, K1 , alpha);
    powerSpectrum pw(N0,N1 );

    /****** parameters are above this line ***********/

    Summation s(e1.Ntotal,sumN);
```

```cpp
39    writeFiles w(seed);

40

41    e1.updating(thremoLOOPS);

42

43    for (size_t i = 0; i < LOOPS; i++) {
44        std::cout << i << '\n';
45        s.zero();
46        for (size_t j = 0; j < sumN; j++) {
47            e1.updating(J);
48            pw.calculate(e1.s);
49            s.add(pw.m_spectrum);
50        }
51        s.ave();
52        w.save(s.c);
53    }

54

55    return 0;
56 }
```

Code C.4: main_proj_2.cpp

C.4   Submitting job arrays in cluster

First we need compile above c++ source codes.

```bash
1 #!/bin/bash
2 FFTW3_HOME="/u/local/apps/fftw3/current"
3
4 echo $FFTW_HOME
5 . /u/local/Modules/default/init/modules.sh
6
7 module load intel/13.cs
8 module load gcc/4.9.3
9
```

```
10 g++ −static −std=c++11 main_proj_2.cpp −o main_proj_2 −I$FFTW3_HOME/include −
     L$FFTW3_HOME/lib −lfftw3 −lm
```

Code C.5: compile.sh

After this step, we have "main_proj_2" executable file, we need to set the permission by command "chmod 777 main_proj_2"

```
1 #!/bin/bash
2 echo $SGE_TASK_ID
3 ./main_proj_2 $SGE_TASK_ID
```

Code C.6: jobarray.sh

```
1 #!/bin/bash
2 qsub −cwd −V −N PJ −l h_data=1024M, h_rt=24:00:00 −M $HOME −m bea −t 1−500:1
     jobarray.sh
```

Code C.7: submit500.sh

The above syntax is used for Hoffman2 cluster. To submit more jobs:

```
1 #!/bin/bash
2 ./submit500.sh
3 ./submit1000.sh
4 ./submit1500.sh
5 ./submit2000.sh
```

Code C.8: all_submit.sh

Bibliography

[1] Note link: What is the optimal MCMC jumping step?

[2] L.-F. Arsenault, R. Neuberg, L. A. Hannah, and A. J. Millis. Projected regression method for solving Fredholm integral equations arising in the analytic continuation problem of quantum physics. *Inverse Problems*, 33(11):115007, November 2017.

[3] K. S. D. Beach. Identifying the maximum entropy method as a special limit of stochastic analytic continuation, 2004.

[4] K. S. D. Beach, R. J. Gooding, and F. Marsiglio. Reliable padé analytical continuation method based on a high-accuracy symbolic computation algorithm. *Phys. Rev. B*, 61:5147–5157, Feb 2000.

[5] Piet W. Brouwer, Mathias Duckheim, Alessandro Romito, and Felix von Oppen. Probability distribution of majorana end-state energies in disordered wires. *Phys. Rev. Lett.*, 107:196804, Nov 2011.

[6] Matthew W. Butcher, J. H. Pixley, and Andriy H. Nevidomskyy. Efficient monte carlo simulation of a dissipative ising chain. *AIP Advances*, 8(10):101415, 2018.

[7] Sudip Chakravarty and Anthony J. Leggett. Dynamics of the two-state system with ohmic dissipation. *Phys. Rev. Lett.*, 52(1):5–8, jan 1984.

[8] Sudip Chakravarty and Joseph Rudnick. Dissipative dynamics of a two-state system, the kondo problem, and the inverse-square ising model. *Phys. Rev. Lett.*, 75:501–504, Jul 1995.

[9] J. Ignacio Cirac and Peter Zoller. Goals and opportunities in quantum simulation. *Nature Physics*, 8(4):264–266, apr 2012.

[10] R. Coldea, D. A. Tennant, E. M. Wheeler, E. Wawrzynska, D. Prabhakaran, M. Telling, K. Habicht, P. Smeibidl, and K. Kiefer. Quantum criticality in an ising chain: Experimental evidence for emergent e8 symmetry. *Science*, 327(5962):177–180, jan 2010.

[11] Arnab Das and Bikas K. Chakrabarti. Colloquium. *Rev. Mod. Phys.*, 80:1061–1081, Sep 2008.

[12] H. Dekker. Noninteracting-blip approximation for a two-level system coupled to a heat bath. *Physical Review A*, 35(3):1436–1437, feb 1987.

[13] Amit Dutta, Gabriel Aeppli, Bikas K. Chakrabarti, Uma Divakaran, Thomas F. Rosenbaum, and Diptiman Sen. Quantum phase transitions in transverse field spin models: from statistical physics to quantum information, 2010.

[14] Romain Fournier, Lei Wang, Oleg V. Yazyev, and QuanSheng Wu. An artificial neural network approach to the analytic continuation problem, 2018.

[15] Sebastian Fuchs, Thomas Pruschke, and Mark Jarrell. Analytic continuation of quantum monte carlo data by stochastic analytical inference. *Phys. Rev. E*, 81:056701, May 2010.

[16] Niklas M. Gergs, Lars Fritz, and Dirk Schuricht. Topological order in the kitaev/majorana chain in the presence of disorder and interactions. *Phys. Rev. B*, 93:075129, Feb 2016.

[17] Olga Goulko, Andrey S. Mishchenko, Lode Pollet, Nikolay Prokof'ev, and Boris Svistunov. Numerical analytic continuation: Answers to well-posed questions. *Phys. Rev. B*, 95:014102, Jan 2017.

[18] O. Gunnarsson, M. W. Haverkort, and G. Sangiovanni. Analytical continuation of imaginary axis data for optical conductivity. *Phys. Rev. B*, 82:165125, Oct 2010.

[19] Xing-Jie Han, Hai-Jun Liao, Hai-Dong Xie, Rui-Zhen Huang, Zi-Yang Meng, and Tao Xiang. Analytic continuation with padé decomposition. *Chinese Physics Letters*, 34(7):077102, 2017.

[20] Yizhen Huang, Alejandro M. Lobos, and Zi Cai. Dissipative majorana quantum wires, 2018.

[21] Mark Jarrell and J.E. Gubernatis. Bayesian inference and the analytic continuation of imaginary-time quantum monte carlo data. *Physics Reports*, 269(3):133 – 195, 1996.

[22] Xun Jia and Sudip Chakravarty. Quantum dynamics of an ising spin chain in a random transverse field. *Phys. Rev. B*, 74:172414, Nov 2006.

[23] Jiasen Jin, Alberto Biella, Oscar Viyuela, Cristiano Ciuti, Rosario Fazio, and Davide Rossini. Phase diagram of the dissipative quantum ising model on a square lattice. *Phys. Rev. B*, 98:241108, Dec 2018.

[24] A Yu Kitaev. Unpaired majorana fermions in quantum wires. *Physics-Uspekhi*, 44(10S):131, 2001.

[25] A. J. Leggett, S. Chakravarty, A. T. Dorsey, Matthew P. A. Fisher, Anupam Garg, and W. Zwerger. Dynamics of the dissipative two-state system. *Rev. Mod. Phys.*, 59:1–85, Jan 1987.

[26] Ryan Levy, J.P.F. LeBlanc, and Emanuel Gull. Implementation of the maximum entropy method for analytic continuation. *Computer Physics Communications*, 215:149 – 155, 2017.

[27] Biao Lian, Jing Wang, Xiao-Qi Sun, Abolhassan Vaezi, and Shou-Cheng Zhang. Quantum phase transition of chiral majorana fermions in the presence of disorder. *Phys. Rev. B*, 97:125408, Mar 2018.

[28] Alejandro M. Lobos, Roman M. Lutchyn, and S. Das Sarma. Interplay of disorder and interaction in majorana quantum wires. *Phys. Rev. Lett.*, 109:146403, Oct 2012.

[29] E. Luijten. Monte carlo simulation of spin models with long-range interactions. In David P. Landau, Steven P. Lewis, and Heinz-Bernd Schüttler, editors, *Computer Simulation Studies in Condensed-Matter Physics XII*, pages 86–99, Berlin, Heidelberg, 2000. Springer Berlin Heidelberg.

[30] Erik Luijten and Holger Meßingfeld. Criticality in one dimension with inverse square-law potentials. *Phys. Rev. Lett.*, 86:5305–5308, Jun 2001.

[31] D. Maile, S. Andergassen, W. Belzig, and G. Rastelli. Quantum phase transition with dissipative frustration. *Phys. Rev. B*, 97:155427, Apr 2018.

[32] Yuezhen Niu, Suk Bum Chung, Chen-Hsuan Hsu, Ipsita Mandal, S. Raghu, and Sudip Chakravarty. Majorana zero modes in a quantum ising chain with longer-ranged interactions. *Phys. Rev. B*, 85:035110, Jan 2012.

[33] A. Östlin, L. Chioncel, and L. Vitos. One-particle spectral function and analytic continuation for many-body implementation in the exact muffin-tin orbitals method. *Phys. Rev. B*, 86:235107, Dec 2012.

[34] Junya Otsuki, Masayuki Ohzeki, Hiroshi Shinaoka, and Kazuyoshi Yoshimi. Sparse modeling approach to analytical continuation of imaginary-time quantum monte carlo data. *Phys. Rev. E*, 95:061302, Jun 2017.

[35] Vincent R. Overbeck, Mohammad F. Maghrebi, Alexey V. Gorshkov, and Hendrik Weimer. Multicritical behavior in dissipative ising models. *Phys. Rev. A*, 95:042133, Apr 2017.

[36] Bob Pego and Jian Wang. diagonalizing $\begin{pmatrix} 0 & M^T \\ M & 0 \end{pmatrix}$ numerically . https://math.stackexchange.com/questions/2412535/diagonalizing-beginpmatrix-0-mt-m-0-endpmatrix-numerically, 2017.

[37] Pierre Pfeuty. The one-dimensional ising model with a transverse field. *Annals of Physics*, 57(1):79–90, mar 1970.

[38] Marek M. Rams, Masoud Mohseni, and Adolfo del Campo. Inhomogeneous quasi-adiabatic driving of quantum critical dynamics in weakly disordered spin chains. 2016.

[39] H. M. Rønnow, R. Parthasarathy, J. Jensen, G. Aeppli, T. F. Rosenbaum, and D. F. Mc-Morrow. Quantum phase transition of a magnet in a spin bath. *Science*, 308(5720):389–392, 2005.

[40] Subir Sachdev. *Quantum phase transitions*. Wiley Online Library.

[41] Anders W. Sandvik. Stochastic method for analytic continuation of quantum monte carlo data. *Phys. Rev. B*, 57:10287–10290, May 1998.

[42] Anders W. Sandvik. Constrained sampling method for analytic continuation. *Phys. Rev. E*, 94:063308, Dec 2016.

[43] J. Schött, E. G. C. P. van Loon, I. L. M. Locht, M. I. Katsnelson, and I. Di Marco. Comparison between methods of analytical continuation for bosonic functions. *Phys. Rev. B*, 94:245140, Dec 2016.

[44] Johan Schött, Inka L. M. Locht, Elin Lundin, Oscar Grånäs, Olle Eriksson, and Igor Di Marco. Analytic continuation by averaging padé approximants. *Phys. Rev. B*, 93:075104, Feb 2016.

[45] R. N. Silver, D. S. Sivia, and J. E. Gubernatis. Maximum-entropy method for analytic continuation of quantum monte carlo data. *Phys. Rev. B*, 41:2380–2389, Feb 1990.

[46] Iver Bakken Sperstad, Einar B. Stiansen, and Asle Sudbø. Monte carlo simulations of dissipative quantum ising models. *Phys. Rev. B*, 81:104302, Mar 2010.

[47] Robert H. Swendsen and Jian-Sheng Wang. Nonuniversal critical dynamics in monte carlo simulations. *Phys. Rev. Lett.*, 58:86–88, Jan 1987.

[48] Olav F. Syljuåsen. Using the average spectrum method to extract dynamics from quantum monte carlo simulations. *Phys. Rev. B*, 78:174429, Nov 2008.

[49] Denis Tolkunov and Vladimir Privman. Short-time decoherence for general system-environment interactions. *Phys. Rev. A*, 69:062309, Jun 2004.

[50] H. J. Vidberg and J. W. Serene. Solving the eliashberg equations by means ofn-point padé approximants. *Journal of Low Temperature Physics*, 29(3):179–192, Nov 1977.

[51] Klaus Völker. Dynamical behavior of the dissipative two-state system. *Phys. Rev. B*, 58:1862–1871, Jul 1998.

[52] Jian Wang and Sudip Chakravarty. Binary disorder in quantum ising chains and induced majorana zero modes, 2018.

[53] Jian Wang and Sudip Chakravarty. Rational function regression method for numerical analytic continuation. 2018.

[54] H. Weisbrich, C. Saussol, W. Belzig, and G. Rastelli. Decoherence in the quantum ising model with transverse dissipative interaction in the strong-coupling regime. *Phys. Rev. A*, 98:052109, Nov 2018.

[55] Ulrich Weiss. *Quantum Dissipative Systems*. WORLD SCIENTIFIC, 4th edition, 2012.

[56] Philipp Werner, Matthias Troyer, and Subir Sachdev. Quantum spin chains with site dissipation. *Journal of the Physical Society of Japan*, 74(Suppl):67–70, 2005.

[57] Philipp Werner, Klaus Völker, Matthias Troyer, and Sudip Chakravarty. Phase diagram and critical exponents of a dissipative ising spin chain in a transverse magnetic field. *Phys. Rev. Lett.*, 94:047201, Jan 2005.

[58] M. Wimmer. Efficient numerical computation of the pfaffian for dense and banded skew-symmetric matrices. 2011.

[59] Ulli Wolff. Collective monte carlo updating for spin systems. *Phys. Rev. Lett.*, 62:361–364, Jan 1989.

[60] Zheng Yan, Lode Pollet, Jie Lou, Xiaoqun Wang, Yan Chen, and Zi Cai. Interacting lattice systems with quantum dissipation: A quantum monte carlo study. *Phys. Rev. B*, 97:035148, Jan 2018.

[61] Hongkee Yoon, Jae-Hoon Sim, and Myung Joon Han. Analytic continuation via 'domain-knowledge free' machine learning, 2018.

[62] A. P. Young and H. Rieger. Numerical study of the random transverse-field ising spin chain. *Phys. Rev. B*, 53:8486–8498, Apr 1996.